# nature cell biology



**Article** 

https://doi.org/10.1038/s41556-025-01773-z

# Microtubule architecture connects AMOT stability to YAP/TAZ mechanotransduction and Hippo signalling

Received: 5 February 2025

Accepted: 22 August 2025

Published online: 1 October 2025



Giada Vanni¹, Anna Citron¹, Ambela Suli¹, Paolo Contessotto¹, Robin Caire¹, Alessandro Gandin², Giovanna Mantovan¹, Francesca Zanconato¹, Giovanna Brusatin ®², Michele Di Palma³, Elisa Peirano³, Lisa Sofia Pozzer³, Carlo Albanese Jr¹, Roberto A. Steiner³,⁴, Michelangelo Cordenonsi ®¹, Tito Panciera ®¹,⁶ ⋈ & Stefano Piccolo ®¹,⁵,⁶ ⋈

Cellular mechanotransduction is a key informational system, yet its mechanisms remain elusive. Here we unveil the role of microtubules in mechanosignalling, operating downstream of subnuclear F-actin and nuclear envelope mechanics. Upon mechanical activation, microtubules reorganize from a perinuclear cage into a radial array nucleated by centrosomes. This structural rearrangement triggers degradation of AMOT proteins, which we identify as key mechanical rheostats that sequester YAP/TAZ in the cytoplasm. AMOT is stable in mechano-OFF but degraded in mechano-ON cell states, where microtubules allow AMOT rapid transport to the pericentrosomal proteasome in complex with dynein/dynactin. This process ensures swift control of YAP/TAZ function in response to changes in cell mechanics, with experimental loss of AMOT proteins rendering cells insensitive to mechanical modulations. Ras/RTK oncogenes promote YAP/TAZ-dependent tumorigenesis by corrupting this AMOT-centred mechanical checkpoint. Notably, the Hippo pathway fine-tunes mechanotransduction: LATS kinases phosphorylate AMOT, shielding it from degradation, thereby indirectly restraining YAP/TAZ. Thus, AMOT protein stability serves as a hub linking cytoskeletal reorganization and Hippo signalling to YAP/TAZ mechanosignalling.

Mechanical forces are increasingly recognized as pervasive factors in cell physiology, controlling multiple aspects of cell behaviour, including differentiation, proliferation and tumorigenesis<sup>1-4</sup>. The ability to sense mechanical forces must rely on the cell's construction principles; physical and architectural properties of the microenvironment, initially perceived at adhesive sites, need to be transmitted to the cytoskeleton and then other, still poorly understood, intracellular transducers. The discovery of the yes-associated-protein (YAP)/transcriptional

coactivator with a PDZ-binding motif (TAZ) transcriptional regulators as pervasive transducers of physical signals into gene-expression programs opened the possibility to dissect and functionally probe cellular mechanosignalling mechanistically<sup>5,6</sup>. Yet, in spite of extensive efforts, it remains largely enigmatic how mechanically induced changes in a cell's cytoskeleton may ultimately impact a dominant event of mechanotransduction: the displacement of YAP/TAZ from so far poorly understood cytoplasmic anchors, allowing YAP/TAZ entry into the nucleus<sup>4,7</sup>.

<sup>1</sup>Department of Molecular Medicine, University of Padova, Padova, Italy. <sup>2</sup>Department of Industrial Engineering, University of Padova, Padova, Italy. <sup>3</sup>Department of Biomedical Sciences, University of Padova, Padova, Italy. <sup>4</sup>Randall Centre for Cell and Molecular Biophysics, King's College London, London, UK. <sup>5</sup>IFOM ETS, the FIRC Institute of Molecular Oncology, Milan, Italy. <sup>6</sup>These authors jointly supervised this work: Tito Panciera, Stefano Piccolo. —e-mail: tito.panciera@unipd.it; stefano.piccolo@unipd.it In this view, a mechanical continuum of interconnected subcellular systems must be in place to allow the cell to entirely restructure itself in response to mechanical cues. Major emphasis in cell mechanics has so far been placed on F-actin microfilaments, whose structural organization and tensional state are directly connected to cellular adhesive systems<sup>8,9</sup>. Dissolution of F-actin filaments by drug treatments is known to prevent YAP/TAZ nuclear accumulation. Conversely, boosting microfilament formation, as in cells lacking F-actin severing proteins, potently drives YAP/TAZ activation<sup>5,10</sup>. Yet, the direct link between YAP/TAZ control and F-actin still largely relies on inference. No biochemical mechanism involving bona fide F-actin-regulated protein has been directly connected to YAP/TAZ control<sup>6</sup>.

With this background in mind, we began this investigation by considering the contribution of cytoskeletal systems other than F-actin in connecting cell-shape changes to mechanotransduction. Besides their well-established function in cell division, microtubules (MTs) are fundamental regulators of cell shape and motility, on par with actin-based processes<sup>11–14</sup>. MT-associated proteins have recently been reported to tune focal adhesions at the cell periphery<sup>11</sup>. Yet, how MTs switch their own architecture in response to distinct physical cues and their direct involvement in mechanosignalling is only rudimentarily understood. This represents a potentially large black box, as MTs are a self-organizing, pervasive and highly dynamic system, whose spatial organization (for example, presence or absence of the centrosome or its location) is known to be intertwined with distinct cell states and functions<sup>15</sup>. Just like F-actin, MTs connect to the nucleus, whose role in mechanotransduction has recently emerged<sup>16,17</sup>. Crucially, the architecture of MTs spatially organizes several subcellular structures by coordinating protein and organelle trafficking, in turn preserving cellular structure and function15. By focusing on MTs, here we shed new light on the mechanisms of mechanosignalling, and, in so doing, we advance on the view that the response to mechanical cues is coordinated at the whole cell level, involving a hierarchical coordination between distinct subcellular structures.

Fig. 1 | Microtubule organization serves as a determinant of YAP/TAZ mechanotransduction. a, Left: representative IF images (3D sections) of MCF10A cells seeded on stiff (40 kPa, mechano-ON, hereafter Mech.ON) versus soft (0.7 kPa, mechano-OFF, hereafter Mech.OFF) hydrogels. Right: quantifications of  $\gamma$ -TURC number in cells seeded as in the left panels for n=65(Mech.ON) and n = 51 (Mech.OFF) pooled from two independent seedings. P < 0.0001. b, Left: representative IF images (3D sections) of MCF10A cells seeded on spread (unconfined, Mech.ON) versus small (100 µm2 micropatterns, Mech.OFF) substrates. Right: quantifications (n = 50 cells for each condition, pooled from two independent seedings) of y-TURC number in cells seeded as in the left panels. P < 0.0001. In **a** and **b**, MT are labelled by  $\alpha$ -tubulin staining (αTub, magenta), γ-TURCs by γ-tubulin staining (γTub, yellow) and nuclei are counterstained with Hoechst (cyan). White arrowheads in Mech.ON panels indicate γ-TURCs convergence into a single MTOC. Scale bars (a,b), 5 μm. Extended Data Fig. 1a and Supplementary Video 1 provide 3D reconstructions of cells seeded as in a and b. Comparable results were obtained with HEK293 and U2OS cells (Extended Data Fig. 1c,d). c, Representative IF images (3D sections) of MCF10A cells seeded on stiff (40 kPa, Mech.ON) versus soft (0.7 kPa, Mech.OFF) hydrogels, MT architecture is labelled by  $\alpha$ -tubulin staining ( $\alpha$ Tub, magenta) and the centrosome by pericentrin staining (PCNT1, grey) and highlighted by a white arrowhead. Nuclei are counterstained with Hoechst (cyan). Scale bars, 5 μm. Extended Data Fig. 1b presents representative IF images (3D sections) of MCF10A cells seeded on spread versus small substrates and stained as in c. Comparable results were obtained with HEK293 and U2OS cells (Extended Data Fig. 1c,d). d, Left: representative IF images of MTs and y-TURCs (top panels) and EGFP-YAP (bottom panels) in MCF10A cells bearing a YAP-EGFP knock-in(KI) allele seeded on hydrogels tuned to the indicated stiffness gradient. Images in the top panels are magnifications of the insets shown in the upper right corners. Scale bars, 5  $\mu$ m. Right: quantifications of  $\gamma$ -TURCs (left, n = 49 cells for 40 kPa, n = 52for 13 kPa, n = 53 each for all other conditions, pooled from two independent seedings) and YAP nuclear-to-cytoplasmic subcellular localization (N/C, right, n = 63 cells for 40 kPa, n = 51 for 3 kPa, n = 53 for each for all other conditions,

#### Results

# Microtubule centrosomal organization as dominant determinant of mechanosignalling

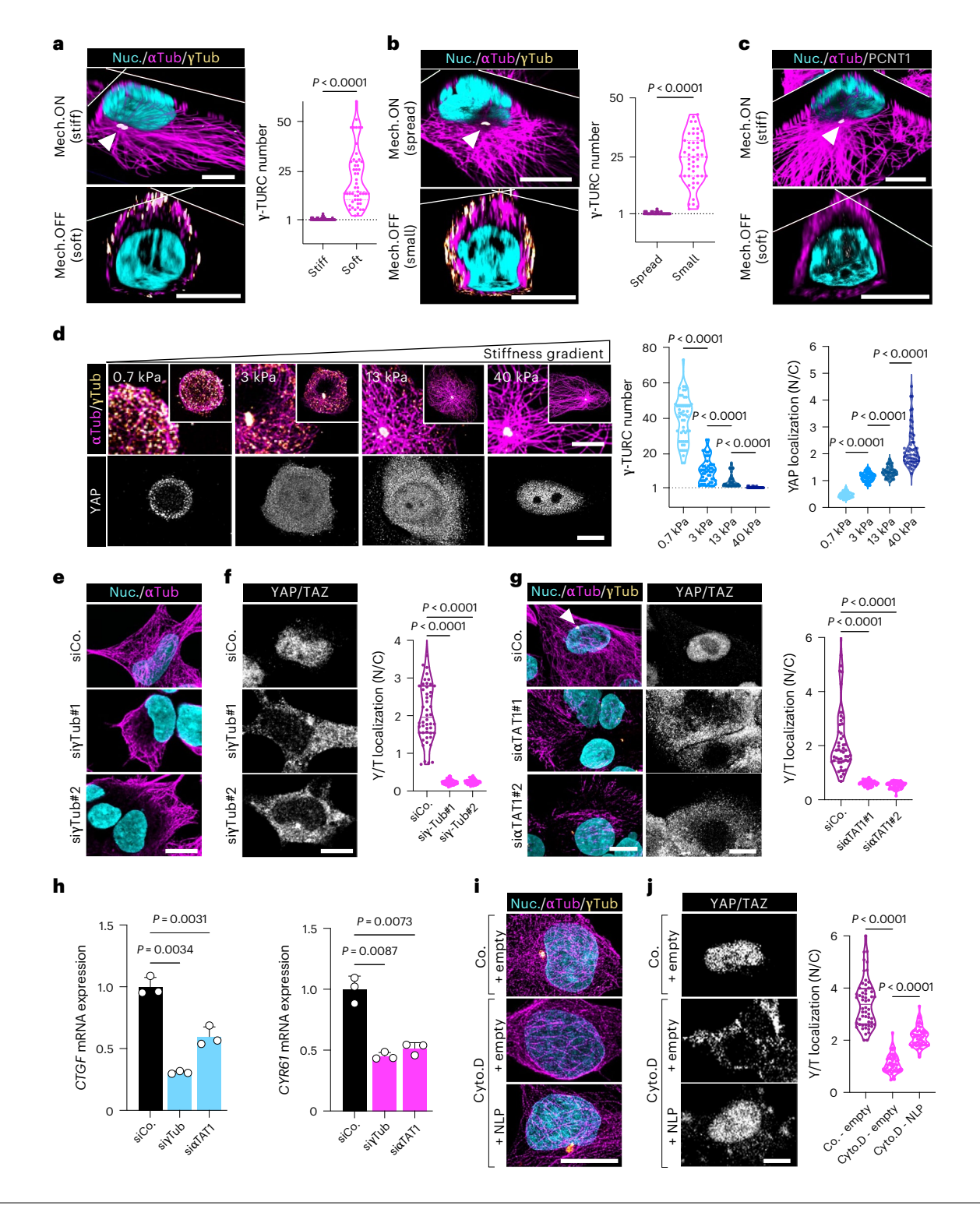
We adopted MT-compatible immunofluorescence (IF) procedures and MT-specific live imaging probes to investigate the structural organization of the MT lattice in cells either seeded on soft 0.7-kPa extracellular matrix (ECM) or confined to small adhesive areas (hereafter mechano-OFF cells), and compared them to cells either stretched on a rigid 40-kPa ECM or unconfined substrates (mechano-ON cells). Mechano-ON cells displayed a prominent perinuclear centrosome labelled by y-tubulin and pericentrin, established markers of the microtubule organizing centre (MTOC; Fig. 1a-c, Extended Data Fig. 1a,b and Supplementary Video 1). As expected<sup>15</sup>. MTs sprout in an astral arrangement from the MTOC, radiating towards the cell periphery, displaying a planar polarized alignment along the cell elongation axis (Fig. 1a-c, Extended Data Fig. 1a,b and Supplementary Video 1). Strikingly, however, MT organization dramatically changes in response to mechano-inhibitory inputs. Mechano-OFF cells lose the MTOC, and their MTs become acentrosomal and display an inverted polarity, with minus-ends anchored to multiple peripheral y-TURCs, mainly located beneath the apical cell cortex. All in all, this generates a MT network with an apico-basal 'cage-like' structure around the nucleus (Fig. 1a-c, Extended Data Fig. 1a,b and Supplementary Video 1). These findings were obtained independently in different cell types, such as MCF10A, HEK293 and U2OS cells (Extended Data Fig. 1c,d). Collectively, these results show that comparable MT restructuring occurred in distinct experimental mechano-ON versus mechano-OFF conditions, that is, in cells plated on stiff versus soft substrates, on large versus small adhesive islands, in sparse versus high density, or in cells experiencing mechanically dynamic hydrogels<sup>18</sup>. Changes in MT spatial organization are intrinsic to the cellular response to mechanical cues, with mechano-ON, but not mechano-OFF cells, displaying a perinuclear MTOC and centrosome.

pooled from two independent seedings) in cells seeded as in the left panels. P < 0.0001. **e**, Representative IF images of MTs ( $\alpha$ Tub) in HEK293 cells transfected with the indicated siRNAs. Nuclei are counterstained with Hoechst (cyan). Scale bar, 10 µm. f, Left: representative IF images of YAP/TAZ (Y/T, grey) in HEK293 cells transfected with the indicated siRNAs. Right: quantifications (n = 51 cells for siyTub#1, n = 50 cells each for all other conditions, pooled from two independent seedings) of YAP/TAZ N/C subcellular localization in cells treated as in the left panels. P < 0.0001. g, Left: representative IF images of MTs (αTub), γ-TURCs (yTub) and YAP/TAZ in HEK293 cells transfected with the indicated siRNAs. Nuclei are counterstained with Hoechst (cvan). The white arrowhead indicates MT convergence in the centrosomal MTOC in control cells. Scale bars (f,g), 10  $\mu$ m. Right: quantifications (n = 50 cells for siCo., n = 52 cells each for all other conditions, pooled from two independent seedings) of YAP/TAZ N/C subcellular localization in cells treated as in the left panels. P < 0.0001. h, Quantitative realtime PCR (qRT-PCR) assessing the expression levels of the YAP/TAZ endogenous targets CTGF (left) and Cyr61 (right) in MCF10A cells treated with the indicated siRNAs and seeded in Mech.ON conditions. Data are presented as mean + s.d. of n = 3 biologically independent samples. In the left graph, P = 0.0034 (siCo. versus  $si\gamma Tub$ ), P = 0.0031 (siCo. versus  $si\alpha TAT1$ ); right graph P = 0.0087 (siCo. versus siyTub), P = 0.0073 (siCo. versus  $si\alpha TAT1$ ). Extended Data Fig. 2d presents similar results obtained with U2OS cells. i, Representative IF images of MTs (αTub) and y-TURCs (yTub) in HEK293 cells transduced with empty or NLP1-encoding lentiviruses and treated with cytochalasin D (Cyto.D, 1  $\mu$ M for 2 h) or DMSO as negative control (Co.). Nuclei are counterstained with Hoechst (cyan). Scale bar, 5 μm. j, Left: representative IF images of YAP/TAZ (grey) in HEK293 cells treated as in i. Right: quantifications (n = 52 cells for each condition, pooled from two independent seedings) of YAP/TAZ N/C subcellular localization in cells treated as in the left panels. P < 0.0001. Extended Data Fig. 2f shows controls demonstrating effective F-actin disruption by Cyto.D treatment. P values were determined by unpaired two-tailed Student's t-test with Welch's correction (a,b) or one-way analysis of variance (ANOVA) with Welch's correction (d,f-h,j).

We next asked to what extent MT centrosomal organization correlates with mechanotransduction, as quantified by YAP/TAZ nuclear entry, an established proxy of YAP/TAZ activation <sup>19</sup>. For this, we exposed cells to a gradient of mechanical forces by seeding them on substrates ranging from 0.7-kPa to 40-kPa elastic modules; in these cultures, we then quantified, by IF, the YAP/TAZ nucleo/cytoplasmic ratio and the number of  $\gamma$ -TURCs per individual cell by anti- $\gamma$ -Tub staining (Fig. 1d). Cells with the highest level of nuclear YAP/TAZ were those displaying a single  $\gamma$ -TURC signal (set to 1 in Fig. 1d), corresponding to a single perinuclear MTOC. Conversely, cells seeded at the lowest stiffness displayed cytoplasmic YAP/TAZ accompanied by multiple independently scattered  $\gamma$ -TURCs that never converge into an individual MTOC

(Fig. 1d). Intriguingly, at intermediate mechanical states (3–13 kPa in Fig. 1d), one MTOC typically coexists in the same cell with peripherally scattered  $\gamma$ -TURC signals, whose number correlated with YAP/TAZ cytoplasmic retention (proxy of YAP/TAZ turn OFF). These findings indicate that the perinuclear MTOC and its associated MT aster are mechanically regulated cellular structures connecting cellular architectural features with YAP/TAZ mechanotransduction.

Given the above correlations, we next asked to what extent centrosomal MT organization is causal for YAP/TAZ regulation. For this, we first inhibited MTOC formation in mechano-ON cells by depletion of  $\gamma$ -tubulin. Notably, as shown in Fig. 1e, this treatment causes the disappearance of radial MTs from the perinuclear area, yet preserves shorter



MTs at the cell periphery. Importantly, this invariably results in YAP/TAZ cytoplasmic retention (Fig. 1f), with ensuing inhibition of YAP/TAZ transcriptional activity, as measured by endogenous target gene expression (Extended Data Fig. 1e), suggesting the key role of pericentrosomal MT organization for YAP/TAZ activation. Of note, cells depleted of  $\gamma$ -tubulin display overtly normal focal adhesions, as assessed by paxillin staining, and F-actin arrangement (Extended Data Fig. 1f), a finding compatible with the view that MTs are essential regulators of YAP/TAZ function acting either downstream or in parallel to actomyosin.

To further validate that MT centrosomal organization serves as a determinant of mechanosignalling, we next tackled MT acetylation, a central post-translational modification essential for MTs to bend without breaking, and thus critical for the stability of the curved aster of perinuclear MTs<sup>20</sup>. Indeed, in mechano-ON cells, perinuclear astral MTs are more acetylated than peripheral ones (Extended Data Fig. 2a). The main enzyme responsible for MT acetylation is the tubulin acetyl-transferase ( $\alpha$ -TAT1)<sup>20</sup>, and its depletion with independent small interfering RNAs (siRNAs) caused loss of pericentrosomal MTs and YAP/TAZ inhibition (Fig. 1g, h and Extended Data Fig. 2b–d). Of note, this occurred while preserving short MTs at the cell periphery and without interfering with F-actin architecture, focal adhesion engagement and cell spreading (Fig. 1g and Extended Data Fig. 2e), all in all phenocopying  $\gamma$ -tubulin depletion.

Given the above requirement of the MTOC and radial MT sprouting for YAP/TAZ activation in mechano-ON cells, we then asked whether experimentally sustaining such structural features in mechano-OFF cells is sufficient to rescue nuclear YAP/TAZ accumulation. For this, we considered ninein-like protein 1 (NLP1), a centrosomal factor instrumental for centrosome maturation and MT nucleation<sup>21</sup>. We opted to overexpress NLP1 in cells experiencing an extreme mechano-OFF condition, that is, in cells void of F-actin after cytochalasin D (Cyto.D) treatment. Remarkably, even in this condition, gain of NLP1 was sufficient to rescue perinuclear MTOC formation, radial MTs and YAP/TAZ nuclear accumulation (Fig. 1i,j and Extended Data Fig. 2f). As forcing centrosome formation is sufficient to sustain mechanosignalling in mechano-OFF conditions, this implies that the centrosome acts formally downstream of F-actin in mechanosignalling.

# A mechanical continuum between a stress fibre subpool, the nuclear envelope and microtubules

The above results leave unaddressed how mechanical forces, well known to be primarily perceived by F-actin at sites of cell-ECM adhesions<sup>8,9</sup>, could ultimately converge on perinuclear MT organization and YAP/TAZ regulation. The nuclear envelope (NE) has recently emerged as a central hub integrating tensional forces generated by the actomyosin cytoskeleton in a mechanical continuum with the other cytoskeletal systems16. Central to this network are LINC complexes, which connect nuclear lamins with F-actin (through nesprin1/2) and SUN) and MTs (through nesprin4)<sup>16,17,22</sup>. We found by dual IF for F-actin and laminA that two distinct subpools of stress fibres exist in epithelial cells: stress fibres that do not contact the NE, and ventral stress fibres that do (hereafter nuclear-associated stress fibres, NASFs; Fig. 2a and Extended Data Fig. 3a). This distinction was derived by applying a machine-learning classifier to differentially segment phalloidin-stained F-actin fibres whose pixels colocalize with the laminA-stained NE in three-dimensional (3D) confocal reconstructions. Importantly, NASFs tether the cell surface with the basal side of the NE exclusively in mechano-ON cells (Supplementary Video 2). Using a conformation-sensitive anti-laminA antibody<sup>23</sup>, we also found that the NASFs-NE interaction stretches the basal side of the NE (Extended Data Fig. 3b). Interrupting this mechanical continuum by SUN2 depletion indeed not only abolishes NASFs formation and induces NE relaxation (Fig. 2b and Extended Data Fig. 3c,d), but also causes YAP/TAZ cytoplasmic retention, with ensuing downregulation of YAP/TAZ target genes (Fig. 2c,d and Extended Data Fig. 3e-g).

Of note, this occurs without overtly interfering with cell shape or the other stress fibre subtypes that characterize the mechano-ON state (Extended Data Fig. 3d,h).

MTs are known to push against the nucleus, inducing the typical indentation described to host the centrosome in many cultured mammalian cells ('centrosomal bay')<sup>24,25</sup>. Is NE anchorage by NASFs required for such MT-generated forces? We found that SUN2 depletion impeded close MT attachment to the NE, in turn causing defective MTOC formation and localization, together resulting in severely inhibited MT convergence to the perinuclear centrosome (Fig. 2e). We then asked whether the physical connection between MTs and the NE is key to allow centrosome formation and MT radial organization. For this, we interfered with nesprin4 or emerin, the main MT-anchoring factors at the NE<sup>16,17,22</sup>. Similarly to SUN2 depletion, loss of emerin or nesprin4 results in defective MTOC, loss of centrosomal MTs and YAP/TAZ inhibition (Fig. 2f–k and Extended Data Fig. 4a–f).

To reinforce the notion that MT centrosomal organization acts downstream of F-actin-mediated force sensing, we monitored YAP/TAZ activity in cells lacking the F-actin capping/severing factors actin depolymerizing factor (ADF)/cofilin. As previously reported, depletion of ADF/cofilin potently rescued YAP/TAZ activity in mechano-OFF conditions  $^{10}$ . However, we found that this rescue is impaired by concomitant depletion of  $\alpha$ -TAT1 or nesprin4 (Extended Data Fig. 4g), indicating that boosting F-actin stress fibres requires pericentrosomal MTs to impact on mechanosignalling.

#### AMOT protein stabilization as mechano-rheostat

How does the centrosomal MTOC trigger YAP/TAZ mechanotransduction? In addressing this crucial question, we considered the well-known role of the multiprotein centrosomal assembly in coordinating local degradation of proteasomal substrates. Indeed, earlier work has shown that other signalling factors, such as polyubiquitinated Smad1, β-catenin and Axin2, display continuous delivery to the centrosomal proteasome<sup>26-28</sup>. Also well-established is the role of MTs originating from the MTOC in allowing dynein-mediated retrograde flow of cellular components towards the proteasome at pericentrosomal condensates<sup>15</sup>. As previously reported<sup>27,29</sup>, the cellular proteasome is enriched at the centrosomal bay (Fig. 3a). We found that proteasomal accumulation at the centrosome itself is dependent on the mechanical state of the cell and correlates with MT architecture, with mechano-ON cells displaying proteasome enrichment at the perinuclear centrosome and mechano-OFF cells displaying more diffused proteasomes throughout the cytoplasm (Fig. 3a and Extended Data Fig. 5a). Intriguingly, we also found that proteasome localization is dependent on the NASFs-NE-MTs mechanical equilibrium, as interfering with SUN2 or emerin results in failed proteasome aggregation at the centrosomal bay (Fig. 3b and Extended Data Fig. 5b).

We surmised that a scenario that could mechanistically explain YAP/TAZ regulation by MTs may be one in which the mechanoregulated perinuclear MTOC and proteasome condensation are required for degradation of a YAP/TAZ cytoplasmic inhibitor. Although the existence of a mechanoregulated YAP/TAZ inhibitor has long been postulated, its identification has remained elusive<sup>30</sup>. In pursuing this hypothesis, we unbiasedly searched the BioGRID4.4 dataset<sup>3</sup> to compile a list of cytoplasmic proteins interacting with both YAP and TAZ (Supplementary Table 1). We tested whether mechanical cues could tune their endogenous levels. By carrying out western blots of mechano-ON versus -OFF cell lysates, we found that the stability of only one such protein, AMOT-p130, stood out for being strikingly mechanoregulated (Fig. 3c and Extended Data Fig. 5c,d) in the absence of any effect at the level of AMOT mRNA transcription (Extended Data Fig. 5e). This was an intriguing finding, as AMOT has been shown to interact directly with YAP/TAZ<sup>32</sup>, acting as a scaffold protein for their large tumor suppressor kinase (LATS)-mediated phosphorylation and thus contributing to YAP/TAZ inhibition by

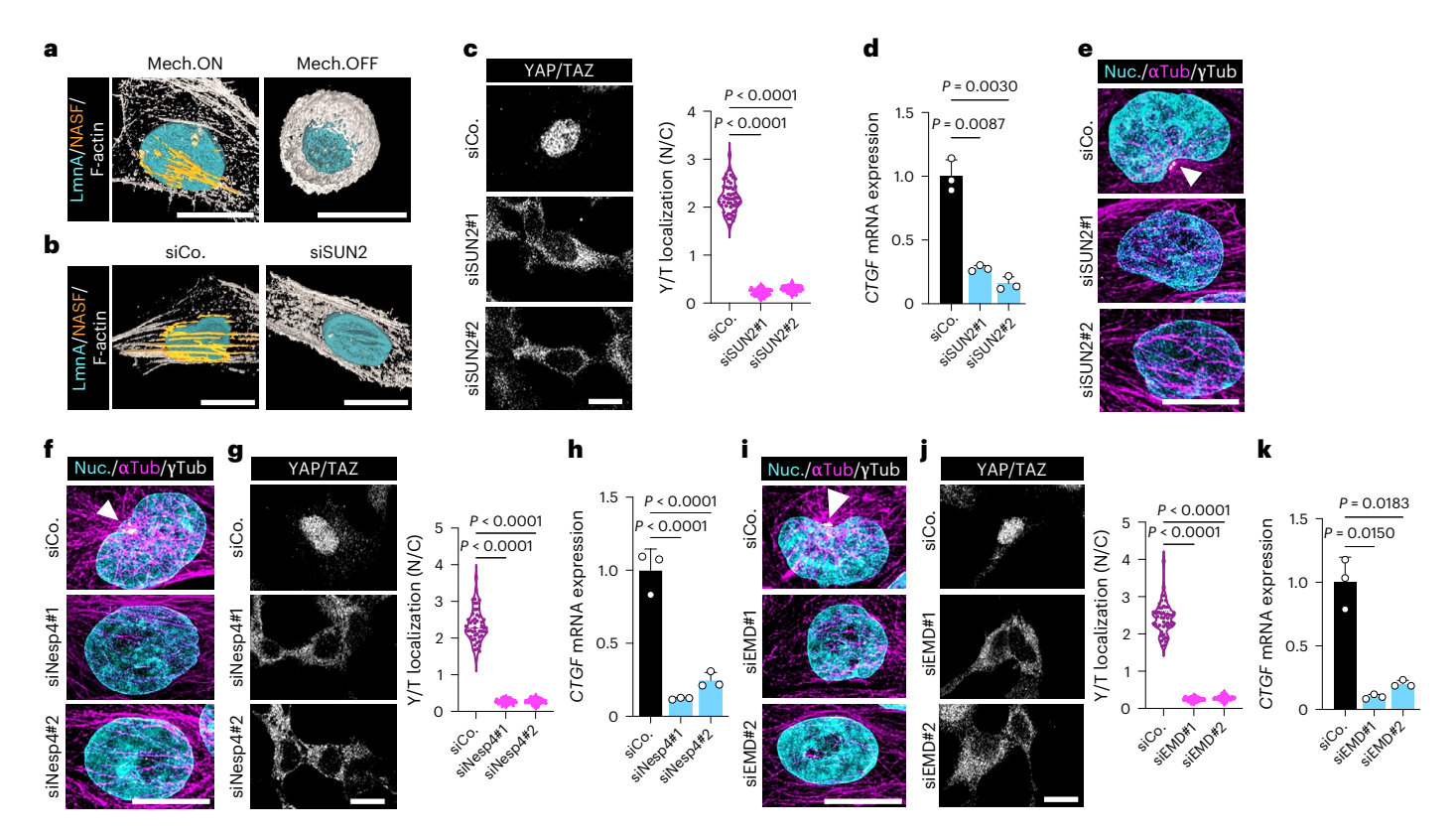


Fig. 2 | A mechanical continuum between stress fibres, the NE and MTs dictates YAP/TAZ mechanotransuction. a, Representative 3D IF reconstructions of MCF10A cells seeded in Mech.ON (40 kPa) versus Mech.OFF (0.7 kPa) conditions. Scale bars, 10 µm. Supplementary Video 2 presents a wrap-around view and Extended Data Fig. 3a representative Z-planes of cells seeded as in a. The nuclear lamina was labelled by laminA staining (LmnA, cyan) and F-actin by phalloidin staining (F-actin, grey). NASFs are highlighted in orange in the 3D reconstruction (Methods). b, Representative 3D IF reconstructions of MCF10A cells treated with the indicated siRNAs. Scale bars, 10 µm. Extended Data Fig. 3d presents representative Z-planes of cells treated with the same siRNAs. The nuclear lamina is labelled by laminA staining (LmnA, cyan) and F-actin by phalloidin staining (F-actin, grey). NASFs are highlighted in orange in the 3D reconstruction (Methods). c, Left: representative IF images of YAP/TAZ (grey) in HEK293 cells transfected with the indicated siRNAs. Scale bar, 10 µm. Right: quantifications (n = 50 cells for each condition, pooled from two independent seedings) of YAP/TAZ N/C subcellular localization in cells treated as in the left panels. P < 0.0001. d. gRT-PCR assessing the expression levels of the YAP/TAZ endogenous target CTGF in HEK293 cells treated with the indicated siRNAs and seeded in Mech.ON conditions. Data are presented as mean + s.d. of n = 3 biologically independent samples. P = 0.0087 (siCo. versus siSUN2#1), P = 0.003 (siCo. versus siSUN2#2). Extended Data Fig. 3e presents qRT-PCR results assessing the expression levels of the YAP/TAZ endogenous target Cyr61 in the same experiment. e,f, Representative IF images of MTs (αTub) and γ-TURC (γTub) in HEK293 cells transfected with the indicated siRNAs. Nuclei are counterstained with Hoechst (cyan). The white arrowhead indicates MT convergence in a perinuclear MTOC

only in control cells (siCo.). Scale bar, 10 µm. g, Left: representative IF images of YAP/TAZ (grey) in HEK293 cells transfected with the indicated siRNAs. Scale bar, 10  $\mu$ m. Right: quantifications (n = 50 cells for each condition, pooled from two independent seedings) of YAP/TAZ N/C subcellular localization in cells treated as in the left panels. P < 0.0001. **h**, qRT-PCR assessing the expression levels of the YAP/TAZ endogenous target CTGF in HEK293 cells treated with the indicated siRNAs and seeded in Mech.ON conditions. Data are presented as mean + s.d. of n = 3 biologically independent samples. P < 0.0001. See Extended Data Fig. 4a for qRT-PCR assessing the expression levels of the YAP/TAZ endogenous target Cyr61 in the same experiment. i, Representative IF images of MTs ( $\alpha$ Tub) and y-TURCs (yTub) in HEK293 cells transfected with the indicated siRNAs. The white arrowhead highlights MT convergence in a perinuclear MTOC only in control (siCo.) cells. Nuclei are counterstained with Hoechst (cyan). Scale bar, 10 µm. j, Left: representative IF images of YAP/TAZ (grey) in HEK293 cells transfected with the indicated siRNAs. Scale bar, 10  $\mu$ m. Right: quantifications (n = 50 cells for each condition, pooled from two independent seedings) of YAP/TAZ N/C subcellular localization in cells treated as in the left panels, P < 0.0001. k, qRT-PCR assessing the expression levels of the YAP/TAZ endogenous target  $\textit{CTGF} in \, \text{HEK293} \, cells \, treated \, with \, the \, indicated \, siRNAs \, and \, seeded \, in \, Mech. ON$ conditions. Data are presented as mean + s.d. of n = 3 biologically independent samples. P = 0.015 (siCo. versus siEMD#1), P = 0.0183 (siCo. versus siEMD#2). Extended Data Fig. 4c presents qRT-PCR results assessing the expression levels of the YAP/TAZ endogenous target Cyr61 in the same experiment. P values were determined by one-way ANOVA with Welch's correction (c,d,g,h,j,k).

the Hippo pathway<sup>33</sup>. Yet, the role of AMOT in mechanosignalling remains poorly addressed. In vitro, AMOT has also been proposed to associate with F-actin<sup>34</sup>, although the importance of this observation for mechanosignalling remains unclear. For example, we found that AMOT levels are equally stabilized by treatment with microfilament inhibitory drugs (Extended Data Fig. 5f-h) or by physiologically mimicking mechano-OFF cell states (Fig. 3c), in which F-actin levels, if anything, tend to increase when compared to mechano-ON cells (Extended Data Fig. 5i). Importantly, we also found that AMOT levels are similarly increased by treatment of mechano-ON cells with inhibitors of MT polymerization, such as nocodazole and vincristine

(Extended Data Fig. 5j). In other words, AMOT stabilization is orchestrated by mechanosignalling events that formally also operate independently of F-actin.

Next, we thus addressed the role of centrosomal MT organization as a determinant of AMOT stabilization. We tested this in all experimental conditions that we found above to inhibit centrosome formation. We found that AMOT stabilization occurs in mechano-ON cells after (1) uncoupling the NE from NASFs (that is, after SUN2 depletion), (2) uncoupling the NE from MTs (that is, upon nesprin4 depletion) or (3) impairing perinuclear MT aster stability through inhibition of MT acetylation (that is, after  $\alpha$ -TAT1 depletion) (Fig. 3d).

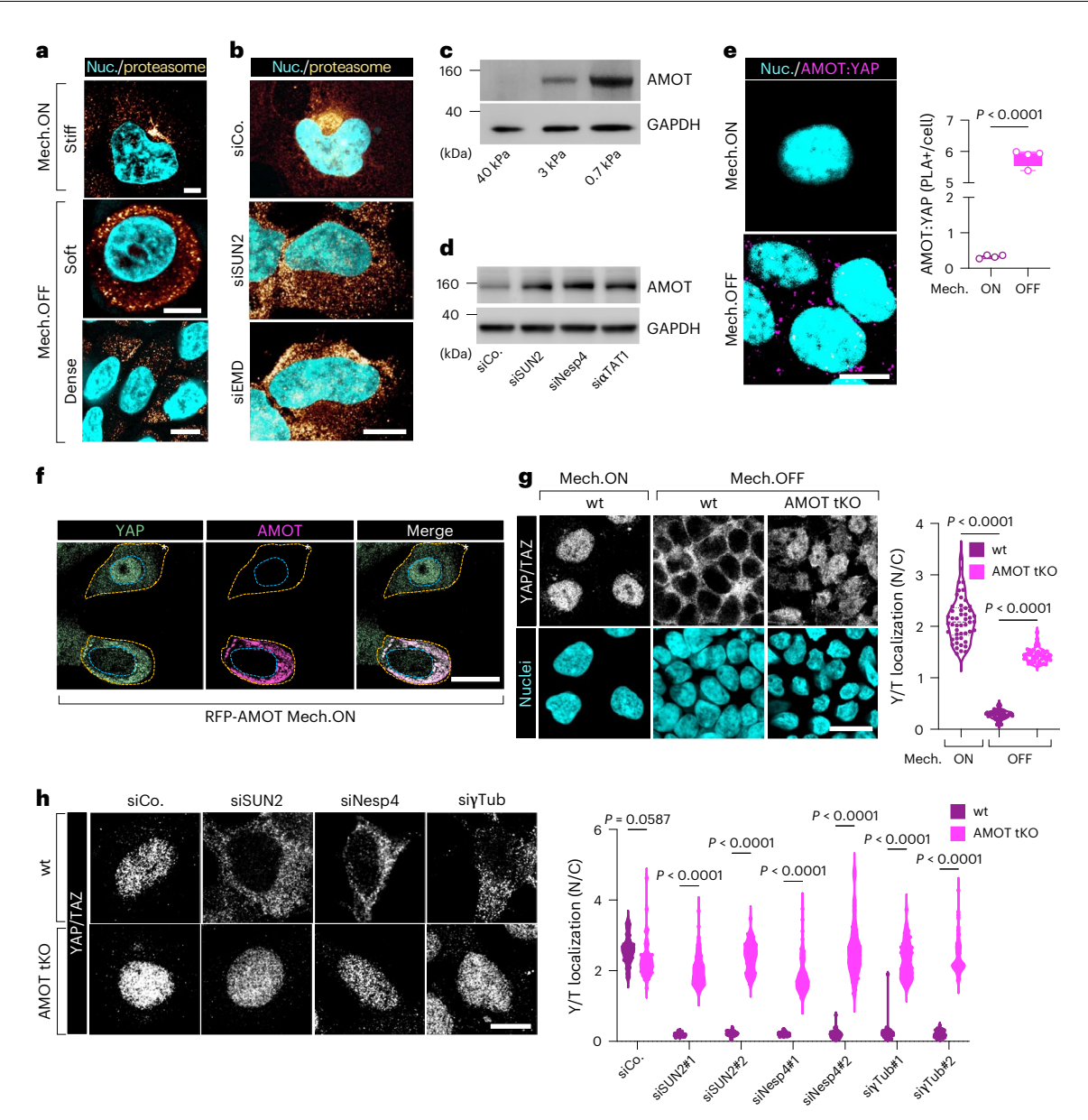


Fig. 3 | AMOT acts as a cytoplasmic mechanical rheostat to control YAP/TAZ activity. a, Representative IF images of HEK293 cells seeded in Mech.ON (stiff, 40-kPa hydrogels) versus Mech.OFF (soft, 0.7-kPa hydrogels or dense culture) conditions. The proteasome was labelled by 20S/PSMA5 staining (proteasome, yellow) and nuclei were counterstained with Hoechst (cyan). Scale bars, 10 µm. Extended Data Fig. 5a presents quantifications of proteasome localization in cells seeded under the same conditions. b, Representative IF images of HEK293 cells seeded in Mech.ON conditions and treated with the indicated siRNAs. The proteasome was labelled by 20S/PSMA5 staining (proteasome, yellow) and nuclei were counterstained with Hoechst (cyan). Scale bar, 10 µm. Extended Data Fig. 5b presents quantifications of proteasome localization in cells treated in the same way. c, Representative AMOT immunoblot of MCF10A cells seeded on hydrogels of the indicated stiffness. GAPDH serves as loading control. The same experiment was repeated twice with comparable results. Extended Data Fig. 5d,f-h presents AMOT immunoblots from cells experiencing independent Mech.OFF conditions by treatment with F-actin inhibitors, and Supplementary Fig. 1a shows quantifications. d, Representative AMOT immunoblot of HEK293 cells treated with the indicated siRNAs. GAPDH serves as loading control. Supplementary Fig. 1b provides quantifications. The same experiment was repeated twice with comparable results. e, Left: representative images of PLAs showing exclusively cytoplasmic interaction (magenta) between endogenous AMOT and YAP/TAZ in HEK293 cells seeded in Mech.OFF conditions. Mech. ON conditions (absence of endogenous AMOT protein) serve as a negative

control. Nuclei are counterstained with Hoechst (cyan). Scale bar, 10 µm. Right: quantification of the mean number of PLA dots per cell (50 cells were quantified for each n = 4 independent experiment). The boxplot shows the interquartile range, and whiskers represent min to max. P < 0.0001. **f**, Representative stills from live fluorescence images of RFP-AMOT-expressing MCF10A-YAP-EGFP<sup>KI</sup> cells showing that AMOT overexpression is sufficient to cause YAP cytoplasmic retention in Mech.ON conditions. Cells without AMOT overexpression (\*), showing nuclear YAP accumulation, serve as negative control. Cell and nuclear borders are outlined in yellow and blue dashed lines, respectively. Scale bar,  $20\,\mu m.\,\textbf{g}$  , Left: representative IF images of YAP/TAZ in control (wt) versus AMOT-130/AMOT-L1/AMOT-L2 triple KO (AMOT tKO) HEK293 cells in Mech.ON versus Mech.OFF conditions. Nuclei are counterstained with Hoechst (cyan). Scale bar, 20  $\mu$ m. Right: quantifications (n = 51 for wt Mech.OFF, n = 50 cells each for all other conditions, pooled from two independent seedings) of YAP/TAZ N/C subcellular localization in cells seeded as in the left panels. P < 0.0001. h, AMOT is epistatic to LINC proteins and MTs. Left: representative IF images of YAP/TAZ in control versus AMOT tKO HEK293 cells treated with the indicated siRNAs. Scale bar, 10  $\mu$ m. Right: quantifications (n = 45 for AMOTtKO siCo., n = 50 cells each for all other conditions, pooled from two independent seedings) of YAP/TAZ N/C subcellular localization in cells treated as in the left panels. P = 0.0587 for wt versus AMOTtko in siCo., P < 0.0001 for all other comparisons shown. P values were determined by unpaired two-tailed Student's t-test with Welch's correction (e) or one-way ANOVA with Welch's correction (g,h).

Is AMOT stability a mechanical rheostat responding to MT organization for YAP/TAZ regulation? To address this, we used proximity ligation assays (PLAs) to spatially map the YAP/AMOT interaction and found that this occurs exclusively in the cytoplasm of mechano-OFF cells (Fig. 3e), Moreover, supporting AMOT levels in mechano-ON cells by AMOT overexpression is sufficient to quantitatively retain YAP in the cytoplasm (Fig. 3f) and to blunt YAP/TAZ transcriptional responses (Extended Data Fig. 5k,l). YAP cytoplasmic retention relies on its direct physical association with AMOT, as demonstrated by two complementary experiments involving mutations in the known interacting domains of the two proteins: (1) expression in mechano-ON cells of AMOT versions bearing point mutations that impair YAP/TAZ binding<sup>35,36</sup> was inconsequential for YAP/TAZ activity (Extended Data Fig. 5k): (2) reconstitution of YAP/TAZ-depleted cells with a YAP-WW-mutant-unable to bind AMOT-rendered them insensitive to AMOT add-back (Extended Data Fig. 5l). Collectively, the data indicate that AMOT protein stability operates as mechanical rheostat by binding to YAP/TAZ.

Beyond gain of function, we next investigated the extent to which YAP/TAZ nuclear entry requires AMOT degradation. For this, we depleted all AMOT proteins (AMOTp130, AMOTL1 and L2) from mechano-OFF cells by triple CRISPR-mediated knockout (KO) or siR-NAs. Remarkably, AMOT depletion fully rescued YAP/TAZ nuclear entry and activity in mechano-OFF cells (Fig. 3g). We proved this for several experimental conditions, such as in cells seeded on soft substrates or small adhesive islands (Extended Data Fig. 5m,n), in cells with impaired F-actin contractility (Extended Data Fig. 50) and also in cells carrying centrosomal MTs impairment through depletion of SUN2, nesprin4 or y-tubulin (Fig. 3h). Under all these mechano-inhibitory conditions, AMOT was the downstream factor causing YAP/TAZ inhibition, as its depletion rescued YAP/TAZ nuclear localization and transcriptional activity, as measured by YAP/TAZ endogenous target genes and the YAP/TAZ/TEAD-activity synthetic reporter 8XGTIIC-Lux (Fig. 3g,h and Extended Data Fig. 5m-o).

# $\label{lem:method} \textbf{Mechanical regulation of AMOT stability relies on retrograde transport along MTs}$

We have shown that AMOT degradation in mechano-ON cells relies on the centrosome and MT radial organization, raising questions about the underlying mechanism. Proteasomal degradation of AMOT has previously been described downstream of poly-ADP ribosylation (that is, 'PARylation') by TNKS1/2 enzymes serving as a degron-tag to promote AMOT poly-ubiquitilation by the E3 ligase RNF146<sup>37</sup>. Consistently, as previously reported and here confirmed, inhibiting PARylation or depleting cells of the E3 ligase RNF146 potently supports AMOT stabilization (Extended Data Fig. 6a,b).

Given this cascade, we asked whether cell mechanics in fact regulates any of these biochemical events. Tankyrase1/2-dependent AMOT PARylation and subsequent poly-ubiquitination occur under both mechano-ON and mechano-OFF conditions, and, consistently, RNF146 protein levels and subcellular localization were also indistinguishable in mechano-ON and -OFF conditions (Extended Data Fig. 6c-f). This prompted us to consider the role of the mechanoregulated centrosomal proteasome as a determinant of AMOT stability. To test this notion, we first confirmed that AMOT protein levels in mechano-ON cells could be rescued, dose-dependently, by treatment with proteasome inhibitors (Fig. 4a). Next, we followed AMOT subcellular localization by 3D imaging in proteasome-inhibited mechano-ON cells. Notably, under these conditions, the sole AMOT protein that could be identified is indeed concentrated at centrosomal condensates (Fig. 4b). Consistently, we found that AMOT protein could be immunoprecipitated in complexes with the proteasome component 20S, and exclusively in cells seeded in mechano-ON conditions (Fig. 4c and Extended Data Fig. 6g). Thus, in mechano-ON cells, AMOT is constantly targeted to the pericentrosomal area, allowing robust, quantitative and timely control of protein levels, essential for stringent cellular mechanoresponsiveness. To quantitatively probe the rate of AMOT protein degradation in mechano-ON cells, we conducted cycloheximide pulse-and-chase experiments, showing that the entire AMOT protein pool that is stabilized by proteasome inhibitor treatment is readily degraded after proteasome inhibitor washout (Extended Data Fig. 6h).

Next, we asked how AMOT is delivered to centrosomal condensates. Interesting clues came from considering publicly available AMOT interaction datasets. We first considered recent proteome-wide reports mapping proteins that, in living cells, colocalize within the same subcellular compartment<sup>38</sup>. We retrieved AMOT exclusively in association with Hippo components, MTs and centrosome components (Extended Data Fig. 7a and Supplementary Table 2). We also considered published protein–protein interaction datasets<sup>31</sup> that suggested that all AMOT family members can form complexes with components of the dynein system (Supplementary Table 3), well known to mediate retrograde transport towards the MTOC.

Given these clues, we thus reasoned that AMOT might reach the centrosomal location through the same mechanism shared by most pericentrosomal factors, that is, by dynein-dependent retrograde transport along the MT conveyor belt15. We first approached this model from a functional perspective, asking whether interference with dynein motor activity could impact AMOT stability. For this, we inhibited dynein-mediated retrograde transport by depleting components of the dynein system. The latter is composed of two parts: the MT-binding dynein motor complex and the dynactin complex, which is the cargo-binding cofactor of this transport system<sup>39</sup>. As shown in Fig. 4d and Extended Data Fig. 7b, depletion of dynein-light chain 2, as well as of the dynactin components ARP1 or ARP11, readily results in aberrant AMOT stabilization in mechano-ON cells. Reinforcing this conclusion, a similar effect was obtained by blocking dynein-mediated retrograde transport with dynarrestin, an inhibitor of dynein association to MTs (Extended Data Fig. 7c), or with ciliobrevin D, a reversible inhibitor of dynein ATPase activity (Extended Data Fig. 7d). Importantly, AMOT stabilization is dynamically and quantitatively regulated by dynein-dependent retrograde transport towards the pericentrosomal proteasome, as AMOT is readily degraded within 4 h after ciliobrevin D washout (Extended Data Fig. 7d). Interfering with retrograde transport by depletion of dynein or dynactin components is indeed sufficient to inhibit YAP/TAZ responses (Fig. 4e and Extended Data Fig. 7e-g), as expected by the requirement of retrograde transport to blunt AMOT levels in mechano-ON cells.

The above results prompted us to test a biochemical interaction between AMOT and components of the cargo-binding dynactin complex. The latter is, in turn, composed of two multiprotein portions: an actin-like ARP1/11 filament binding to dyneins, and a projecting DCTN1 'shoulder complex', required for recruiting specific cargos<sup>40</sup>. Using cell lysates of mechano-ON cells pretreated with proteasome inhibitors, we found that pulldown of endogenous AMOT specifically co-immunoprecipitated with endogenous DCTN1, but not ARP11 or ARP1 (Fig. 4f). Of note, when bound to DCTN1, AMOT is ostensibly unable to bind YAP, as we observed interaction between endogenous AMOT and YAP exclusively under mechano-OFF conditions (Extended Data Fig. 7h).

Next, we wished to gain insights into the interaction between AMOT and DCTN1. As revealed by electron microscopy studies 40-42, DCTN1 is composed of multiple coiled-coil regions with an N-terminal CAP-Gly domain responsible, together with the basic amino-acid-rich region, for MTs binding, and a central intra-coiled-coil domain (ICD), whose functional role is still poorly understood. The structure of an AMOT peptide has been resolved by X-ray crystallography in complex with the 14-3-3 scaffold protein, an association requiring AMOT phosphorylation in pSer175<sup>43</sup> (Extended Data Fig. 7i). AlphaFold2<sup>44,45</sup> predicted with very high confidence the structure of the ICD, revealing a structural similarity between the ICD predicted structure and

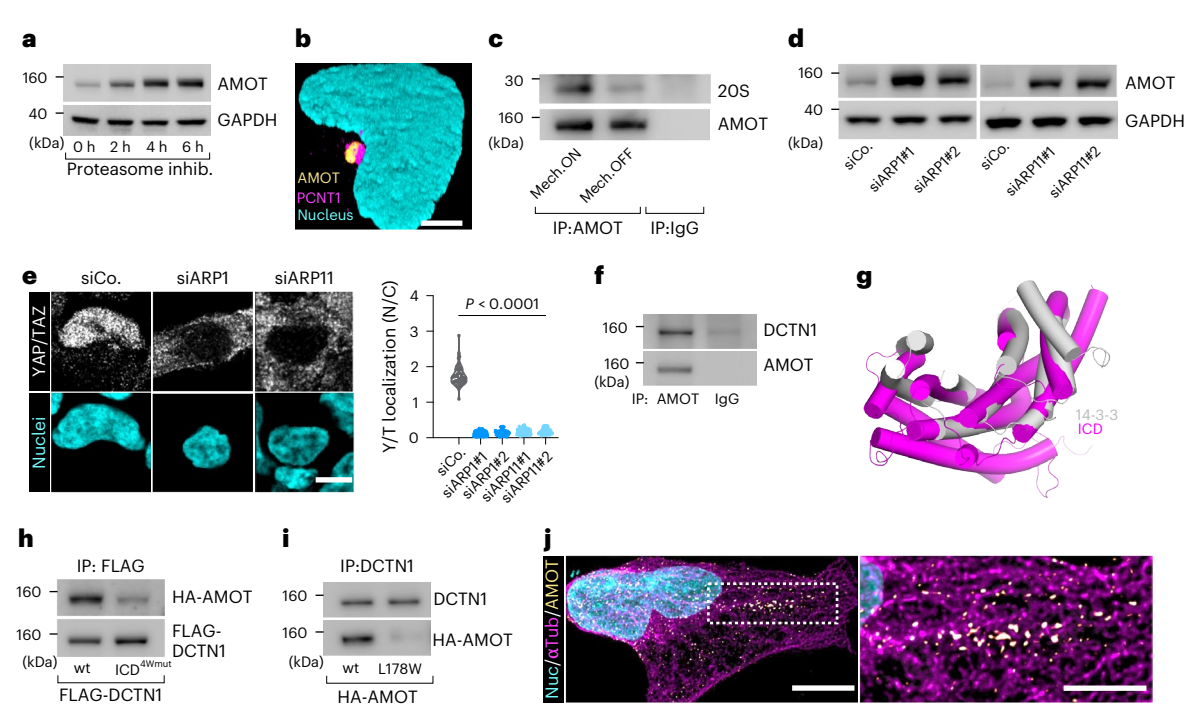


Fig. 4 | Mechanical regulation of AMOT stability relies on retrograde transport along MTs in mechano-ON cells. a, Representative AMOT immunoblot of HEK293 cells seeded in Mech.ON conditions and treated with proteasome inhibitor (lactacystin 10 μM) for the indicated timings. GAPDH serves as loading control, b. Representative 3D IF reconstructions of HEK 293 cells seeded in Mech.ON conditions treated with proteasome inhibitor (lactacystin 10  $\mu$ M, 6 h). Centrosome was labelled by pericentrin staining (PCNT1, magenta), AMOT in yellow, and the nucleus was counterstained with Hoechst (cyan). Scale bar, 5 µm. c, Pulldown of endogenous AMOT from proteasome-inhibited HEK293T cells seeded in Mech.ON versus Mech.OFF conditions, showing AMOT interaction with the proteasome component 20S exclusively under Mech.ON conditions. IgG pulldown serves as the negative control. The inputs of the same pulldown experiment are shown in Extended Data Fig. 6g. d, Representative AMOT immunoblots of HEK293 cells treated with the indicated siRNAs targeting components of the dynactin complex. GAPDH serves as loading control. e, Left: representative IF images of YAP/TAZ in HEK293 cells transfected with the indicated siRNAs. Nuclei are counterstained with Hoechst (cyan). Scale bar, 10  $\mu$ m. Right: quantifications (n = 55 for siCo., n = 50 cells each for all other conditions, pooled from two independent seedings) of YAP/TAZ N/C subcellular localization in cells treated as in the left panels, P < 0.0001, f. Pulldown of endogenous AMOT from proteasome-inhibited Mech.ON HEK293T cell lysates showing AMOT interaction with the dynactin complex component DCTN1.

IgG pulldown serves as negative control. g, Structural superposition between the 14-3-3 domain (grey) and intra-coiled-coil domain (ICD) of DCTN1/p150 (magenta). Extended Data Fig. 7j presents the predicted alignment error (PAE) plot for the complex shown here. h, Pulldown of FLAG-DCTN1 from Mech.ON HFK 293T cells transiently transfected with HA-AMOT and the indicated FLAG-DCTN1 mutants and treated with dynarrestin (10 µM) for 6 h, showing impaired interaction between AMOT and a DCTN1 mutant bearing S659W/L662W/T835W/ A839W substitutions in the ICD (ICD<sup>4W</sup> mutant). The inputs of the same pulldown experiment are shown in Extended Data Fig. 7m. i, Pulldown of endogenous DCTN1 from Mech.ON HEK293T cells transiently transfected with the indicated AMOT mutants and treated with dynarrestin 10 µM for 6 h, showing impaired interaction between DCTN1 and the AMOTL178W mutant. The inputs of the same pulldown experiment are shown in Extended Data Fig. 7n. j, Representative IF images of MTs ( $\alpha$ Tub, magenta) and endogenous AMOT (yellow) in MCF10A cells seeded in Mech.ON conditions and treated with dynarrestin (10  $\mu$ M) for 6 h. Nuclei are counterstained with Hoechst (cyan). Scale bar (left), 10 μm. The right panel shows a magnification of the dashed area in the left panel. Scale bar (right), 5 μm. Supplementary Video 3 shows live time-lapse videos showing AMOT retrograde transport along MTs in DMSO versus dynarrestin-treated MCF10A cells. P values (P < 0.0001 for siCo, versus all other samples) were determined by one-way ANOVA with with Dunnett T3 correction for multiple comparisons (e).

14-3-3, particularly striking for the structural arrangement of the helices contributing to the concave surface by which 14-3-3 associates with AMOT (Fig. 4g and Extended Data Fig. 7j,k). The structural similarity between 14-3-3 and the ICD promoted the hypothesis that AMOT might associate with the ICD using the same region centred around S175. To address this idea, we performed co-IP experiments. We found, indeed, that replacement of S659, L662, T835 and A839, located on the concave surface of the ICD (Extended Data Fig. 7k,l), with tryptophan residues impaired binding of DCTN1 to wild-type AMOT (Fig. 4h and Extended Data Fig. 7m). Conversely, the L178W AMOT variant, predicted to impair ICD association, also abolished the interaction with endogenous DCTN1 (Fig. 4i and Extended Data Fig. 7n).

Collectively, the above biochemical results support a model in which the mechanical regulation of AMOT abundance relies on its loading onto dynein–dynactin complexes and its constant retrograde delivery to the proteasomal sink along the pericentrosomal MT aster. Supporting this model, by co-staining AMOT and MTs in mechano-ON cells treated with dynarrestin, we found that AMOT forms discrete

condensates decorating MT tracks and is enriched in the pericentrosomal area (Fig. 4j). Moreover, following by live imaging the movement of AMOT condensates on MTs, we were able to directly visualize a very fast retrograde transport of red fluorescent protein (RFP)-tagged AMOT aggregates along MTs. This flow is dramatically reduced by dynarrestin treatment (Supplementary Video 3).

# A unifying model integrating mechanosignalling and the Hippo cascade

The above results offer fresh perspectives on a currently debated issue, that is, how the Hippo pathway intersects with mechanosignalling. Previous work has shown that AMOT is phosphorylated by the core Hippo kinases LATS1/2<sup>32,46,47</sup>. Here we found that LATS1/2 activity contributes to AMOT stability, as demonstrated by AMOT enhanced degradation in LATS1/2-depleted cells (Fig. 5a and Extended Data Fig. 8a). What attracted our attention was that LATS1/2 phosphorylates AMOT-130 exactly in S175 (Extended Data Fig. 8b), namely, within the same region responsible for loading AMOT on 14-3-3 (ref. 43) and on the

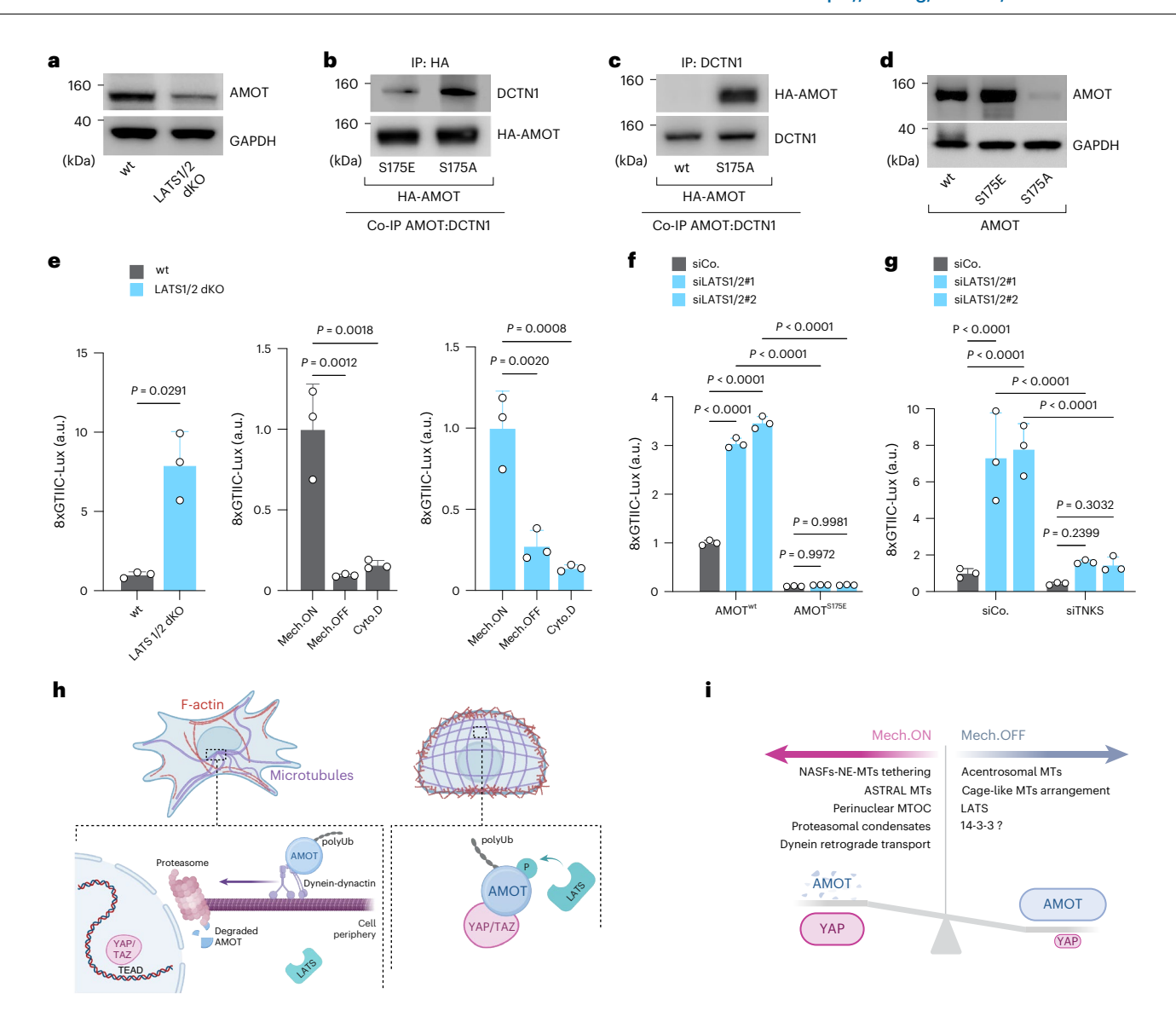


Fig. 5 | Hippo/LATS signalling regulates YAP/TAZ mechanotransduction through AMOT. a, Representative immunoblots of Mech.OFF HEK293 LATS1/2 dKO cells showing impaired AMOT stabilization upon LATS1/2 double knockout. GAPDH serves as loading control. b, Pulldown of HA-AMOT from Mech.ON HEK293T cells transiently transfected with the indicated HA-AMOT mutants and treated with lactacystin (10  $\mu$ M) for 6 h, showing lower and higher ability of the AMOT-S175E and AMOT-S175A mutants to bind to DCTN1, respectively. The inputs of the same pulldown experiment are shown in Extended Data Fig. 8c. c, Pulldown of endogenous DCTN1 from Mech.ON HEK293T cells transiently transfected with the indicated HA-AMOT mutants and treated with dynarrestin (10 µM) for 6 h, showing enhanced interaction between DCTN1 and the AMOT S175A mutant. The inputs of the same pulldown experiment are shown in Extended Data Fig. 8d. d, Representative AMOT immunoblots of HEK293 cells transiently transfected with the indicated AMOT mutants. GAPDH serves as loading control. The same experiment was repeated twice with comparable results. e. Luciferase assay of control (wt) or LATS1/2 dKO HEK293 cells transfected with a synthetic reporter for YAP/TAZ/TEAD-dependent transcription (8xGTIIC-Lux). The middle and right panels show luciferase assays performed with these same cells seeded in Mech.ON (sparse), Mech.OFF (dense) conditions or treated with Cyto.D (0.5  $\mu$ M, 15 h). Data are presented as mean + s.d. of n = 3 biologically independent samples. Left panel, P = 0.0291; middle panel, P = 0.0012 (Mech.ON versus Mech.OFF), P = 0.0018 (Mech.ON versus CytoD); right panel, P = 0.002 (Mech.ON versus Mech.OFF), P = 0.0008(Mech.ON versus CytoD). f, Luciferase assay of HEK293 cells treated with the indicated siRNAs and transfected with a synthetic reporter for YAP/TAZ/TEADdependent transcription (8xGTIIC-Lux) and with the indicated AMOT mutants.

Data are presented as mean + s.d. of n = 3 biologically independent samples. P = 0.9972 (AMOTS175E siCo. versus siLATS1/2#1), P = 0.9981 (AMOTS175E siCo. versus siLATS1/2#2), P < 0.0001 for all other comparisons shown. **g**, Luciferase assay of HEK293 cells treated with the indicated siRNAs and transfected with a synthetic reporter for YAP/TAZ/TEAD-dependent transcription (8xGTIIC-Lux). Data are presented as mean + s.d. of n = 3 biologically independent samples. P = 0.2399 (siTNKS+siCo. versus siTNKS+siLATS1/2#1), P = 0.3032 (siTNKS+siCo. versus siTNKS+siLATS1/2#2), P < 0.0001 for all other comparisons shown. **h**, Top: schematics of the cytoskeletal organization of Mech.ON (left) versus Mech.OFF (right) cells. Bottom: schematic representation of the mechano-signalling events controlling the stability of AMOT proteins. In Mech.ON cells, AMOT protein is controlled by binding to the dynein/dynactin complex, allowing fast dynein $mediated\ transport\ of\ AMOT\ through\ the\ MT\ aster\ towards\ the\ pericentrosomal$ proteasome where AMOT is locally degraded. In Mech.OFF cells, absence of a MT aster allows accrual of AMOT protein levels. Here, LATS kinase further contributes to AMOT stability by direct phosphorylation of AMOT, averting it from its degradation route. In Mech.OFF cells, increase of AMOT levels serves as a cytoplasmic sink for YAP/TAZ, impeding nuclear accumulation. Created with BioRender. i, Schematic representation of factors and cytoskeletal components  $tipping \, the \, balance \, towards \, AMOT \, degradation \, and \, YAP/TAZ \, activation \, in \, Mech.$ ON cells (shown on the left) and those that drive AMOT stabilization in Mech.OFF cells (shown on the right). Created with BioRender. P values were determined by unpaired two-tailed Student's t-test with Welch's correction (e, left panel), oneway ANOVA with Tukey's multiple comparison test (e, middle and right panels) or two-way ANOVA (f,g).

DCTN1/dynactin complex (Fig. 4g and Extended Data Fig. 7i). This raised the possibility that AMOT phosphorylation by LATS may tip the balance of these associations, averting AMOT from dynactin. To test this, we used HA-tagged AMOT phospho-mimetic AMOT-S175E and phospho-mutant AMOT-S175A constructs. We carried out reciprocal co-immunoprecipitation/western blot experiments to monitor their association with endogenous DCTN1 in cell lysates. We found that AMOT-S175E and AMOT-S175A showed lower and higher ability to bind to DCTN1, respectively (Fig. 5b,c and Extended Data Fig. 8c,d). Consistently, after dose titration and western blotting, we found that AMOT-S175E is a more stable protein than AMOTwt, whereas AMOT-S175A is readily degraded (Fig. 5d). In sum, LATS-AMOT phosphorylation represents a 'salvage' mechanism favouring AMOT escape from its degradation pathway.

The above results depict a scenario in which AMOT serves as the central rheostat of mechanical cues, also integrating key inputs from Hippo/LATS1/2 activity. Of note, by monitoring LATS1/2 activity, we also found that the levels of LATS1 autophosphorylation (a hallmark of LATS activation 48), and the very same AMOT phosphorylation by LATS, are ostensibly indistinguishable in lysates from mechano-ON and -OFF cells (Extended Data Fig. 8e). In other words, this suggests that AMOT regulation by LATS is a tonic modulation that constantly attempts to skew AMOT from degradation to stabilization, without affecting mechanoresponsiveness per se, but rather modulating its amplitude. In line with this, LATS1/2 double-knockout cells display enhanced YAP/TAZ activity but are still readily inhibited by mechano-OFF conditions or cytoskeletal inhibition (Fig. 5e).

If LATS activity converges on YAP/TAZ mechanoregulation by ultimately regulating AMOT protein levels, then we should expect YAP/ TAZ inhibition by AMOT to be formally uncoupled from LATS activity. To test this, we monitored YAP/TAZ activity in LATS1/2-depleted cells upon AMOT reconstitution. As shown in Fig. 5f, reconstitution with AMOT phosphomimicking (S175E) mutant is sufficient to render YAP/ TAZ activity insensitive to LATS1/2 depletion, implying that the effect of LATS1/2 depletion on YAP/TAZ activity is, to a substantial extent, due to modulation of AMOT degradation. If LATS operates on YAP/TAZ mechanosignalling indirectly, by saving AMOT from its degradation pathway, then stabilizing endogenous AMOT by alternative means should render LATS dispensable for YAP/TAZ inhibition. We confirmed this prediction by promoting the stabilization of endogenous AMOT by inhibiting its upstream degradation signal (that is, by depletion of TNKS1/2), finding that this renders YAP/TAZ insensitive to inhibition by LATS1/2 (Fig. 5g).

The above results also imply, at least in part, a departure from the classic modality by which the Hippo pathway has been envisioned, that is, by LATS1/2-mediated direct phosphorylation of YAP/TAZ. Indeed, in mechano-OFF conditions displaying increased AMOT levels, YAP/TAZ phosphorylation per se should be dispensable for their mechanical inhibition. In line with this, cells expressing LATS-insensitive mutant isoforms of YAP could still be readily inhibited by mechano-OFF conditions (Extended Data Fig. 8f), a result consistent with previous reports 5.10,49-59. In other words, experimentally uncoupling AMOT from its degradation pathway renders LATS1/2 marginal for mechano-dependent YAP/TAZ modulation, implying that the potent effect of LATS1/2 depletion on mechano-dependent YAP/TAZ regulation is mainly due to modulation of AMOT degradation (schematic representations are shown in Fig. 5h,i), rather than of YAP/TAZ per se.

#### Biological role of AMOT in classic mechanobiology assays

The data above imply a central functional role of AMOT for biological responses driven by YAP/TAZ mechanical regulation. We thus set out to validate this notion in classic mechanobiology assays. Mesenchymal stem cell (hMSC) differentiation towards an adipogenic fate is known to be strictly dependent on YAP/TAZ mechanical inhibition<sup>5</sup>. We found that AMOT is crucial in this context, as AMOT depletion

impairs adipogenic differentiation in mechano-OFF states (Fig. 6a and Extended Data Fig. 9a,b). Conversely, AMOT add-back is sufficient to drive adipogenic differentiation in mechano-ON mesenchymal stem cells, in which this fate is otherwise inhibited (Extended Data Fig. 9c).

Next, we asked whether YAP/TAZ inactivation by AMOT dictates the proliferation patterns of epithelial monolayers instructed by the geometrical distribution of mechanical signals. To test this, we employed microfabricated fibronectin (FN) islands of defined area <sup>10,60</sup>. In this setting, cells stretched at the border of the island are endowed with YAP/TAZ-dependent proliferation capacity. In contrast, cells at the centre of the island experience density-dependent YAP/TAZ turn off and contact-inhibition of proliferation <sup>10</sup>. Notably, we found that proliferation and YAP/TAZ patterning are driven by AMOT patterning, with AMOT depletion resulting in aberrant proliferation throughout the entire island (Fig. 6b and Extended Data Fig. 9d).

#### AMOT as mechanoregulated tumour suppressor

Mammary tumorigenesis has long been associated with increased tissue stiffness, and, consistently, several studies have proven that YAP/TAZ activation is indeed chiefly involved in mammary cell transformation and tumour growth<sup>4</sup>. Given our above results, YAP/TAZ-dependent tumorigenesis should be expected to be favoured by the destabilization of AMOT. We tested this notion in several models. Tumorigenic reprogramming of mammary luminal differentiated cells by activated oncogenes, such as overexpression of constitutively active HER2, has previously been shown to require mechanical forces in a YAP/TAZ-dependent manner 49,61,62. Here we found that such oncogene-mediated reprogramming is indeed accompanied by oncogene-induced AMOT degradation (Fig. 6c). Indeed, oncogene effects are impaired by add-back of wild-type AMOT, but not of an AMOT mutant incompetent for YAP/TAZ binding (Fig. 6d and Extended Data Fig. 9e). Consistently, we also found that triple KO (tKO) of AMOT in poorly aggressive, Ras-transformed human mammary epithelial cells (MII) potently enhanced their transformation in mechano-OFF conditions, as measured by mammosphere and soft-agar assays (Extended Data Fig. 9f,g) and confirmed by in vivo tumorigenesis assays (Fig. 6e). Coherently, we also demonstrated that the effects of AMOT depletion were strictly YAP/TAZ-dependent, as shown by concomitant AMOT and YAP/TAZ depletion or treatment with TEAD inhibitors (Extended Data Fig. 9f,g). In the opposite direction, we also proved that increasing the levels of wild-type AMOT, but not of AMOT incapable of YAP/TAZ association, impairs the tumorigenic capacities of the highly aggressive MDA-MB-231 mammary cells. This was demonstrated in vitro by inhibited soft-agar colony growth (Extended Data Fig. 9h) and in vivo by impairment of tumour formation induced by experimentally supporting AMOT levels (Fig. 6f). The role of AMOT as candidate tumour suppressor in human tumours was then validated by digital pathology-based quantification of AMOT protein levels in a cohort of chemo-naïve triple-negative breast cancer (TNBC) samples versus adjacent normal tissues. We found that AMOT is undetectable in TNBC, but present in the luminal compartment of the normal epithelium from which TNBC derives (Fig. 6g and Extended Data Fig. 10a,b). Importantly, in these patient samples, AMOT levels are invariably and quantitatively anticorrelated with YAP/TAZ nuclear localization (Fig. 6g and Extended Data Fig. 10a,b). We conclude from this collective set of biological assays that AMOT is a dominant determinant of YAP/TAZ activity, required and sufficient for cellular mechano-responses.

#### **Discussion**

One of the most fascinating and least understood aspects of cell biology is how microenvironmental mechanical cues link to a cell's shape and then to gene expression and cell behaviour. In recent years, several individual molecular steps have been linked to mechanotransduction, particularly in relation to the F-actin cytoskeleton. Yet, no discrete events can, by themselves, explain mechanosignalling, as it is the whole

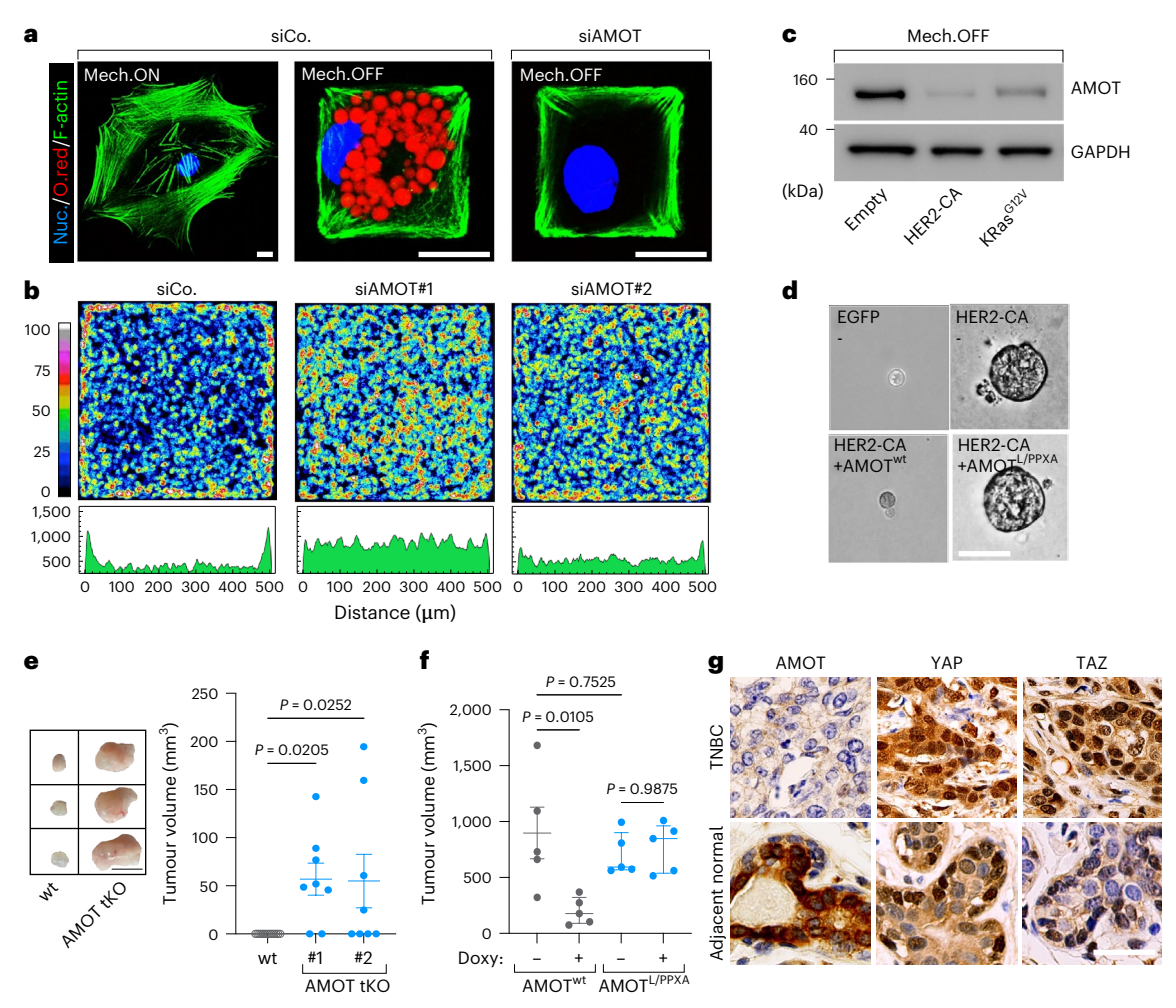


Fig. 6 | AMOT plays a central role in biological responses driven by YAP/TAZ mechanical regulation. a, Representative IF images of hMSCs seeded on spread (unconfined, Mech.ON) or small (1,000 µm<sup>2</sup>, Mech.OFF) micropatterns and treated with the indicated siRNAs. Oil Red (O.red) staining is used to identify lipid vacuoles (red), F-actin is stained with phalloidin (green) and nuclei are counterstained with Hoechst (blue). Scale bars, 15 µm. Extended Data Fig. 9a provides quantifications. b, Top: stacked images of BrdU incorporation. The colour scale indicates the extent of cell proliferation in a given position of the monolayers. Bottom: spatial mapping of the proliferation rate (BrdU signal) along the x axis of each panel shown on top (Methods). Extended Data Fig. 9d presents images of controls showing comparable densities of cells in all conditions. c, Representative AMOT immunoblots of HEK293 cells transiently transfected with empty vector or with constitutively active oncogenes and seeded in Mech.OFF conditions. GAPDH serves as loading control. d, Representative images and quantifications of colonies formed by human mammary luminal differentiated cells undergoing oncogenic reprogramming when transduced with lentiviral vectors encoding for the indicated factors. HER-CA, constitutive active HER2 mutant (Methods); AMOT point

mutant in the three L/PPXY YAP-binding motifs (Methods). Scale bar, 170  $\mu m$ . Extended Data Fig. 9e provides quantifications. e, Representative images (left) and tumour volume quantifications (right, n = 14 mice for wt and n = 8 mice each for each AMOTtko condition) of orthotopic mammary tumours formed by control or AMOT tKO MII cells. Lines represent mean  $\pm$  s.e.m. P = 0.0205(wt versus AMOTtKO#1), P = 0.0252 (wt versus AMOTtKO#2). f, Tumour volume quantifications (n = 5 mice for each condition) of orthotopic mammary tumours formed by MDA-MB-231 cells transduced with lentiviral vectors encoding for the indicated doxycycline (Doxy)-dependent AMOT mutants. Lines represent mean  $\pm$  s.e.m. P = 0.0105 (AMOT wt Doxy<sup>-</sup> versus Doxy<sup>+</sup>), P = 0.7525 (AMOT wt Doxy versus AMOT L/PPXA Doxy), P = 0.9875 (AMOT L/PPXA Doxy versus AMOT L/PPXA Doxy<sup>+</sup>). **g**, Representative immunohistochemical pictures of AMOT, YAP and TAZ proteins in chemo-naïve human TNBC samples or adjacent normal mammary tissue. Data are representative of n = 7 independent patient samples. Scale bar, 50 µm. Extended Data Fig. 10a presents lower magnifications of the same samples and Extended Data Fig. 10b quantifications of immunohistochemical staining in all tested samples. Pvalues were determined by one-way ANOVA with Tukey's multiple comparison test (e,f).

cell that integrates its response to forces across scales and organelles to determine its own mechanical state. Here we reveal that distinct subcellular structures are part of a mechanical continuum converging to regulate AMOT protein stability, and, in turn, YAP/TAZ mechanosignalling. AMOT proteins act as the long-sought cytoplasmic sink for YAP/TAZ. AMOT regulation represents an energy-consuming but efficient system to readily shift a constantly produced YAP/TAZ inhibitor from degradation to accumulation. This requires a swift adaptation of the cell to changes in its physical microenvironment.

We show that distinct cytoskeletal and cytoskeletal-associated structures act as an integrated whole to transduce forces. In particular,

we demonstrate the essential role of MTs as pillars of cellular mechanosignalling on par with, and downstream of, the F-actin cytoskeleton. Here we show that the cellular response to mechanical cues imposes a dramatic restructuring of the MTOC and of MT spatial organization (Fig. 5h,i). In mechanically inhibited cells, MTs are acentrosomal, with their minus-end oriented at the cell periphery, and structured as a lattice that surrounds the nucleus. MTs radiating from the cell centre in mechano-ON cells emanate from the perinuclear centrosome, generating a polarized astral arrangement that, in turn, facilitates further spreading from the Golgi complex 63-66. This MT arrangement is essential for dynein-mediated transport of AMOT, which occurs by

direct binding of AMOT to the dynactin component DCTN1, at the level of its ICD.

We propose that in mechano-ON cells, the centrosome, with its dual function of serving as MTOC and as physical scaffold for concentrating protein degradation, is a mechanoregulated cellular structure essential for YAP/TAZ regulation. We show that centrosome formation mediates the effects of rigidity sensing downstream of ECM adhesion and stress fibre formation. Three lines of evidence support this conclusion. First, specific disruption of radial MTs emanating from the centrosome in mechanically challenged cells prevents AMOT degradation and YAP/TAZ activation. Second, boosting stress fibre formation is inconsequential for YAP/TAZ activation in cells with inhibited radial MTs. Third, inducing MTOC formation in F-actin-depleted cells through NLP1 overexpression is sufficient to restore AMOT degradation and YAP/TAZ nuclear entry. It is worth noting that, in mechano-OFF cells-the typical cell state of epithelial monolayers-increased F-actin cortical tension across cell-cell junctions may also influence MT orientation by repositioning MTOC components from the centrosome to apical or cortical structures, or by contributing to the stabilization of cortex-associated MT minus-ends through γ-tubulin puncta<sup>67,68</sup>. These mechanisms may further contribute to a diminished AMOT delivery to the proteasome at the cell centre.

An appealing aspect of our findings is provision of a unifying model that mechanistically merges the activity of the two main inputs feeding on YAP/TAZ activity, the Hippo cascade and mechanosignalling. The current model by which Hippo kinases regulate YAP/TAZ is through direct YAP/TAZ phosphorylation, whose inhibitory mechanisms remain incompletely defined, spanning from regulation of protein stability to tuning association with undefined cytoplasmic anchors<sup>48</sup>. In the context of mechanosignalling, however, our data provide, at least in part, a departure from this model, as we show that LATS phosphorylation of AMOT is a dominant layer by which the Hippo cascade regulates YAP/ TAZ. AMOT phosphorylation by LATS1/2 is constitutive: on the one hand, this is known to favour its association with 14-3-3 (ref. 43); on the other, as shown here, in mechano-ON cells, this phosphorylation is skewing AMOT away from its cell shape-MTs-centrosome-dependent degradation route. In other words, by hindering fast AMOT retrograde transport and degradation, LATS1/2 tip the balance to regenerate an AMOT pool. We speculate that AMOT salvage may be further reinforced by AMOT association with 14-3-3 (ref. 43). In other words, the potent effect of Hippo signalling on YAP/TAZ mechanotransduction appears overly indirect, by promoting AMOT stabilization and dampening the amplitude of mechanosensing. This leaves open intriguing questions on how, and in which contexts, YAP/TAZ direct phosphorylation by LATS may further tune YAP/TAZ mechanoresponsiveness, for example, in the context of LATS regulation mediated by GPCR signalling, cell-cell junctions and by polarity complexes in epithelial cells.

Our data support the leading role of the NE in cellular mechanotransduction <sup>16,17,22</sup>. On the one hand, we show that the NE serves as a hub mediating the physical and tensional connectivity between the F-actin and MTs cytoskeletal systems through distinct LINC complexes. The role of NASF as preferred F-actin subpool to mechanically tether the NE, here investigated primarily in epithelial cell types, may be further reinforced by more dorsal 'actin-cap'-like fibres that are specific to other cell types, chiefly fibroblasts<sup>69</sup>. On the other hand, laminopathies and LINC defects converge in inducing aging-related defects³, and, intriguingly, the same is true for genetic disorders that impact MTOC tethering to the NE, such as mutations in ninein (for example, Seckel disease)<sup>70</sup>. Our data may thus offer a point of convergence between these apparently unrelated observations, particularly considering the recently discovered role of declining YAP/TAZ activity in ageing and senescence<sup>71</sup>.

Recent studies have proposed that the permeability of nuclear pores can regulate the nuclear entry of YAP/TAZ $^{51}$ . Clearly, the regulatory layer provided by the nuclear permeability model may coexist with

the molecular regulation of YAP/TAZ by cytoplasmic sinks, particularly through mechanisms centred on the stability of the AMOT protein as here proposed. We further note that the nuclear permeability model may contribute to YAP/TAZ regulation only in the mechano-ON cell state, but it can hardly explain the control of mechanosignalling in the resting, mechano-OFF state. Indeed, in cells experiencing soft substrates—that is, cells with predicted less permissive nuclear pores experimental loss of AMOT nevertheless massively increases YAP nuclear entry. In other words, our results point to an overarching regulation of YAP/TAZ cytoplasmic retention determined by AMOT levels. Of note, the nuclear permeability model relates to the low or zero AMOT of the mechano-ON cell state, as it was proposed in studies in which cells were experiencing levels of ECM rigidity (for example, greater than 5 kPa)<sup>51</sup> that we have shown are sufficient to deplete cells of their AMOT protein pool (Fig. 3c). Moreover, experimental stabilization of AMOT in mechano-ON cells is sufficient to effectively oppose YAP/TAZ nuclear entry, despite more permissive nuclear pores. Taken together, these results paint a picture in which YAP/TAZ subcellular localization is dictated by AMOT stability in mechano-ON versus -OFF states, but can be further controlled by a second regulatory layer, at the level of nuclear pores in AMOT-low mechano-ON cells.

We speculate that AMOT availability in normal epithelia may spatially confine YAP/TAZ activation to specific locations and cell states, at the same time preventing unscheduled YAP/TAZ activation with its associated tumorigenic potential<sup>4</sup>. Here we show that AMOT is a novel candidate tumour suppressor acting through YAP/TAZ inhibition, raising the tempting possibility that pharmacological treatments aimed at supporting AMOT stabilization may represent promising avenues for cancer therapy. Probing the structural pockets of AMOT–DCTN1 association may represent an interesting route for YAP/TAZ inhibition.

#### Online content

Any methods, additional references, Nature Portfolio reporting summaries, source data, extended data, supplementary information, acknowledgements, peer review information; details of author contributions and competing interests; and statements of data and code availability are available at https://doi.org/10.1038/s41556-025-01773-z.

#### References

- Humphrey, J. D., Dufresne, E. R. & Schwartz, M. A. Mechanotransduction and extracellular matrix homeostasis. Nat. Rev. Mol. Cell Biol. 15, 802–812 (2014).
- Kim, S., Uroz, M., Bays, J. L. & Chen, C. S. Harnessing mechanobiology for tissue engineering. Dev. Cell 56, 180–191 (2021).
- 3. Phillip, J. M., Aifuwa, I., Walston, J. & Wirtz, D. The mechanobiology of aging. *Annu. Rev. Biomed. Eng.* **17**, 113–141 (2015).
- Piccolo, S., Panciera, T., Contessotto, P. & Cordenonsi, M. YAP/ TAZ as master regulators in cancer: modulation, function and therapeutic approaches. *Nat. Cancer* 4, 9–26 (2023).
- Dupont, S. et al. Role of YAP/TAZ in mechanotransduction. *Nature* 474, 179–183 (2011).
- Panciera, T., Azzolin, L., Cordenonsi, M. & Piccolo, S. Mechanobiology of YAP and TAZ in physiology and disease. Nat. Rev. Mol. Cell Biol. 18, 758–770 (2017).
- 7. Manning, S. A., Kroeger, B. & Harvey, K. F. The regulation of Yorkie, YAP and TAZ: new insights into the Hippo pathway. *Development* **147**, dev179069 (2020).
- 8. Del Pozo, M. A., Lolo, F. N. & Echarri, A. Caveolae: mechanosensing and mechanotransduction devices linking membrane trafficking to mechanoadaptation. *Curr. Opin. Cell Biol.* **68**, 113–123 (2021).
- Gauthier, N. C. & Roca-Cusachs, P. Mechanosensing at integrin-mediated cell-matrix adhesions: from molecular to integrated mechanisms. *Curr. Opin. Cell Biol.* 50, 20–26 (2018).

- Aragona, M. et al. A mechanical checkpoint controls multicellular growth through YAP/TAZ regulation by actin-processing factors. Cell 154, 1047–1059 (2013).
- Aureille, J. et al. Focal adhesions are controlled by microtubules through local contractility regulation. EMBO J. 43, 2715–2732 (2024).
- Seetharaman, S. et al. Microtubules tune mechanosensitive cell responses. *Nat. Mater.* 21, 366–377 (2022).
- Matis, M. The mechanical role of microtubules in tissue remodeling. *Bioessays* 42, e1900244 (2020).
- Meiring, J. C. M., Shneyer, B. I. & Akhmanova, A. Generation and regulation of microtubule network asymmetry to drive cell polarity. Curr. Opin. Cell Biol. 62, 86–95 (2020).
- Gudimchuk, N. B. & McIntosh, J. R. Regulation of microtubule dynamics, mechanics and function through the growing tip. Nat. Rev. Mol. Cell Biol. 22, 777–795 (2021).
- Maurer, M. & Lammerding, J. The driving force: nuclear mechanotransduction in cellular function, fate and disease. *Annu. Rev. Biomed. Eng.* 21, 443–468 (2019).
- Uhler, C. & Shivashankar, G. V. Regulation of genome organization and gene expression by nuclear mechanotransduction. *Nat. Rev. Mol. Cell Biol.* 18, 717–727 (2017).
- Gandin, A. et al. YAP/TAZ mechanotransduction is a fast cellular response to subnuclear adhesions revealed by mechanically dynamic substrates. Preprint at https://www.biorxiv.org/content/ 10.1101/2025.06.04.656127v1 (2025).
- Brusatin, G., Panciera, T., Gandin, A., Citron, A. & Piccolo, S. Biomaterials and engineered microenvironments to control YAP/ TAZ-dependent cell behaviour. Nat. Mater. 17, 1063–1075 (2018).
- Andreu-Carbo, M., Egoldt, C., Velluz, M. C. & Aumeier, C. Microtubule damage shapes the acetylation gradient. Nat. Commun. 15, 2029 (2024).
- Casenghi, M. et al. Polo-like kinase 1 regulates Nlp, a centrosome protein involved in microtubule nucleation. Dev. Cell 5, 113–125 (2003).
- Hale, C. M. et al. Dysfunctional connections between the nucleus and the actin and microtubule networks in laminopathic models. *Biophys. J.* 95, 5462–5475 (2008).
- Ihalainen, T. O. et al. Differential basal-to-apical accessibility of lamin A/C epitopes in the nuclear lamina regulated by changes in cytoskeletal tension. *Nat. Mater.* 14, 1252–1261 (2015).
- 24. Gerlitz, G., Reiner, O. & Bustin, M. Microtubule dynamics alter the interphase nucleus. *Cell. Mol. Life Sci.* **70**, 1255–1268 (2013).
- Zhao, T., Graham, O. S., Raposo, A. & St Johnston, D. Growing microtubules push the oocyte nucleus to polarize the *Drosophila* dorsal-ventral axis. *Science* 336, 999–1003 (2012).
- Acebron, S. P., Karaulanov, E., Berger, B. S., Huang, Y. L. & Niehrs, C. Mitotic wnt signaling promotes protein stabilization and regulates cell size. *Mol. Cell* 54, 663–674 (2014).
- Fuentealba, L. C. et al. Integrating patterning signals: Wnt/ GSK3 regulates the duration of the BMP/Smad1 signal. Cell 131, 980–993 (2007).
- Vora, S. M. & Phillips, B. T. The benefits of local depletion: the centrosome as a scaffold for ubiquitin-proteasome-mediated degradation. Cell Cycle 15, 2124–2134 (2016).
- Wigley, W. C. et al. Dynamic association of proteasomal machinery with the centrosome. J. Cell Biol. 145, 481–490 (1999).
- Totaro, A., Panciera, T. & Piccolo, S. YAP/TAZ upstream signals and downstream responses. Nat. Cell Biol. 20, 888–899 (2018).
- 31. Oughtred, R. et al. The BioGRID database: a comprehensive biomedical resource of curated protein, genetic and chemical interactions. *Protein Sci.* **30**, 187–200 (2021).
- Chan, S. W. et al. Hippo pathway-independent restriction of TAZ and YAP by angiomotin. J. Biol. Chem. 286, 7018–7026 (2011).
- 33. Wang, L. et al. Multiphase coalescence mediates Hippo pathway activation. *Cell* **185**, 4376–4393 e4318 (2022).

- Mana-Capelli, S., Paramasivam, M., Dutta, S. & McCollum, D. Angiomotins link F-actin architecture to Hippo pathway signaling. Mol. Biol. Cell 25, 1676–1685 (2014).
- 35. Yi, C. et al. The p130 isoform of angiomotin is required for Yap-mediated hepatic epithelial cell proliferation and tumorigenesis. Sci. Signal. **6**, ra77 (2013).
- 36. Zhao, B. et al. Angiomotin is a novel Hippo pathway component that inhibits YAP oncoprotein. *Genes Dev.* **25**, 51–63 (2011).
- Wang, W. et al. Tankyrase inhibitors target YAP by stabilizing angiomotin family proteins. Cell Rep. 13, 524–532 (2015).
- 38. Go, C. D. et al. A proximity-dependent biotinylation map of a human cell. *Nature* **595**, 120–124 (2021).
- Reck-Peterson, S. L., Redwine, W. B., Vale, R. D. & Carter, A. P. The cytoplasmic dynein transport machinery and its many cargoes. *Nat. Rev. Mol. Cell Biol.* 19, 382–398 (2018).
- 40. Singh, K. et al. Molecular mechanism of dynein-dynactin complex assembly by LIS1. Science **383**, eadk8544 (2024).
- 41. Saito, K. et al. Conformational diversity of dynactin sidearm and domain organization of its subunit p150. *Mol. Biol. Cell* **31**, 1218–1231 (2020).
- 42. Urnavicius, L. et al. The structure of the dynactin complex and its interaction with dynein. *Science* **347**, 1441–1446 (2015).
- Centorrino, F., Andlovic, B., Cossar, P., Brunsveld, L. & Ottmann, C. Fragment-based exploration of the 14-3-3/Amot-p130 interface. Curr. Res. Struct. Biol. 4, 21–28 (2022).
- 44. Jumper, J. et al. Highly accurate protein structure prediction with AlphaFold. *Nature* **596**, 583–589 (2021).
- 45. Mirdita, M. et al. ColabFold: making protein folding accessible to all. *Nat. Methods* **19**, 679–682 (2022).
- 46. Adler, J. J. et al. Amot130 adapts atrophin-1 interacting protein 4 to inhibit yes-associated protein signaling and cell growth. *J. Biol. Chem.* **288**, 15181–15193 (2013).
- Dai, X. et al. Phosphorylation of angiomotin by Lats1/2 kinases inhibits F-actin binding, cell migration and angiogenesis. J. Biol. Chem. 288, 34041–34051 (2013).
- 48. Ma, S., Meng, Z., Chen, R. & Guan, K. L. The Hippo pathway: biology and pathophysiology. *Annu. Rev. Biochem.* **88**, 577–604 (2019)
- Panciera, T. et al. Reprogramming normal cells into tumour precursors requires ECM stiffness and oncogene-mediated changes of cell mechanical properties. *Nat. Mater.* 19, 797–806 (2020).
- Das, A., Fischer, R. S., Pan, D. & Waterman, C. M. YAP nuclear localization in the absence of cell-cell contact is mediated by a filamentous actin-dependent, myosin II- and phospho-YAP-independent pathway during extracellular matrix mechanosensing. J. Biol. Chem. 291, 6096–6110 (2016).
- Elosegui-Artola, A. et al. Force triggers YAP nuclear entry by regulating transport across nuclear pores. Cell 171, 1397–1410 e1314 (2017).
- 52. Esposito, D. et al. ROCK1 mechano-signaling dependency of human malignancies driven by TEAD/YAP activation. *Nat. Commun.* **13**, 703 (2022).
- 53. Feng, X. et al. Hippo-independent activation of YAP by the GNAQ uveal melanoma oncogene through a trio-regulated rho GTPase signaling circuitry. *Cancer Cell* **25**, 831–845 (2014).
- 54. Reginensi, A. et al. Yap- and Cdc42-dependent nephrogenesis and morphogenesis during mouse kidney development. *PLoS Genet.* **9**, e1003380 (2013).
- 55. Silvis, M. R. et al. α-catenin is a tumor suppressor that controls cell accumulation by regulating the localization and activity of the transcriptional coactivator Yap1. *Sci. Signal.* **4**, ra33 (2011).
- 56. Sorrentino, G. et al. Metabolic control of YAP and TAZ by the mevalonate pathway. *Nat. Cell Biol.* **16**, 357–366 (2014).
- 57. Taniguchi, K. et al. A gp130-Src-YAP module links inflammation to epithelial regeneration. *Nature* **519**, 57–62 (2015).

- Wada, K., Itoga, K., Okano, T., Yonemura, S. & Sasaki, H. Hippo pathway regulation by cell morphology and stress fibers. *Development* 138, 3907–3914 (2011).
- Nakajima, H. et al. Flow-dependent endothelial YAP regulation contributes to vessel maintenance. *Dev. Cell* 40, 523–536 e526 (2017).
- 60. Nelson, C. M. et al. Emergent patterns of growth controlled by multicellular form and mechanics. *Proc. Natl Acad. Sci. USA* **102**, 11594–11599 (2005).
- Cordenonsi, M. et al. The Hippo transducer TAZ confers cancer stem cell-related traits on breast cancer cells. Cell 147, 759–772 (2011).
- Panciera, T. et al. Induction of expandable tissue-specific stem/ progenitor cells through transient expression of YAP/TAZ. Cell Stem Cell 19, 725–737 (2016).
- 63. van Grinsven, E. J. & Akhmanova, A. Diversity of microtubule arrays in animal cells at a glance. *J. Cell Sci.* **138**, JCS263476 (2025).
- 64. Frye, K. et al. Cell cycle-dependent dynamics of the Golgicentrosome association in motile cells. *Cells* **9**, 1069 (2020).
- Gavilan, M. P. et al. The dual role of the centrosome in organizing the microtubule network in interphase. EMBO Rep. 19, e45942 (2018).
- 66. Hurtado, L. et al. Disconnecting the Golgi ribbon from the centrosome prevents directional cell migration and ciliogenesis. *J. Cell Biol.* **193**, 917–933 (2011).
- 67. Sanchez, A. D. & Feldman, J. L. Microtubule-organizing centers: from the centrosome to non-centrosomal sites. *Curr. Opin. Cell Biol.* **44**, 93–101 (2017).
- Sumigray, K. D., Foote, H. P. & Lechler, T. Noncentrosomal microtubules and type II myosins potentiate epidermal cell adhesion and barrier formation. J. Cell Biol. 199, 513–525 (2012).

- Khatau, S. B. et al. A perinuclear actin cap regulates nuclear shape. Proc. Natl Acad. Sci. USA 106, 19017–19022 (2009).
- 70. Dauber, A. et al. Novel microcephalic primordial dwarfism disorder associated with variants in the centrosomal protein ninein. *J. Clin. Endocrinol. Metab.* **97**, E2140–E2151 (2012).
- Sladitschek-Martens, H. L. et al. YAP/TAZ activity in stromal cells prevents ageing by controlling cGAS-STING. *Nature* 607, 790–798 (2022).

**Publisher's note** Springer Nature remains neutral with regard to jurisdictional claims in published maps and institutional affiliations.

Open Access This article is licensed under a Creative Commons Attribution-NonCommercial-NoDerivatives 4.0 International License, which permits any non-commercial use, sharing, distribution and reproduction in any medium or format, as long as you give appropriate credit to the original author(s) and the source, provide a link to the Creative Commons licence, and indicate if you modified the licensed material. You do not have permission under this licence to share adapted material derived from this article or parts of it. The images or other third party material in this article are included in the article's Creative Commons licence, unless indicated otherwise in a credit line to the material. If material is not included in the article's Creative Commons licence and your intended use is not permitted by statutory regulation or exceeds the permitted use, you will need to obtain permission directly from the copyright holder. To view a copy of this licence, visit http://creativecommons.org/licenses/by-nc-nd/4.0/.

© The Author(s) 2025

#### Methods

Animal experiments were performed while adhering to our institutional guidelines as approved by the animal welfare body (Organismo Preposto al Benessere Animale; OPBA). Discarded tissue from anonymized healthy women undergoing reduction mastoplasty surgery and human TNBC archival samples were collected with informed consent according to our institutional guidelines and the Azienda Ospedaliera di Padova Ethics Committee (CESC).

#### Plasmids and reagents

LatrunculinA, cytochalasin D, dynarrestin, doxycycline, MG132 (Z-Leu-Leu-Leu-al), MG115 (Z-Leu-Leu-Norvalinal), dasatinib and XAV939 were sourced from Sigma. WIKI4 and JW55 were from EMD Millipore. Lactacystin was from Santa Cruz Biotechnology. Fasudil was from Tocris Bioscience. Defactinib, vincristine, nocodazole, ciliobrevin D and cycloheximide were from Selleckchem. VT107, GNE6640 and P005091 were from MedChemExpress. Rho inhibitor 1 (exoenzyme C3 transferase) was from Cytoskeleton. A complete list of the plasmids used is provided in Supplementary Table 4.

#### Cell culture

MCF10A cells were a gift from F. Miller (Karmanos) and were cultured in Dulbecco's modified Eagle medium (DMEM)/F12 (Gibco) with 5% horse serum, glutamine and antibiotics, freshly supplemented with insulin (Sigma-Aldrich), hEGF (Peprotech), hydrocortisone (Sigma-Aldrich) and cholera toxin (Sigma-Aldrich). MCF10A-YAP-eGFP-KI cells were a gift from J. T. Liphardt<sup>72</sup>, and were cultured as MCF10A. MII cells were a gift from S. Santner<sup>73</sup>, and were cultured as MCF10A. HEK293 (ATCC CRL-1573) and HEK293T (ATCC CRL-3216) cells were from ATCC and were cultured in DMEM (Gibco) supplemented with 10% fetal bovine serum (FBS), glutamine and antibiotics. U2OS (ATCC HTB-96) cells were from ATCC and were cultured in DMEM (Gibco) supplemented with 10% FBS, glutamine and antibiotics. MDA-MB-231 (ICLC HTL99004) cells were from ICLC, and were cultured in DMEM/F12 (Gibco) supplemented with 10% FBS, glutamine and antibiotics. Bone marrow-derived hMSCs were purchased from Lonza (C-12974) and grown according to the manufacturer's instructions. HEK293 LATS double knockout (dKO c) ells were a gift from K. L. Guan<sup>74</sup>, and cultured as HEK293.

NLP-expressing HEK293 cells were obtained by transduction with plenti-NLP-c-Myc-DDK-P2A-puro followed by puromycin selection, and were cultured in DMEM (Gibco) supplemented with 10% FBS, glutamine and antibiotics.

RFP-AMOT-expressing MCF10A-YAP-eGFP-KI cells were obtained by transduction with doxycycline-inducible lentiviral construct (pcw57.1-RFP-AMOTL1), and were cultured in DMEM/F12 (Gibco) with 5% horse serum, glutamine and antibiotics, freshly supplemented with insulin (Sigma-Aldrich), hEGF (Peprotech), hydrocortisone (Sigma-Aldrich) and cholera toxin (Sigma-Aldrich). Doxycycline (2  $\mu g$  ml $^{-1}$ ) was administered to cells 24 h before the experiments to induce RFP-AMOT overexpression.

HEK293 AMOT tKO cells were obtained by CRISPR-Cas-mediated gene editing, by transfection of pSpCas9(BB)-2A-puro-AMOTtKO-A or pSpCas9(BB)-2A-puro-sgGFP as negative control, using TRANS-IT LT1 transfection reagent following the manufacturer's instructions. Cells were selected by puromycin and, after three weeks, independent clonal cell lines (control, AMOT tKO#1 and AMOT tKO#2) were picked, expanded and tested by immunoblotting. HEK293 AMOT tKO cells were cultured as HEK293 cells.

HA-AMOT<sup>wt</sup> and HA-AMOT<sup>L/PPXA</sup>-expressing MDA-MB-231 cells were obtained by transduction with doxycycline-inducible lentiviral constructs (pcw57.1-HA-AMOT<sup>wt</sup> or pcw57.1-HA-AMOT<sup>L/PPXA</sup>), and were cultured in DMEM/F12 (Gibco) supplemented with 10% tetracycline-free FBS, glutamine and antibiotics. Doxycycline (2  $\mu$ g ml $^{-1}$ ) was administered to cells 24–48 h before the experiments to induce HA-AMOT<sup>wt</sup> or HA-AMOT<sup>L/PPXA</sup> expression.

MII AMOT tKO cells were obtained by CRISPR-Cas-mediated gene editing by nucleofection using Amaxa 4D nucleofector (Lonza) with pSpCas9(BB)-2A-puro-AMOTtKO-B or pSpCas9(BB)-2A-puro-sgGFP as negative control. Cells were selected by puromycin and, after three weeks, independent clonal cell lines (control, AMOT tKO#1 and AMOT tKO#2) were picked, expanded and tested by immunoblotting. MII AMOT tKO cells were cultured as MII cells. Guide RNA (gRNA) sequences are provided in Supplementary Table 5.

AMOT-expressing hMSCs were obtained by transduction with doxycycline-inducible lentiviral constructs pcw57.1-HA-AMOT<sup>wt</sup> and were treated with doxycycline (2  $\mu$ g ml<sup>-1</sup>) throughout the entire duration of adipogenic differentiation assays.

RFP-AMOT-expressing HEK293 cells were obtained by transduction with doxycycline-inducible lentiviral constructs (pcw57.1-RFP-AMOTL1) and cultured in DMEM (Gibco) supplemented with 10% tetracycline-free FBS, glutamine and antibiotics. Doxycycline (0.33  $\mu g\ ml^{-1}$ ) was administered to cells 24 h before the experiments to induce mild RFP-AMOT expression.

FLAG-YAPwt- and FLAG-YAP5SA-expressing MCF10A cells were obtained by transduction with doxycycline-inducible lentiviral constructs (pcw57.1-FLAG-YAP $^{\rm wt}$  or pcw57.1-FLAG-YAP $^{\rm SSA}$ ) and cultured as MCF10A cells. Doxycycline (0.04 and 0.2  $\mu g$  ml $^{-1}$ ) was administered to cells 24–48 h before the experiments to induce comparable expression of FLAG-YAPwt and FLAG-YAP5SA, respectively.

All parental cell lines were authenticated by BMR Genomics. All cell lines were routinely tested to exclude mycoplasma contamination.

#### **RNA interference and DNA transfections**

siRNA transfections were performed with Lipofectamine RNAi-MAX (Thermo Fisher Scientific) in antibiotic-free medium according to the manufacturer's instructions. The sequences of the siRNAs are provided in Supplementary Table 5. Validations of siRNAs efficiency are provided in Supplementary Fig. 2. DNA transfections were performed with TransitLT1 reagent (Mirus Bio) according to the manufacturer's instructions. For dual siRNA/DNA transfections, DNA transfections were performed 8 hafter siRNA transfection. For dual siRNA transfections, transfections were performed 8 hapart. Cells were collected 48 h post siRNA or DNA transfection, unless differently specified.

#### **Human mammary tissue**

Discard tissue from anonymized healthy women undergoing reduction mastoplasty surgery and human TNBC archival samples were collected with informed consent according to our institutional guidelines and the Azienda Ospedaliera di Padova Ethics Committee (CESC).

#### Human mammary luminal cell isolation and culturing

Single-cell suspensions of primary human mammary cells were generated as previously described<sup>49</sup>, with minor modifications. Briefly, the ductal tree was mechanically minced and enzymatically digested in tissue dissociation medium (Advanced DMEM-F12 supplemented with HEPES, 1.5% GlutaMAX, 600 U ml<sup>-1</sup> collagenase and 200 U ml<sup>-1</sup> hyaluronidase at 37 °C overnight). Cells were spun down for 3 min at 700 r.p.m., and the pellet was further dissociated in 0.25% trypsin-ethylenediaminetetraacetic acid (EDTA) for 5 min followed by the addition of 5 μg ml<sup>-1</sup> dispase and 1 μg ml<sup>-1</sup> DNasel for a further 10 min. Digestion was stopped in advanced DMEM 10% FBS, and the cells were filtered through a 40-µm strainer to remove residual tissue fragments and cell aggregates. Single-cell suspensions of primary mammary cells were stained with CD31 (BioLegend no. 303119), CD45 (BD Biosciences no. 557833), CD49f (BD Biosciences no. 555736) and EpCAM (BD Biosciences no. 347197) in DMEM for 30 min at 4 °C. After excluding CD31<sup>+</sup> CD45<sup>+</sup> (Lin<sup>+</sup>) cells, mammary cells were sorted into four populations using a FACS Aria III system (BD Biosciences), as previously shown<sup>49</sup>: luminal differentiated cells, CD49f<sup>-</sup>EpCAM<sup>+</sup>; luminal progenitor cells, CD49f<sup>+</sup>EpCAM<sup>+</sup>; basal cells, CD49f<sup>+</sup>EpCAM<sup>-</sup>; stromal

cells, CD49f<sup>-</sup>EpCAM<sup>-</sup>. Supplementary Fig. 3 presents the gating strategy. Freshly isolated primary luminal differentiated cells were seeded in human mammary epithelial growth medium (HMGM; advanced DMEM/F12 supplemented with HEPES, GlutaMAX, 0.5% FBS, 4 µl ml<sup>-1</sup> bovine pituitary extract (BPE), 10 ng ml<sup>-1</sup> human epidermal growth factor (hEGF), 10 μM Y27632,10 μM forskolin and antibiotics). After FACS purification, cells were seeded in 24-well plates coated with collagen I and transduced with lentiviral vectors (the virus suspension was mixed 1:1 with the medium). For primary mammary cell reprogramming, cells were transduced for 48 h with FU-tetO-HER2-CA in combination with reverse tetracycline transactivator (rtTA)-encoding lentiviruses (FudeltaGW-rtTA) and with FU-tetO-AMOT<sup>wt</sup> or FU-tetO-AMOT<sup>L/PPXA</sup>. As a (negative) control, cells were transduced with enhanced green fluorescent protein (EGFP)-expressing vector (FUW-tetO-EGFP) in combination with rtTA-encoding lentiviruses. After infection, adherent cells were washed and treated with 2 µg ml<sup>-1</sup> doxycycline for seven days in HMGM to activate tetracycline-inducible gene expression. After one week, mammary cells were detached with trypsin and seeded at a density of 2,000 cells per well in 24-well ultralow-attachment plates (Corning) in mammary clonogenic suspension medium (advanced DMEM/F12 containing HEPES, GlutaMAX, antibiotics, 5% matrigel, 2% FBS, 10 ng ml<sup>-1</sup> human EGF, 4 μl ml<sup>-1</sup> BPE, 10 μM forskolin and 2 μg ml<sup>-1</sup> doxycycline). Primary colonies were counted 14 days after seeding.

#### Orthotopic mammary fat pad transplantations

MII, MII-AMOTtKO, MDA-MB-231 and AMOT-expressing MDA-MB-231 cellular suspensions (1 × 106 per mouse) in 50% matrigel/phosphate buffered saline (PBS)1x were injected into the inguinal mammary fat pads of female non-obese diabetic severe combined immunodeficient (NOD-SCID) mice (IMSR no. CRL:394, Charles River) at three weeks of age. For the experiments in Fig. 6f, animals were then administered doxycycline (2 mg ml $^{-1}$ in water supplemented with 10 mg ml $^{-1}$ sucrose) in their drinking water for four weeks. Eight weeks (for MII cells) and four weeks (for MDA-MB-231 cells) after injection, mice were euthanized to extract tumour masses, and the tumour mass volume was measured by caliper measurements of the three major axes.

#### Microfabrications

Fibronectin-coated hydrogels were obtained as previously described with minor modifications. Hydrogel formulations in acrylamide (AA), bis-acrilamide (BA), tetramethylethylenediamine (TEMED) and ammonium persulfate (APS) were as follows: 3.5% wt/vol AA, 0.03% wt/vol BA, 1:1,000 vol/vol TEMED and 0.1% wt/vol APS (0.7 kPa); 3% wt/vol AA, 0.15% wt/vol BA, 1:1,000 vol/vol TEMED and 0.1% wt/vol APS (3 kPa); 5% wt/vol AA, 0.225% wt/vol BA, 1:1,000 vol/vol TEMED and 0.1% wt/vol APS (13 kPa); and 8% wt/vol AA, 0.48% wt/vol BA, 1:1,000 vol/vol TEMED and 0.2% wt/vol APS (50 kPa). In all the compositions, AA% represents the sum of acrylamide and *N*-hydroxyethyl acrylamide, which is fixed at 0.1 M. Cells ( $4\times10^4$  cells cm $^{-2}$ ) were seeded in a drop of complete culture medium on top of fibronectin-coated hydrogels. After attachment, the hydrogel-containing wells were filled with the appropriate culture medium. Cells were collected for IF, RNA, protein extraction or luciferase assays after 24 h.

Micropatterned glass substrates were prepared by ultraviolet (UV) photolithography as previously described , with minor modifications. Briefly, a positive photoresist (S1805 G2, Microchem) was spin-coated on glass coverslips, previously silanized with 3-(trimethoxysilyl) propyl methacrylate (Sigma-Aldrich). The film was then patterned by UV exposure (collimated lamp at 365 nm) through a brightfield chrome photomask and developed with MF-319 (Microchem), achieving squares of photoresist. Linear polyacrylamide was then grafted on the patterned surface of the glass, polymerizing an 8% wt/vol solution of acrylamide in milliQ water with 0.0225% wt/vol of ammonium persulfate and 15:1,000 vol/vol of TEMED. The substrates were left overnight in water to wash out unreacted reagents. Finally, the resist

was stripped by dipping the substrates in dimethyl sulfoxide (DMSO) and milliQ water. The coverslips were UV-sterilized and the adhesive islands were functionalized by incubating a 10  $\mu g \ ml^{-1}$  fibronectin solution for 1 h at 37 °C. Micropatterned coverslips were washed twice in PBS, and 1 × 10 s cells (MCF10A, U2OS, HEK293) per micropattern were seeded in complete culture medium. Cells were gently washed twice with complete medium 2 h after seeding to remove unattached cells. Cells were fixed after 24 h for immunofluorescence.

The microfabricated fibronectin islands used in the experiments shown in Fig. 6b and Extended Data Fig. 9d were purchased from Cytoo SA. MCF10A  $(1 \times 10^6)$  cells were plated in a 35-mm dish containing a single Cytoo glass slide, and non-adherent cells were washed with medium after 2 h. After 24 h, the cells were processed for a proliferation assay, as indicated by the manufacturer (BrdU cell proliferation kit, Merck). Briefly, the cells were incubated for 1 h with a pulse of BrdU to label cells undergoing DNA duplication. The cells were fixed and processed for anti-BrdU immunofluorescence (\alpha BRDU). Pictures of BrdU stainings of 50 individual multicellular islands were turned into binary signals, superimposed to obtain the relative pixel frequency, and colour-coded using ImageJ (BrdU stack; Fiji). Pixel values indicate the percentage of cells in individual pictures displaying a BrdU-positive signal at that location. The same process was applied to pictures of nuclei (stained with Hoechst), ensuring a uniform distribution of cells within the monolayers. Proliferation rates in each sample were mapped with ImageJ by plotting BrdU pixel frequencies along the x axis of an imaging window set at the centre of the y axis. Confocal images were obtained with a Leica SP5 microscope and analysed using ImageJ.

#### **Immunofluorescence**

IF on paraformaldehyde (PFA)-fixed cells was performed as previously described  $^{62}$ . The primary antibodies were YAP (Santa Cruz Biotechnology, sc-101199) previously validated as YAP/TAZ antibody  $^{5,10,49,77}$ , laminA/C (Santa Cruz Biotechnology, sc-376248), paxillin (Abcam no. ab32084), GFP (Abcam ab13970), proteasome subunit alpha 5 (PSMA5; Origene, TA332887), AMOT (Santa Cruz Biotechnology, sc-166924), AMOTL1 (Sigma, HPA001196),  $\alpha$ -tubulin (Abcam, ab18251),  $\gamma$ -tubulin (Santa Cruz Biotechnology, sc-17787), acetylated-tubulin (ab24610), pericentrin 1 (Santa Cruz Biotechnology, sc-376111), laminC/C (Abcam, ab8984) and RNF146 (Thermo Fisher, H00081847-B01P). F-actin was stained with Alexa Fluor 568 phalloidin (Invitrogen). Secondary antibodies (1:200) were obtained from Invitrogen. Samples were counterstained with Hoechst to label cell nuclei. Slides were mounted using Prolong Diamond (Sigma).

For proteasomal staining (Fig. 3a,b), cells were treated with 10 µM lactacystin 6 h before collection. For MTs and centrosomal staining, cells were fixed as previously described<sup>78</sup> with minor modifications. The cells were fixed and permeabilized in a solution of 3% PFA, 0.2% glutaraldehyde and 0.25% Triton-X 100 in PBS 1× for 15 min at room temperature, then washed twice in PBS 1× for 10 min. Before staining, the cells were treated with a quenching solution (10 mM MES, 150 mM NaCl, 5 mM egtazic acid (EGTA), 5 mM MgCl<sub>2</sub> and 5 mM glucose, pH 6.1) freshly added with 1 mg ml<sup>-1</sup> sodium borohydride for 15 min on ice, then washed with PBS 1×. For a conformation-sensitive staining of the nuclear lamina (LmnA C-C staining), the cells were fixed in 2% PFA in PBS 1×. Unless otherwise specified, confocal images were obtained with a Leica Stellaris 5 microscope and analysed using LASX software and ImageJ. Super-resolution images of cytoskeletal staining (Figs. 1e,g,i,2e,f,i and 4j and Extended Data Fig. 3a,d) were obtained with the Leica Stellaris 5 LIGHTNING module. YAP/TAZ nuclear versus cytoplasmic ratios was quantified using ImageJ with the same threshold in each staining. yTURC numbers were quantified as the number of γ-tubulin positive dots in each cell using ImageJ. Proteasome puncta were quantified as the number of 20S positive spots in each cell using ImageJ. FAs were measured as the average length of the major axis of the paxillin-positive signal per cell using ImageJ. The apical-to-basal lamin

intensity ratios (Extended Data Fig. 3b,c) were determined as previously described<sup>23</sup> using ImageJ. 3D reconstructions of confocal images were obtained using *Z*-stacks with LASX software (Leica). The 3D reconstructions shown in Fig. 2a,b and Supplementary Video 2 were obtained with AIVIA (Leica) software, by training and applying a machine-learning pixel classifier algorithm to differentially segment phalloidin-stained F-actin fibres that directly contact the nuclear lamina (NASFs, shown in orange in Fig. 2a,b and Supplementary Video 2) and those that do not (shown in grey in Fig. 2a,b and Supplementary Video 2).

#### **Immunohistochemistry**

Immunohistochemical staining experiments were performed on PFA-fixed, paraffin wax-embedded tissue sections as previously described<sup>61</sup>. For immunohistochemistry the antibodies used were anti-YAP (CST #4912), anti-TAZ (Sigma-Aldrich HPA007415) and anti-AMOTL1 (Sigma-Aldrich HPA001196). Brightfield images were obtained with a Nanozoomer Scanner 2.0RS (Hamamatsu) equipped with NDPscan3.1 software. Immunohistochemical stainings were quantified with QuPath 5.0<sup>79</sup>, by adapting a StarDist<sup>80</sup> deep-learning-based cell segmentation algorithm. Relative AMOT protein abundance and YAP/TAZ nuclear-to-cytoplasmic ratios were normalized and expressed as *Z*-scores for comparative analysis.

#### Live imaging

For the live imaging experiments in Fig. 3f, RFP-AMOT-expressing MCF10A-YAP-eGFP-KI cells were seeded on  $\mu$ -dishes (Ibidi) previously coated with fibronectin 20  $\mu$ g ml $^{-1}$  (Santa Cruz Biotechnology) in 0.33  $\mu$ g ml $^{-1}$ doxycycline-containing medium 24 h before live imaging.

For live imaging experiments of Supplementary Video 3, RFP-AMOT-expressing HEK293 cells were seeded on  $\mu$ -dishes (Ibidi) previously coated with fibronectin 20  $\mu g$  ml  $^{-1}$  (Santa Cruz Biotechnology) in 0.33  $\mu g$  ml  $^{-1}$  doxycycline-containing medium 24 h before live imaging. The day after seeding, the cells were kept in complete medium supplemented with dynarrestin 10  $\mu M$  or with DMSO as negative control starting from 3 h before live imaging. For MT visualization, tubulin-555 (SpyroChrome) was diluted in culture medium according to the manufacturer's instructions 1 h before live imaging. All live imaging was acquired with a Leica Stellaris 5 confocal microscope equipped with an Okolab incubator chamber. 3D time-lapse videos were reconstructed using AIVIA software (Leica) by training and applying a machine-learning pixel classifier algorithm to differentially segment AMOT aggregates and microtubules.

#### In situ PLA

In situ PLAs were performed with Duolink in situ reagents (Sigma-Aldrich) on PFA-fixed samples, according to the manufacturer's instructions. The antibodies used were YAP1 (Proteintech, 13584-AP) and AMOT (Santa Cruz Biotechnology, sc-166924). Samples were counterstained with Hoechst to label cell nuclei. Slides were mounted using Prolong Diamond (Sigma). Images were acquired with a Leica Stellaris 5 confocal microscope and analysed using ImageJ.

#### hMSC adipogenic assay

Adipogenic differentiation was performed as previously described<sup>5</sup>, with minor modifications. For the experiments shown in Fig. 6a and Extended Data Fig. 9a,b, hMSCs were transfected with the indicated siRNAs and reseeded on micropatterns after 24 h. The cells were then cultured for five days in adipogenic induction medium (Lonza) followed by one day in adipogenic maintenance medium (Lonza) according to the manufacturer's instructions, until collection at day 6 of differentiation. Where indicated, cells were treated with Cyto.D 500 nM throughout the experiment. For the experiments shown in Extended Data Fig. 9c, hMSCs were transduced with pCW57.1-MCS (empty vector) or pCW57.1-HA-AMOTwt lentiviral constructs and then cultured for five days in adipogenic induction medium (Lonza) followed

by one day in adipogenic maintenance medium (Lonza), according to manufacturer's instructions, in the presence of doxycycline  $2 \mu g \, ml^{-1}$ , until collection at day 6 of differentiation. Adipogenic differentiation was assayed by Oil Red staining (Sigma) and quantified as the Oil Red-positive area normalized to the number of cells (Hoechst-positive nuclei) using ImageJ. Cells subjected to adipogenic differentiation protocol were collected after 24 h of culture in adipogenic induction medium to measure YAP/TAZ activity (Extended Data Fig. 5n).

#### qRT-PCR

Cells were collected using the RNeasy Mini Kit (Qiagen) for total RNA extraction, and contaminant DNA was removed by DNase treatment (Qiagen). qRT-PCR analyses were carried out on reverse-transcribed complementary DNAs (cDNAs) with QuantStudio 5 (Applied Biosystems, Thermo Fisher Scientific) and analysed with QuantStudio Design and Analysis software (version 1.4.3). Expression levels were always normalized to GAPDH. PCR oligonucleotide sequences are listed in Supplementary Table 6.

#### Western blots

Immunoblots were carried out as previously described<sup>61</sup>. The primary antibodies used are listed in Supplementary Table 7. Quantifications of relative protein levels from immunoblot bands were performed with ImageJ, relative to the corresponding GAPDH band from the same lane. Uncropped immunoblot images are provided as source data.

#### Co-immunoprecipitation of endogenous proteins

Pulldown of endogenous AMOT (Fig. 4c, f and Extended Data Fig. 6g), of endogenous DCTN1/p150-Glued (Figs. 4i and 5c and Extended Data Figs. 7n and 8d) and of endogenous YAP (Extended Data Fig. 7h) were performed on HEK293T cell lysates. For DCTN1/p150-Glued pulldown, cells were transiently transfected with 10 ng cm<sup>-2</sup> pCDNA3-HA-hAMOTwt or pCDNA3-HA-hAMOT-L178W for the experiments in Fig. 4i and Extended Data Fig. 7n, and with 0.2 ng cm<sup>-2</sup> pCDNA3-HA-hAMOTwt or pCDNA3-HA-hAMOT-S175A for the experiments in Fig. 5c and Extended Data Fig. 8d. Cells were re-plated at low confluency 24 h post DNA transfection. Cells were treated with dynarrestin 10 µM for 6 h before harvesting for the experiments shown in Fig. 5c and Extended Data Figs. 7n and 8d, and with the proteasome inhibitor lactacystin 10 µM for 6 h before collection for the experiments shown in Fig. 4c.f and Extended Data Fig. 6g. All samples were collected in Marais buffer (20 mM HEPES pH 7.8, 400 mM KCl, 5 mM EDTA, 0.4% NP40, 10% glycerol) freshly supplemented with 1 mM dithiothreitol (DTT), protease (Sigma) and phosphatase (Roche) inhibitors and kept on ice. The samples were sonicated and cleared by centrifugation for 10 min at full speed at +4 °C. Samples were diluted 1:7 vol/vol (for AMOT pulldown) or 1:3 vol/vol (for DCTN1/p150-Glued pulldown) in correction buffer (20 mM HEPES pH 7.8, 3.1 mM MgCl<sub>2</sub>, 3.5% glycerol) freshly supplemented with protease and phosphatase inhibitors. For YAP pulldown, samples were collected in YAP lysis buffer (20 mM HEPES pH 7.6, 50 mM KCl, 0.1% NP40, 0.1% Triton-X100, 5% glycerol, 5 mM MgCl<sub>2</sub>, 1 mM DTT, 1 mM ATP, 1 mM creatin-phosphate) freshly supplemented with protease and phosphatase inhibitors. Samples were mechanically disrupted by repeated passages through a 26-G needle and cleared by centrifugation for 10 min at full speed at room temperature. To the samples were then added 100 mM NaCl, 1.5 mM MgCl<sub>2</sub>, 0.2 mM EDTA and 15% glycerol. Protein-G or protein-A coated magnetic Dynabeads (Thermo Fisher) were coated with 2 µg of anti-AMOT (Santa Cruz Biotechnology), anti-DCTN1/p150-Glued (Abcam) or anti YAP1 (Proteintech) antibody per sample, and the cell lysates were incubated with coated magnetic beads for 3 h at 4 °C (AMOT and DCTN1 pulldowns) or for 3 h at room temperature (YAP pulldown) under gentle rotation. Beads coated with normal mouse immunoglobulin G (IgG; Santa Cruz Biotechnologies) or with normal rabbit IgG (Sigma) were used as a negative control for AMOT or DCTN1/p150-Glued and YAP pulldown, respectively.

#### Co-immunoprecipitation of overexpressed proteins

Pulldown of FLAG-DCTN1wt and FLAG-DCTN1-ICD-4Wmut, shown in Fig. 4h and Extended Data Fig. 7m, pulldown of HA-hAMOT-S175E and HA-hAMOT-S175A, shown in Fig. 5b and Extended Data Fig. 8c, were performed on HEK293T cell lysates. For FLAG-DCTN1 pulldown, the cells were transiently transfected with 60 ng cm<sup>-2</sup> pCDNA3-HA-hAMOTwt and 100 ng cm<sup>-2</sup> pCDNA3-FLAG-DCTN1wt or pCDNA3-FLAG-DCTN1-ICD-4Wmut. For HA-AMOT pulldown, cells were transiently transfected with 25 ng cm<sup>-2</sup> pCDNA3-HA-hAMOT-S175A or 12.5 ng cm<sup>-2</sup> pCDNA3-HA-hAMOT-S175E. The cells were re-plated at low confluency 24 h post DNA transfection. The next day, cells were treated with dynarrestin 10 µM (for FLAG-DCTN1 pulldown) or with lactacystin 10 µM (for HA-AMOT pulldown) for 6 h before collection. All cells were collected in Marais buffer (20 mM HEPES pH 7.8, 400 mM KCl, 5 mM EDTA, 0.4% NP40, 10% glycerol) freshly supplemented with 1 mM DTT, protease and phosphatase inhibitors and kept on ice. The samples were sonicated and cleared by centrifugation for 10 min at full speed at +4 °C, then the samples were diluted 1:3 vol/vol (for FLAG-DCTN1 pulldown) or 1:7 vol/vol (for HA-AMOT pulldown) with correction buffer (20 mM HEPES pH 7.8, 3.1 mM MgCl<sub>2</sub>, 3.5% glycerol), freshly supplemented with protease and phosphatase inhibitors.

Protein-G- or protein-A-coated magnetic Dynabeads (Thermo Fisher) were coated with 2  $\mu g$  anti-FLAG M2 (Sigma) or anti-HA (Abcam) antibody per sample, and the cell lysates were incubated with coated magnetic beads for 3 h at 4 °C under gentle rotation. Beads coated with normal mouse lgG (Santa Cruz Biotechnologies) or with normal rabbit lgG (Sigma) were used as a negative control for FLAG or HA pulldown, respectively.

#### **PARylation** assays

The immunoprecipitation of FLAGmAMOTL1 shown in Extended Data Fig. 6e was performed on HEK293T cell lysates. Cells were transiently transfected with 1.5 ng cm<sup>-2</sup> pCMV6-FLAG-mAMOTL1. Twenty-four hours post DNA transfection, the cells were re-plated in sparse  $(5 \times 10^4 \text{ cells cm}^{-2})$  versus dense  $(2.5 \times 10^5 \text{ cells cm}^{-2})$  conditions with the proteasome inhibitors MG115 and MG132 (10 μM). After 24 h, the cells were lysed in PAR buffer (50 mM Tris-HCl pH 7.4, 150 mM NaCl, 25 mM sodium pyrophosphate, 1% NP40, 5% glycerol), freshly supplemented with 1 µM ADP-HPD (Millipore), 1 mM DTT, protease and phosphatase inhibitors, and kept on ice. The samples were sonicated and cleared by centrifugation for 10 min at full speed at +4 °C. Protein-G-coated magnetic Dynabeads (Thermo Fisher) were coated with 2 µg anti-FLAG M2 antibody (Sigma) per sample in PAR buffer for 1 hat room temperature and then used for FLAG-mAMOTL1 pulldown. Cell lysates were incubated with coated magnetic beads for 4 h at 4 °C under gentle rotation.

#### **Ubiquitylation assays**

The immunoprecipitation of FLAGmAMOTL1 shown in Extended Data Fig. 6f was performed on HEK293T cell lysates. Cells were transiently transfected with siRNAs and after 24 h with 1.5 ng cm<sup>-2</sup> pCMV6-FLAG-mAMOTL1 and with 60 ng cm<sup>-2</sup> pRK5-HA-ubiquitin-WT. The cells were re-plated 8 h post DNA transfection in sparse  $(5 \times 10^4 \text{ cells cm}^{-2})$  or dense  $(2.5 \times 10^5 \text{ cells cm}^{-2})$  conditions. After 15 h, cells were treated with lactacystin (10 µM) for 6 h and then lysed in Ub-buffer (50 mM HEPES pH 7.8, 200 mM NaCl, 5 mM EDTA, 1% NP40, 5% glycerol), freshly supplemented with 250 ng ml<sup>-1</sup>ubiquitin aldehyde (Millipore, 662056), 1 mM DTT, protease and phosphatase inhibitors, and kept on ice. Samples were sonicated and cleared by centrifugation for 10 min at full speed at +4 °C. Protein-G-coated magnetic Dynabeads (Thermo Fisher) were coated with 2 µg anti-FLAG M2 antibody (Sigma) per sample in Ub-buffer for 1 h at room temperature and then used for FLAG-mAMOTL1 pulldown. The cell lysates were incubated with coated magnetic beads for 4 h at 4 °C under gentle rotation in Ub-buffer supplemented with 2 mM MgCl $_2$ . Stringent washes were then performed using Ub-wash buffer (50 mM HEPES pH 7.8, 500 mM NaCl, 5 mM EDTA, 1% NP40, 5% glycerol), freshly complemented with 250 ng ml $^{-1}$  ubiquitin aldehyde, 1 mM DTT, protease and phosphatase inhibitors.

#### Filamentous actin quantitation assays

To determine the amount of filamentous actin (F-actin) versus free globular-actin (G-actin) content in mechano-ON versus mechano-OFF cells (Extended Data Fig. 5i), MCF10A cells were seeded on stiff (40 kPa) versus soft (0.7 kPa) hydrogels (2  $\times$  10 $^6$  total cells for each condition). After 24 h, cells were collected and processed for quantitation of F-actin and G-actin cellular fractions by western blot, using the G-Actin/F-actin In Vivo Assay Biochem Kit (Cytoskeleton, #BK037), according to the manufacturer's instructions.

#### Luciferase reporter assays

Luciferase assays were performed as previously described<sup>49</sup>, with minor modifications. Briefly, the TEAD luciferase reporter 8xGTIlC-Lux (75 ng cm<sup>-2</sup>) was transfected together with phRG-TK-Renilla (25 ng cm<sup>-2</sup>) to normalize for transfection efficiency. Cells plated at low confluency were transfected with DNA or with both siRNAs and DNA, and re-plated in Mech.ON versus Mech.OFF conditions, as indicated. For the experiments shown in Fig. 5e and Extended Data Fig. 5o, cells were re-plated at low confluency in Cyto.D (200 nM) containing medium. Cells were collected 24 h post re-plating. Firefly luciferase activity was measured with an Infinite F200PRO plate reader (Tecan). Data are presented as firefly/*Renilla* luciferase activity.

#### **Mammosphere** assays

MII control and AMOT tKO cells were seeded ( $2 \times 10^3$  cells cm<sup>-2</sup>) as a single-cell suspension in ultralow-attachment plates (Corning). The cells were cultured in DMEM/F12 supplemented with 0.4% bovine serum albumin (BSA), antibiotics,  $5~\mu g$  ml<sup>-1</sup>insulin (Sigma-Aldrich), 10~ng ml<sup>-1</sup> hEGF (Peprotech), 20~ng ml<sup>-1</sup>bFGF (Peprotech) and  $4~\mu g$  ml<sup>-1</sup>heparin. Where indicated, siRNA transfection was performed the day before mammosphere seeding. For the experiments in Extended Data Fig. 9g, the cells were treated with DMSO or VT107 ( $6~\mu M$ ) 48 h before mammosphere seeding, and the treatments were refreshed ( $3~\mu M$ ) every 48 h. Mammospheres were counted after 15 days.

#### Agar colony formation assays

MII cells were transfected with the indicated siRNAs and embedded in agar after 24 h. Effective YAP/TAZ downregulation was assessed by immunoblotting on the same cell population. Where indicated, MII cells were treated with DMSO or the TEAD inhibitor VT107 (6  $\mu$ M) 48 h before agar embedding. For the experiments in Extended Data Fig. 9h, MDA-MB-231 cells were treated with doxycycline (2 μg ml<sup>-1</sup>) 24 h before agar embedding. Clonogenic assays were performed as previously described<sup>77</sup>. Briefly, cells  $(1 \times 10^4)$  were resuspended in complete growth medium with 0.3% agarose (BD Biosciences) and were layered onto 0.6% agar beds in six-well plates. Complete medium was added on top of the cells and was replaced with fresh medium twice a week for four weeks. For the experiments in Extended Data Fig. 9g, DMSO or the TEAD inhibitor VT107 (3  $\mu$ M) were added to fresh medium. For the experiments in Extended Data Fig. 9h, MDA-MB-231 cells were maintained in complete medium supplemented with doxycycline (2 μg ml<sup>-1</sup>).

#### **Lentiviral preparations**

Lentiviral particles were prepared as previously described <sup>61</sup>. Briefly, HEK293T cells were transiently transfected with lentiviral vectors (167 ng cm<sup>-2</sup>) together with the packaging vectors pMD2-VSVG (42 ng cm<sup>-2</sup>) and pPAX2 (125 ng cm<sup>-2</sup>) using TransIT-LT1 (Mirus Bio) according to the manufacturer's instructions.

#### **Statistics**

The number of biological and technical replicates and the number of animals are indicated in the figure legends, main text and Methods. All tested animals were included. Animal ages and sexes are specified in the text and Methods. Sample size was not predetermined. Randomization was not applicable to our experiments with cell lines. Student's *t*-test and ANOVA analyses were performed, as indicated in the figure captions and Supplementary figures, using GraphPad Prism 8.0.2 for Mac software. Data collection and analysis were not performed blind, as the analyses relied on unbiased measurements of quantitative parameters. However, standardized procedures for data collection and analysis were used to prevent bias. No data points or animals were excluded from the analyses.

#### **Reporting Summary**

Further information on research design is available in the Nature Portfolio Reporting Summary linked to this Article.

#### Data availability

Data supporting the findings of this study are available from the corresponding author on reasonable request. The previously published crystal structure of 14-3-3 in complex with Amot-p130 peptide<sup>43</sup> is available from RCSB Protein Data Bank under PDB code 7nma. The BioGRID<sup>31</sup> human database is available at https://downloads.thebiogrid.org/BioGRID/Release-Archive/BIOGRID-3.5.169/. Previously published<sup>38</sup> mass spectrometry datasets of human proximal proteins are available from the ProteomeXchange through its partner Mass spectrometry Interactive Virtual Environment MassIVE (http://proteomics.ucsd.edu/ProteoSAFe/datasets.jsp; PXD015530, PXD015531). Source data are provided with this paper.

#### References

- Franklin, J. M., Ghosh, R. P., Shi, Q., Reddick, M. P. & Liphardt, J. T. Concerted localization-resets precede YAP-dependent transcription. *Nat. Commun.* 11, 4581 (2020).
- Santner, S. J. et al. Malignant MCF10CA1 cell lines derived from premalignant human breast epithelial MCF10AT cells. *Breast Cancer Res. Treat.* 65, 101–110 (2001).
- Meng, Z. et al. RAP2 mediates mechanoresponses of the Hippo pathway. Nature 560, 655–660 (2018).
- Gandin, A. et al. Broadly applicable hydrogel fabrication procedures guided by YAP/TAZ-activity reveal stiffness, adhesiveness and nuclear projected area as checkpoints for mechanosensing. Adv. Healthc. Mater. 11, e2102276 (2022).
- Chang, L. et al. The SWI/SNF complex is a mechanoregulated inhibitor of YAP and TAZ. Nature 563, 265–269 (2018).
- Zanconato, F. et al. Transcriptional addiction in cancer cells is mediated by YAP/TAZ through BRD4. Nat. Med. 24, 1599–1610 (2018).
- Zilberman, Y. et al. Regulation of microtubule dynamics by inhibition of the tubulin deacetylase HDAC6. J. Cell Sci. 122, 3531–3541 (2009).
- 79. Bankhead, P. et al. QuPath: Open source software for digital pathology image analysis. *Sci. Rep.* **7**, 16878 (2017).
- Schmidt, U., Weigert, M., Broaddus, C. & Myers, G. Cell detection with star-convex polygons. Lect. Notes Comput. Sci. 11071, 265–273 (2018).

 Elfmann, C. & Stulke, J. PAE viewer: a webserver for the interactive visualization of the predicted aligned error for multimer structure predictions and crosslinks. *Nucleic Acids Res.* 51, W404–W410 (2023).

#### **Acknowledgements**

We thank colleagues for sharing their plasmids on Addgene, M. Vittoria Dieci, V. Guarneri, M. Fassan and V. Guzzardo for human TNBC samples in the context of the METAMECH Consortium, and all members of our group for critical reading of the manuscript. This research has received funding from the following agencies/ charities: FONDAZIONE AIRC under the 5 per Mille 2019-ID. 22759 programme, and under the IG 2019-ID. 23307 project to S.P.; the European Research Council Executive Agency (ERCEA) under ERC-2022-ADG grant agreement no. 101098074-CHARTAGING to S.P.; FONDAZIONE AIRC under the IG 2022-ID. 27883 project to M.C.; the European Union-Next Generation EU and STARS@UNIPD, GF-MET-Growth factor signalling in metastatic organotropism to F.Z.; the European Union-Next Generation EU, Mission 4, Component 2, CUP C93C22002780006, Spoke n.2 ('Cancer') to F.Z., T.P. and S.P.; and Spoke n.5 ('Inflammatory diseases') to M.C. and G.B.

#### **Author contributions**

G.V. performed most of the experiments in vitro and in vivo, trained and received help from C.A.Jr, and contributed to the writing of the paper. A.C. and G.M. helped with the CRISPR KO clones and mice experiments. A.G. and G.B. supported the mechanical bioassays. M.C. helped with data mining. M.D.P., E.P., L.S.P., A.S. and R.A.S. helped with protein structural studies. R.C. helped with 3D image reconstructions. T.P. developed the methodology for digital pathology quantitative analyses. F.Z. and P.C. contributed with ideas and troubleshooting. S.P. and T.P. conceived the initial hypothesis and experimental design, organized the work and wrote the paper.

#### **Competing interests**

The authors declare no competing interests.

#### **Additional information**

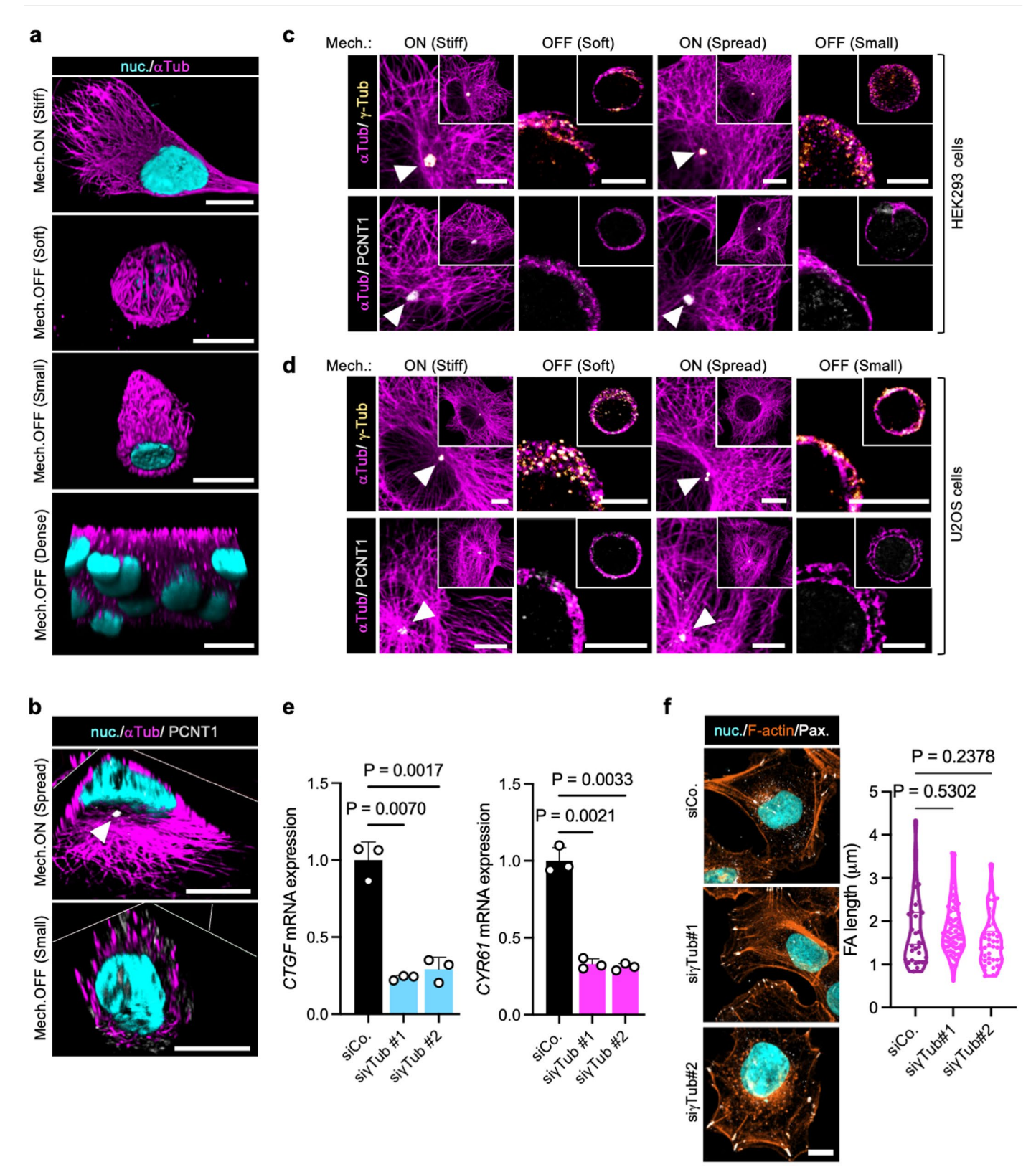
**Extended data** is available for this paper at https://doi.org/10.1038/s41556-025-01773-z.

**Supplementary information** The online version contains supplementary material available at https://doi.org/10.1038/s41556-025-01773-z.

**Correspondence and requests for materials** should be addressed to Tito Panciera or Stefano Piccolo.

**Peer review information** *Nature Cell Biology* thanks Georg Halder and the other, anonymous, reviewer(s) for their contribution to the peer review of this work.

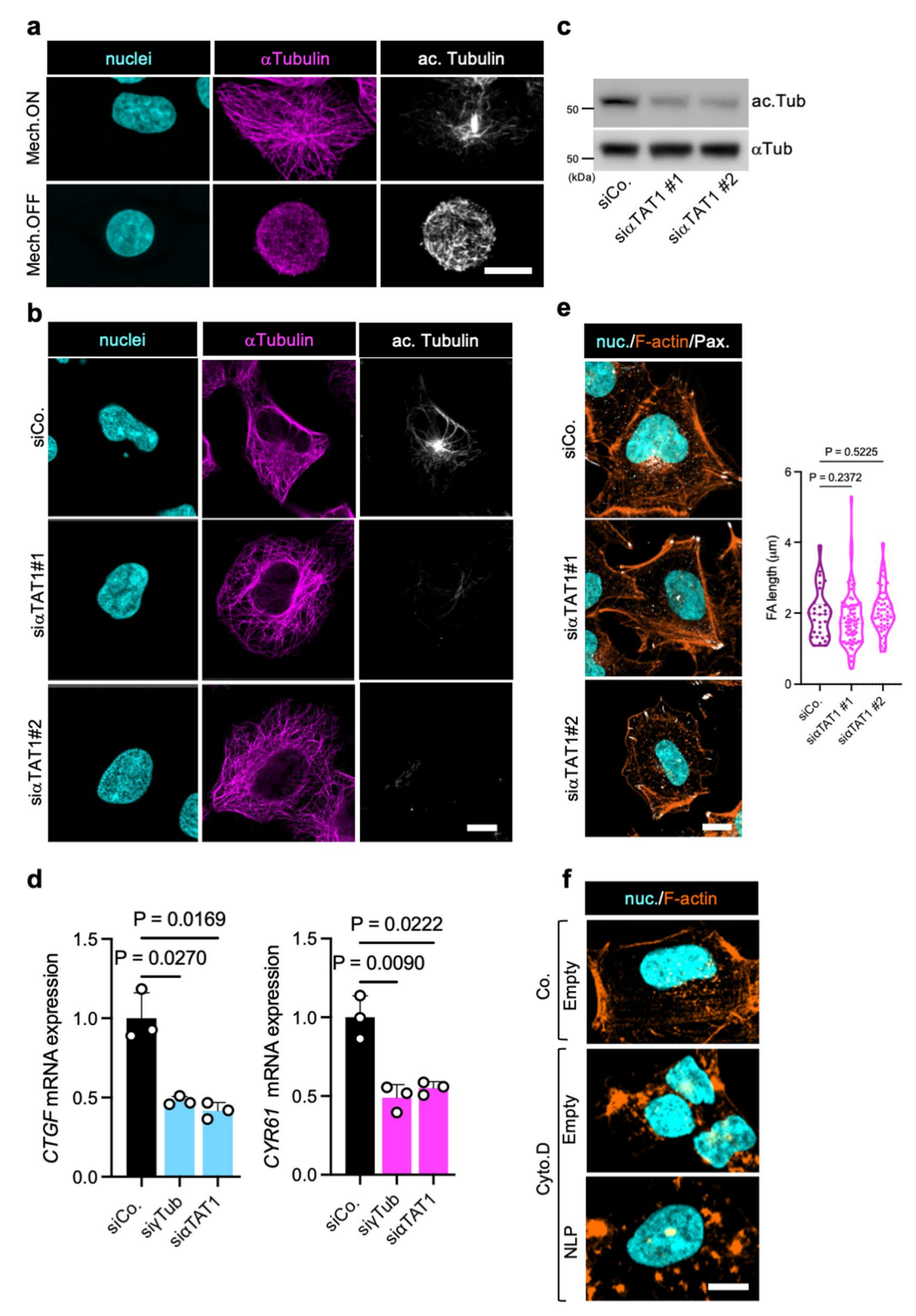
**Reprints and permissions information** is available at www.nature.com/reprints.



Extended Data Fig. 1 | See next page for caption.

Extended Data Fig. 1 | Microtubules (MTs) centrosomal organization serves as determinant of YAP/TAZ mechanotransduction. a) Representative 3D immunofluorescence reconstructions of MCF10A cells seeded the indicated Mech.ON versus Mech.OFF conditions. MTs were labelled by α-Tubulin staining (αTub, magenta) and nuclei were counterstained with Hoechst (cyan). Scalebar, 10 μm. See also Supplementary Video 1 for an all-around view of the same cells. **b**) Representative immunofluorescence images (3D sections) of MCF10A cells seeded on Spread (unconfined, Mech.ON) versus Small (100 µm<sup>2</sup> micropatterns, Mech.OFF) substrates. MTs were labelled by  $\alpha$ -Tubulin staining ( $\alpha$ Tub, magenta), the centrosome was labelled by pericentrin (PCNT1, grey) and highlighted by white arrowhead. Nuclei were counterstained with Hoechst (cyan). Scale bar, 10 μm. **c**, **d**) Representative immunofluorescence images of HEK293 cells (**c**) and U2OS cells (d) seeded in the indicated mechanical conditions. Images are magnifications of the insets shown in the upper right corner of each picture. MTs were labelled by α-Tubulin staining (αTub, magenta), γ-TURCs were labelled by γ-Tubulin staining (γTub, yellow), the centrosome was labelled by pericentrin

(PCNT1, grey). γ-TURCs and centrosomes are highlighted by white arrowheads. Scale bar, 5 µm. The same experiment was repeated twice with comparable results. e) Quantitative real-time PCR (qRT-PCR) assessing the expression levels of the YAP/TAZ endogenous targets CTGF (left) and Cyr61 (right) in HEK293 cells  $treated \, with \, the \, indicated \, siRNAs \, and \, seeded \, in \, mechano-ON \, conditions. \, Data$ are mean + s.d. of n = 3 biologically independent samples. Left graph: P = 0.007(siCo. vs si $\gamma$ Tub#1), P = 0.0017 (siCo. vs si $\gamma$ Tub#2); right graph: P = 0.0021(siCo. vs siyTub#1), P = 0.0033 (siCo. vs siyTub#2). f) Left: representative immunofluorescence images of HEK293 cells treated with the indicated siRNAs. F-actin was labelled by Phalloidin staining (F-actin, orange), focal adhesions were labelled by Paxillin staining (Pax, grey) and nuclei were counterstained with Hoechst (cyan). Scale bar, 10  $\mu$ m. Right: quantifications (n = 30 cells for siCo., n = 71 cells for siyTub#1, n = 40 cells each for siyTub#2, pooled from two independent seedings) of focal adhesion length in cells treated as in left panels. P = 0.5302 (siCo. vs siyTub#1), P = 0.2378 (siCo. vs siyTub#2). P values were determined by one-way ANOVA with Welch's correction (e, f).

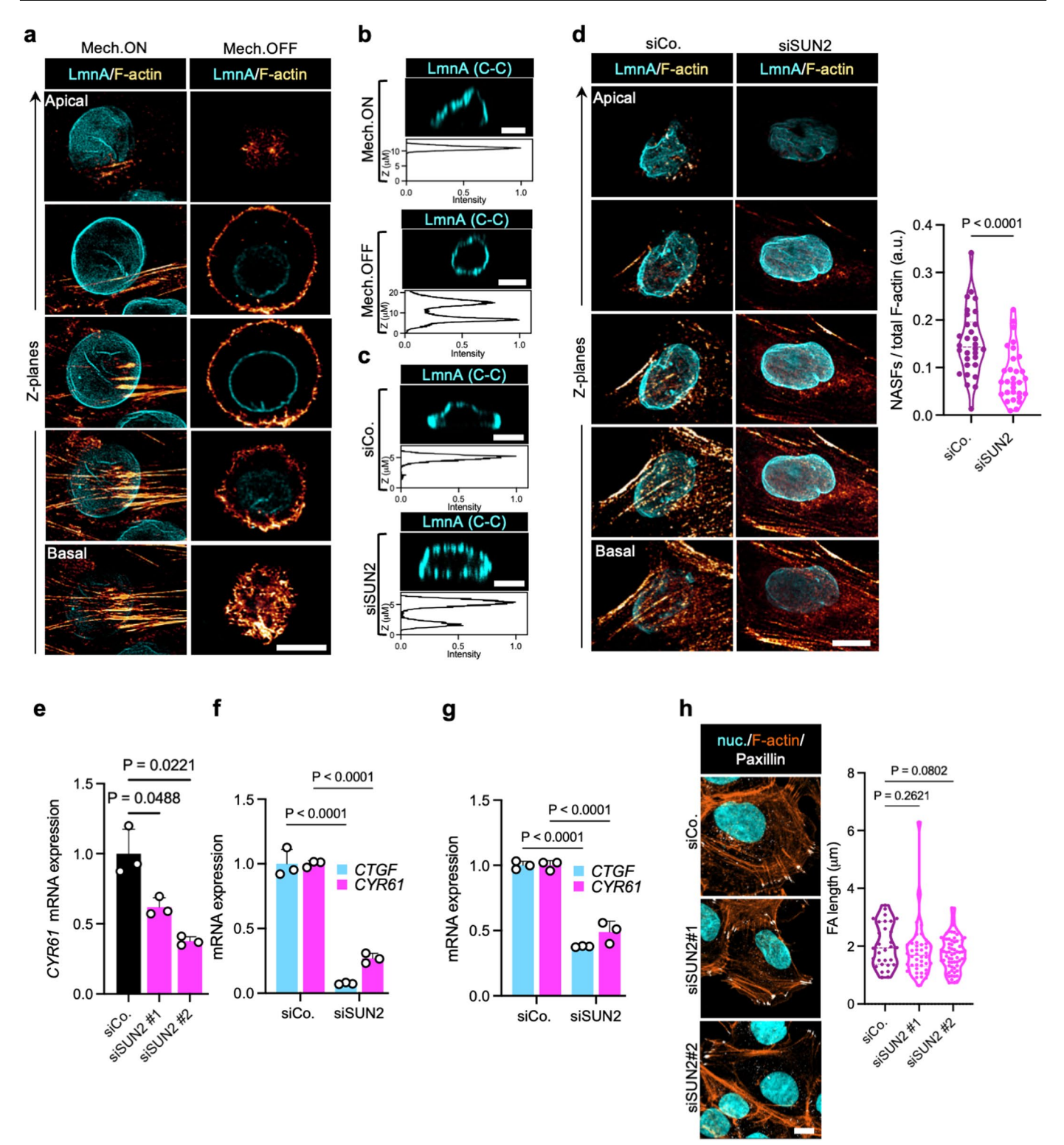


Extended Data Fig. 2 | See next page for caption.

## $\label{prop:prop:continuous} Extended \ Data \ Fig.\ 2\ |\ Microtubules\ acetylation\ is\ required\ for\ centrosomal\ radial\ MT\ sprouting\ and\ for\ YAP/TAZ\ activation\ in\ mechano-ON\ cells.$

a) Representative immunofluorescence images of MTs (αTub) and acetylated Tubulin (ac. Tubulin) in HEK293 cells seeded in the indicated mechanical conditions. Nuclei were counterstained with Hoechst (cyan). Scale bar, 10 μm.
b) Representative immunofluorescence images of MTs (αTub) and acetylated Tubulin (ac. Tubulin) in HEK293 cells seeded in Mech.ON conditions and treated with the indicated siRNAs. Nuclei were counterstained with Hoechst (cyan). Scale bar, 5 μm. c) Representative immunoblots of acetylated Tubulin (ac. Tub) in HEK293 cells seeded in mechano-ON conditions and treated with the indicated siRNAs. αTubulin (αTub) serves as loading control. d) Quantitative real-time PCR (qRT–PCR) assessing the expression levels of the YAP/TAZ endogenous targets *CTGF* (left) and *Cyr61* (right) in U2OS cells treated with the indicated siRNAs and seeded in mechano-ON conditions. Data are mean + s.d. of n = 3 biologically

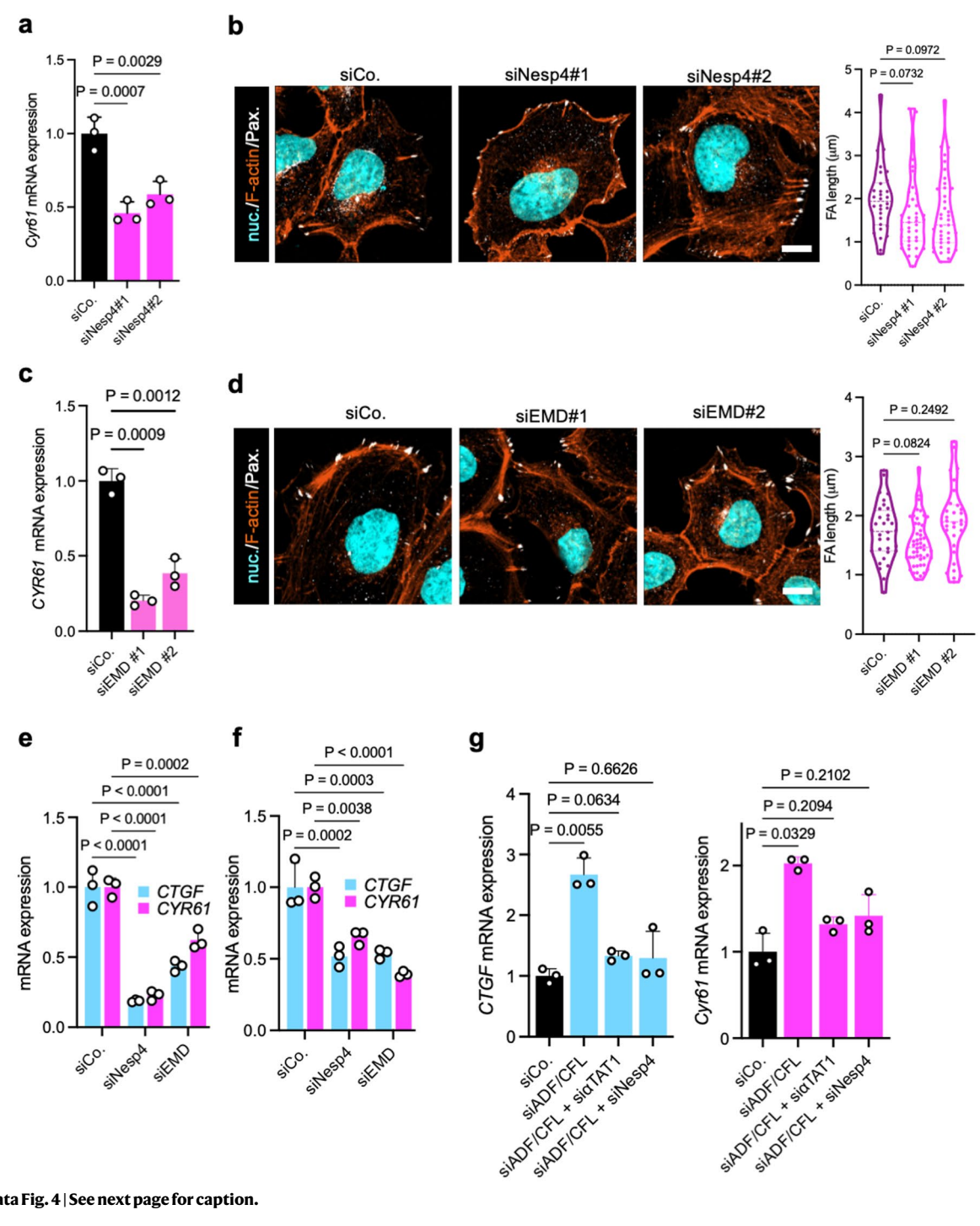
independent samples. Left graph: P = 0.0270 (siCo. vs siyTub), P = 0.0169 (siCo. vs si $\alpha$ TAT1); right graph: P = 0.009 (siCo. vs siyTub), P = 0.0222 (siCo. vs si i $\alpha$ TAT1). e) Left: representative immunofluorescence images of HEK293 cells treated with the indicated siRNAs. F-actin was labelled by Phalloidin staining (F-actin, orange), focal adhesions were labelled by Paxillin staining (Pax, grey) and nuclei were counterstained with Hoechst (cyan). Scale bar, 10  $\mu$ m. Right: quantifications (n = 30 cells for siCo., n = 77 cells for si $\alpha$ TAT1#1, n = 50 cells each for si $\alpha$ TAT1#2, pooled from two independent seedings) of focal adhesion length in cells treated as in left panels. P = 0.2372 (siCo. vs si $\alpha$ TAT1#1), P = 0.5225 (siCo. vs si $\alpha$ TAT1#2). f) Representative immunofluorescence of F-actin (orange, Phalloidin labelling) in HEK293 cells transduced with empty or NLP1-encoding lentiviruses and treated with Cytochalasin D (Cyto.D,  $1 \mu$ M for 2 h) or DMSO as negative control, as in Fig. 1i, j. Nuclei were counterstained with Hoechst (cyan). Scale bar,  $5 \mu$ m. P values were determined by one-way ANOVA with Welch's correction (d, e).



Extended Data Fig. 3 | See next page for caption.

Extended Data Fig. 3 | Loss of NE-NASFs tethering impairs YAP/TAZ mechanoactivation. a) Representative Z-planes of immunofluorescence stacks of MCF10A cells seeded in mechano-ON (40 kPa) versus -OFF (0,7 kPa) conditions, showing NASFs contacting the basal side of the nuclear envelope of mechano-activated, but not of mechano-inhibited cells. The nuclear lamina was labelled by LaminA staining (cyan) and F-actin was labelled by Phalloidin staining (orange). Basal to apical planes are shown in bottom to top panels. Scale bar, 10 µm. See also Fig. 2a for 3D reconstructions of cells seeded in the same conditions. **b**) Representative (n = 3 independent replicates) immunofluorescence YZ-sections of MCF10A cells seeded on stiff (Mech.ON) versus soft (Mech.OFF) hydrogels. Lamin was labelled by a conformation-sensitive LmnA antibody (LmnA C-C, cyan), which is unable to bind the basal side of the NE of mechano-ON cells due to LaminA stretching. The corresponding intensity profiles of LmnA conformation-sensitive staining along the Z-axis is shown below each immunofluorescence picture. Scale bar, 10 µm. c) Representative (n = 3 independent replicates) immunofluorescence YZsections of MCF10A cells treated with the indicated siRNAs. A conformationsensitive LmnA antibody (LmnA C-C, cyan), which is unable to bind stretched LaminA was used to show loss of basal nuclear tension in SUN2-depleted cells. The corresponding intensity profiles of LmnA conformation-sensitive staining along the Z-axis is shown below each immunofluorescence picture. Scale bar, 10 μm. d) Left: Representative Z-planes of immunofluorescence stacks of MCF10A cells treated with indicated siRNAs, showing abolished NASFs formation in SUN2-depleted cells. The nuclear lamina was labelled by LaminA staining (cyan) and F-actin was labelled by Phalloidin staining (orange). Basal to apical

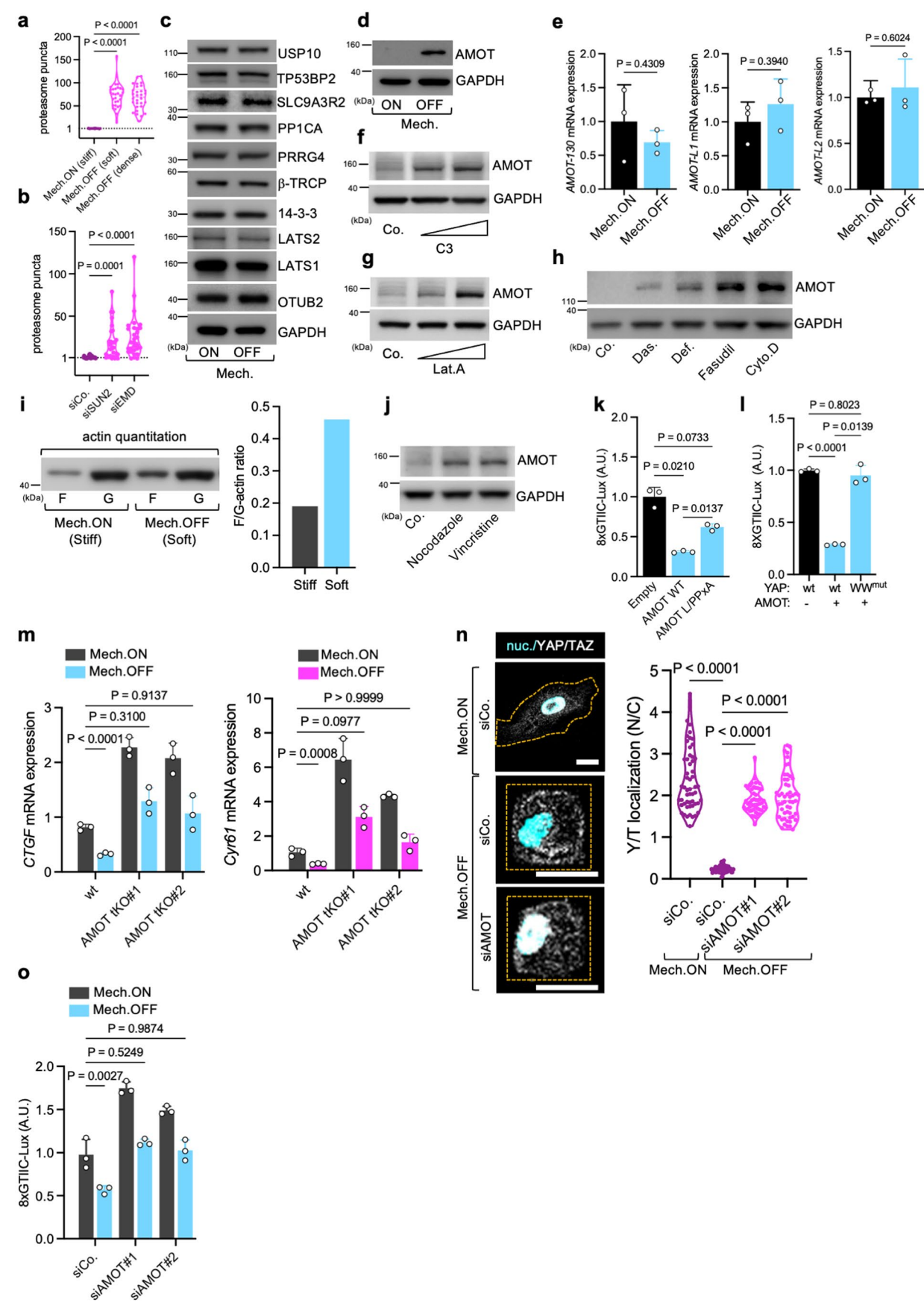
planes are shown in bottom to top panels. Scale bar, 10 µm. See also Fig. 2b for 3D sections of cells treated as in (d). Right: quantifications of NASFs/total F-actin ratios in the same cells (n = 30 for each condition, pooled from two independent seedings). P < 0.0001. e) Quantitative real-time PCR (qRT-PCR) assessing the expression levels of the YAP/TAZ endogenous target Cyr61 in HEK293 cells treated with the indicated siRNAs and seeded in mechano-ON conditions. Data are mean + s.d. of n = 3 biologically independent samples. P = 0.0488 (siCo. vs siSUN2#1), P = 0.0221 (siCo. vs si siSUN2#2). **f**, **g**) Quantitative real-time PCR (qRT-PCR) assessing the expression levels of the YAP/TAZ endogenous targets CTGF and Cyr61 in MCF10A (f) and U2OS (g) cells treated with the indicated siRNAs and seeded in mechano-ON conditions. Data are mean + s.d. of n = 3 biologically  $independent \, samples. \textit{P} < 0.0001.\, \textbf{h}) \, Loss \, of \, NE-MTs \, tethering \, impairs \, YAP/TAZ$ mechano-activation, independently of F-actin and focal adhesions architecture. Left: representative immunofluorescence images of HEK293 cells treated with the indicated siRNAs. F-actin was labelled by Phalloidin staining (F-actin, orange), focal adhesions were labelled by Paxillin staining (Pax, grey) and nuclei were counterstained with Hoechst (cyan). Scale bar, 10 μm. Right: quantifications (n = 30 cells for siCo., n = 42 cells for siSUN2#1, n = 65 cells each for siSUN2#2, pooled from two independent seedings) of focal adhesion length in cells treated as in left panels. P = 0.2621 (siCo. vs siSUN2#1), P = 0.0802 (siCo. vs si siSUN2#2). P values were determined by unpaired two-tailed Student's t-test with Welch's correction (d) one-way ANOVA with Welch's correction (e, h), or with two-way ANOVA (f.g).



Extended Data Fig. 4 | See next page for caption.

Extended Data Fig. 4 | Loss of Nesprin or Emerin impairs YAP/TAZ mechanoactivation. a) Quantitative real-time PCR (qRT-PCR) assessing the expression levels of the YAP/TAZ endogenous target Cyr61 in HEK293 cells treated with the indicated siRNAs and seeded in mechano-ON conditions. Data are mean + s.d. of n = 3 biologically independent samples. P = 0.0007 (siCo. vs siNesp4#1), P = 0.0029 (siCo. vs siNesp4#2). **b**) Left: representative immunofluorescence images of HEK293 cells treated with the indicated siRNAs. F-actin was labelled by Phalloidin staining (F-actin, orange), focal adhesions were labelled by Paxillin staining (Pax, grey) and nuclei were counterstained with Hoechst (cyan). Scale bar, 10 µm. Right: quantifications (n = 30 cells for siCo., n = 39 cells each for all other conditions, pooled from two independent seedings) of focal adhesion length in cells treated as in left panels. P = 0.0732 (siCo. vs siNesp4#1), P = 0.0972(siCo. vs siNesp4#2).c) Quantitative real-time PCR (qRT-PCR) assessing the expression levels of the YAP/TAZ endogenous target Cyr61 in HEK293 cells treated with the indicated siRNAs and seeded in mechano-ON conditions. Data are mean + s.d. of n = 3 biologically independent samples. P = 0.0009 (siCo. vs siEMD#1), P = 0.0012 (siCo. vs siEMD#2). **d**) Loss of NE-MTs tethering impairs YAP/TAZ mechano-activation, independently of F-actin and focal adhesions architecture. Left: representative immunofluorescence images of HEK293 cells treated with the indicated siRNAs. F-actin was labelled by Phalloidin staining (F-actin, orange), focal adhesions were labelled by Paxillin staining (Pax, grey)

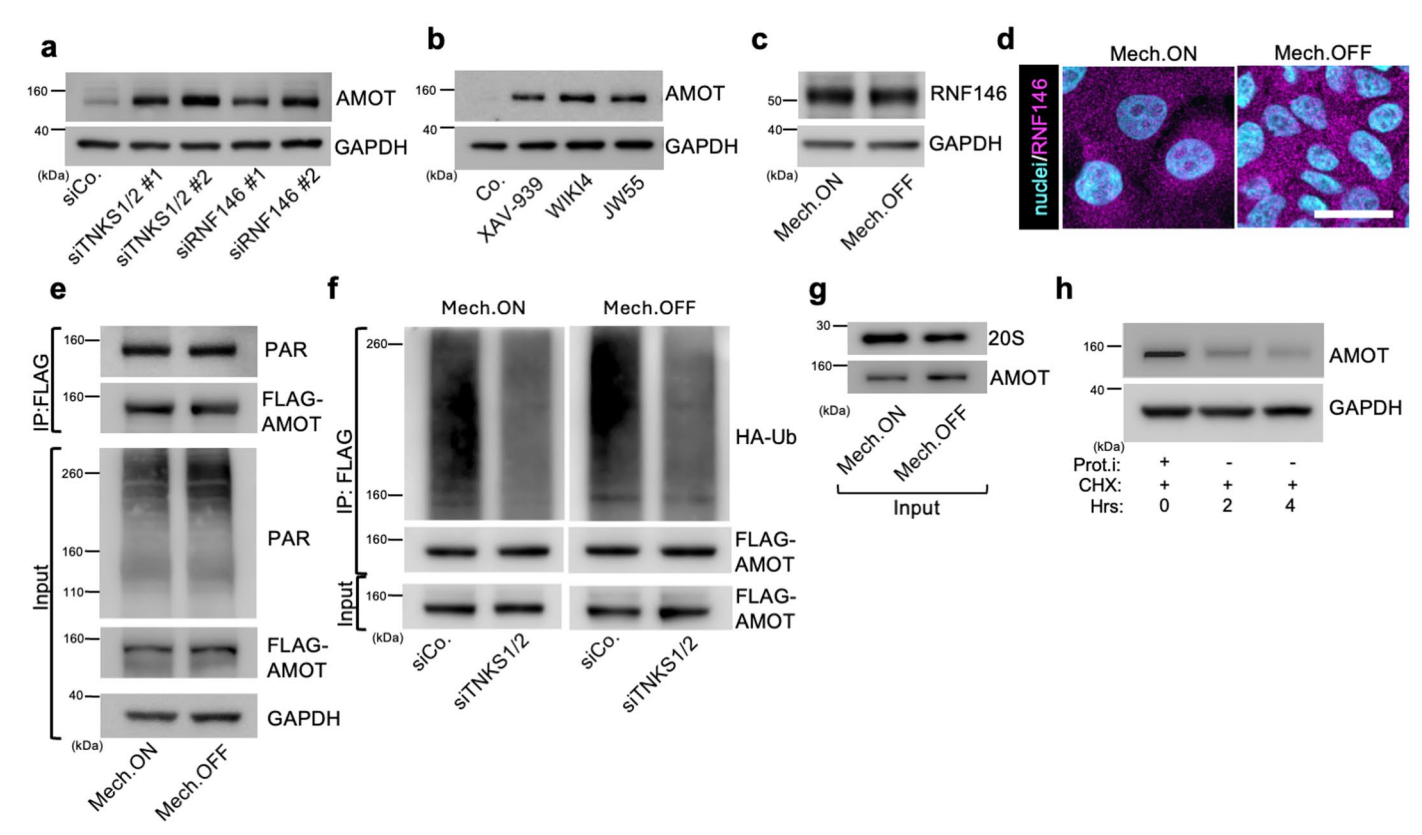
and nuclei were counterstained with Hoechst (cyan). Scale bar, 10 µm. Right: quantifications (n = 32 cells for siCo., n = 51 cells for siEMD#1, n = 30 cells each for si EMD#2, pooled from two independent seedings) of focal adhesion length incells treated as in left panels. P = 0.0824 (siCo. vs siEMD#1), P = 0.2492 (siCo. vs siEMD#2). e, f) Quantitative real-time PCR (qRT-PCR) assessing the expression levels of the YAP/TAZ endogenous targets CTGF and Cyr61 in MCF10A (e) and U2OS (f) cells treated with the indicated siRNAs and seeded in mechano-ON conditions. Data are mean + s.d. of n = 3 biologically independent samples. In (e): P = 0.0002 (Cyr61 siCo. vs siEMD), P < 0.0001 for all other comparisons shown; in (f): P = 0.0002 (CTGF siCo. vs siNesp4), P = 0.0003 (CTGF siCo. vs siEMD); P = 0.0038 (Cyr61 siCo. vs siNesp4); P < 0.0001 (Cyr61 siCo. vs siEMD). g) Quantitative real-time PCR (qRT-PCR) assessing the expression levels of the YAP/TAZ endogenous target CTGF (left) and Cyr61 (right) in HEK293 cells treated with the indicated siRNAs and seeded in mechano-OFF conditions. Data are mean + s.d. of n = 3 biologically independent samples. Left graph: P = 0.0055 (siCo. vs siADF/CFL); P = 0.0634 ( $siCo. vs siADF/CFL + si\alpha TAT1$ ); P = 0.6626 ( $siCo. vs siADF/CFL + si\alpha TAT1$ ); P = 0.6626CFL+siNesp4). Right raph: P = 0.0329 (siCo. vs siADF/CFL); P = 0.2094 (siCo. vs  $siADF/CFL + si\alpha TAT1$ ); P = 0.2102 (siCo. vs siADF/CFL + siNesp4). P values were determined by one-way ANOVA with Welch's correction (a-d, g), or with two-way ANOVA (e, f).



Extended Data Fig. 5 | See next page for caption.

Extended Data Fig. 5 | AMOT acts as cytoplasmic mechanical rheostat to control YAP/TAZ activity. a) Quantifications (n = 30 cells for each condition, pooled from two independent seedings) of proteasome (20-S staining) in cells seeded as in Fig. 3a. Preferential accumulation of the proteasome in a single perinuclear area is set to 1 in mechano-ON conditions. Conversely, cells seeded in mechano-OFF displayed multiple proteasome signals scattered throughout the cytoplasm. P < 0.0001. b) Quantifications (n = 30 cells for each condition, pooled from two independent seedings) of proteasome (20-S staining) in cells seeded as in Fig. 3b. Preferential accumulation of the proteasome in a single perinuclear area is set to 1 in siCo. conditions. Conversely, cells depleted of SUN2 or Emerin displayed multiple proteasome signals scattered throughout the cytoplasm. P < 0.0001. c) Representative immunoblot of YAP/TAZ cytoplasmic interactors in HEK293 cells seeded in mechano-ON (stiff) versus mechano-OFF (0.7 kPa hydrogels) conditions. GAPDH serves as sample processing control. See also Supplementary Table 1 for a summary of these results. d) Representative AMOT immunoblot of HEK293 cells seeded in mechano-ON (sparse) versus mechano-OFF (dense) conditions. GAPDH serves as loading control. e) Quantitative real-time PCR (qRT-PCR) showing that the endogenous expression levels of AMOT-130 and AMOT-L1 (HEK293 cells) and AMOT-L2 (MCF10A cells) are unaffected by Mech.ON (stiff) versus Mech.OFF (0.7 kPa hydrogels) conditions. Data are mean + s.d. of n = 3 biologically independent samples. P = 0.4309 (left), P = 0.3940 (middle), P = 0.6024 (right). f) Representative AMOT immunoblot of HEK293 cells treated with increasing doses of the Rho inhibitor 1 (Exoenzyme C3 Transferase, 5 µg ml<sup>-1</sup> and 10 µg ml<sup>-1</sup>, 4 h). GAPDH serves as loading control. g) Representative AMOT immunoblot of HEK293 cells treated with increasing doses of LatrunculinA (Lat.A, 343 nM and 686 nM, 2 h). GAPDH serves as loading control. h) Representative AMOT immunoblot of HEK293 cells treated with the indicated mechano-inhibitory drugs (Das., Dasatinib 100 nM; Def., Defactinib 5 μM; Fasudil 10 μM; Cyto.D, Cytochalasin D1 μM for 2 h). GAPDH serves as loading control. i) Left: representative immunoblot showing quantitation of filamentous (F) versus free globular (G) actin in MCF10A cells seeded on stiff (40 kPa) versus soft (0.7 kPa) hydrogels. Right: quantitation of F/G-actin ratios of the samples shown on the left (see Methods). Results are representative of two independent experiments. j) Representative AMOT immunoblot of HEK293 cells treated with the indicated inhibitors of microtubule polymerization (Nocodazole 5 μM; Vincristine 5 μM, for 1 h). GAPDH serves as loading control. k) Luciferase assay of

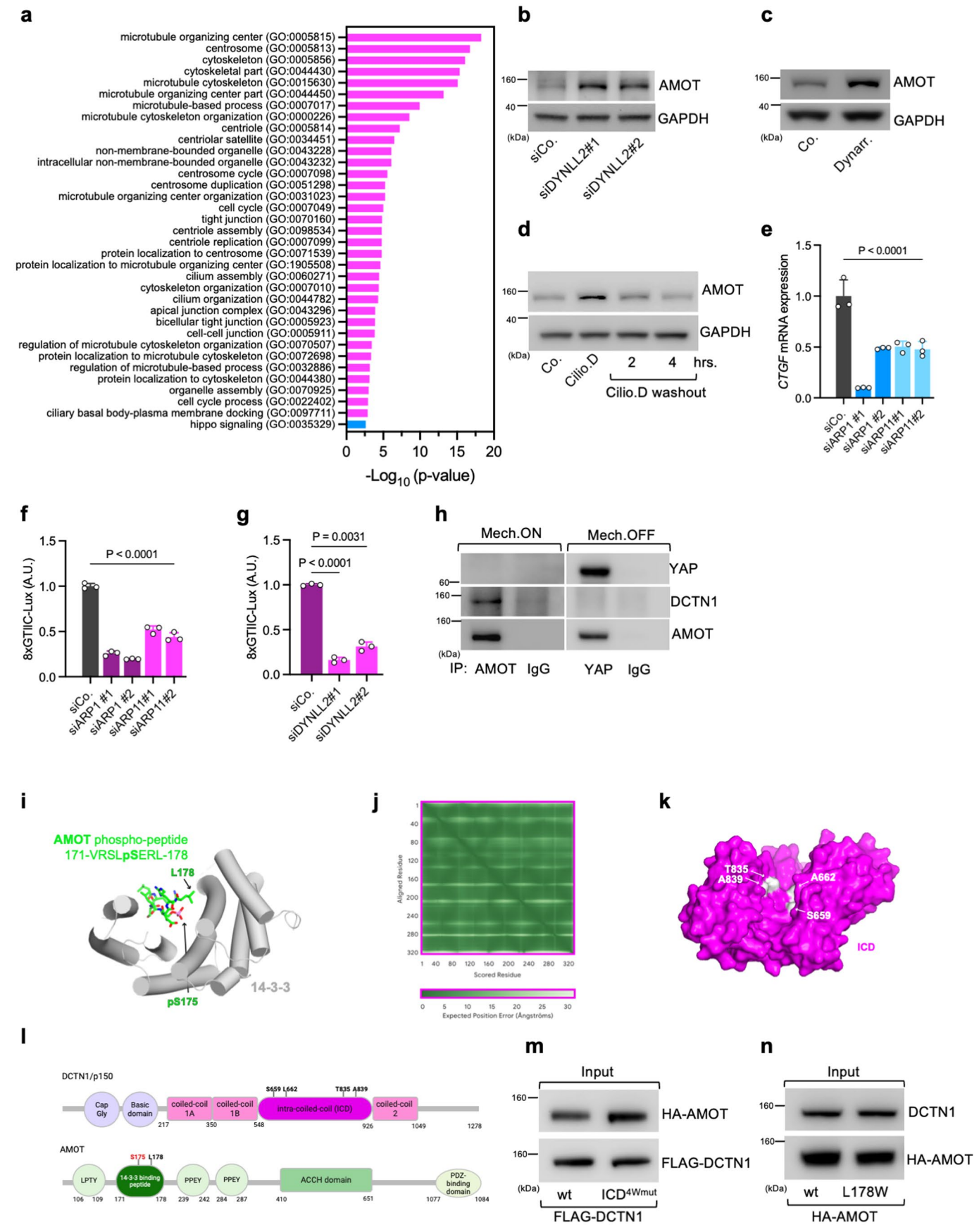
HEK293 cells seeded in mechano-ON conditions and transfected with a synthetic reporter for YAP/TAZ/TEAD-dependent transcription (8xGTIIC-Lux) and with the indicated AMOT mutants. Data are mean + s.d. of n = 3 biologically independent samples. P = 0.0210 (Empty vs AMOTwt), P = 0.0733 (Empty vs AMOT L/PPXA), P = 0.0137 (AMOTwt vs AMOT L/PPXA). I) Luciferase assay of HEK293 cells treated with siRNAs targeting YAP/TAZ and reconstituted with either YAPwt of YAP-WW mutant constructs (see Methods). Cells were concomitantly transiently transfected with AMOT-expressing or empty vectors, and with a synthetic reporter for YAP/TAZ/TEAD-dependent transcription (8xGTIIC-Lux), and after 24 h seeded in mechano-ON conditions. Data are mean + s.d. of n = 3 biologically independent samples. P < 0.0001 (YAPwt AMOT-vs AMOT+), P = 0.8023 (YAPwt AMOT-vs YAPWWmut AMOT+), P = 0.0139 (YAPwt AMOT+vs YAPWWmut AMOT+). m) Quantitative real-time PCR (qRT-PCR) assessing the expression levels of the YAP/TAZ endogenous targets CTGF (left) and Cyr61 (right) in control (wt) or AMOT tKO M2 (see Methods) cells seeded in Mech.ON (stiff) versus Mech. OFF (0.7 kPa hydrogels) conditions. Data are mean + s.d. of n = 3 biologically independent samples. Left graph: P < 0.0001 (wt Mech.ON vs Mech.OFF), P = 0.3100 (wt Mech.ON vs AMOTtKO#1 Mech.OFF), P = 0.9137 (wt Mech.ON vs AMOTtKO#2 Mech.OFF); right graph: P < 0.0008 (wt Mech.ON vs Mech.OFF), P = 0.0977 (wt Mech.ON vs AMOTtKO#1 Mech.OFF), P > 0.9999 (wt Mech.ON vs AMOTtKO#2 Mech.OFF). n) Left: representative immunofluorescence images of YAP/TAZ in hMSCs treated with the indicated siRNAs and seeded in Mech.OFF (1000 µm<sup>2</sup> micropatterns) versus Mech.ON (unconfined) conditions. Nuclei were counterstained with Hoechst (cyan). Scale bar, 20 µm. Cell borders are outlined by orange dashes. Right: quantifications (n = 54 cells for Mech.ON siCo., n = 51 cells for Mech.OFF siAMOT#2, n = 50 cells each for all other conditions, pooled from two independent seedings) of YAP/TAZ nuclear-to-cytoplasmic subcellular localization (N/C) in cells seeded as in left panels. P < 0.0001. **o**) Luciferase assay of HEK293 cells treated with the indicated siRNAs, seeded in mechano-ON versus mechano-OFF (Cyto.D treated) conditions and transfected with a synthetic reporter for YAP/TAZ/TEAD-dependent transcription (8xGTIIC-Lux). Data are mean + s.d. of n = 3 biologically independent samples. P = 0.0027 (siCo. Mech. ON vs Mech.OFF), P = 0.5249 (siCo. Mech.ON vs siAMOT#1 Mech.OFF), P = 0.9874(siCo. Mech.ON vs siAMOT#2 Mech.OFF). Pvalues were determined by unpaired two-tailed Student's t-test with Welch's correction (e), one-way ANOVA with Welch's correction (a, b, k, l, n), or with two-way ANOVA (m, o).



# Extended Data Fig. $6 \mid$ AMOT is constitutively tagged for proteasomal degradation under both mechano-ON and mechano-OFF conditions.

a) Representative AMOT immunoblot of HEK293 cells treated with siRNAs targeting the poly-ADP-ribosyltransferase TNKS1/2 or the E3 ubiquitin ligase RNF146 and seeded in mechano-ON conditions. GAPDH serves as loading control. The same experiment was repeated twice with comparable results.
 b) Representative AMOT immunoblot of HEK293 cells treated with the indicated independent Tankyrase1/2 inhibitors (10 μM, 24 h). GAPDH serves as loading control. The same experiment was repeated twice with comparable results.
 c) Representative RNF146 immunoblot of HEK293 cells seeded in Mech.
 ON (sparse) versus Mech.OFF (dense) conditions. GAPDH serves as loading control. The same experiment was repeated twice with comparable results.
 d) Representative immunofluorescence images of RNF146 in HEK293 cells seeded in Mech.ON (spread) versus Mech.OFF conditions (dense). Nuclei were counterstained with Hoechst (cyan). Scale bar, 25 μm. The same experiment

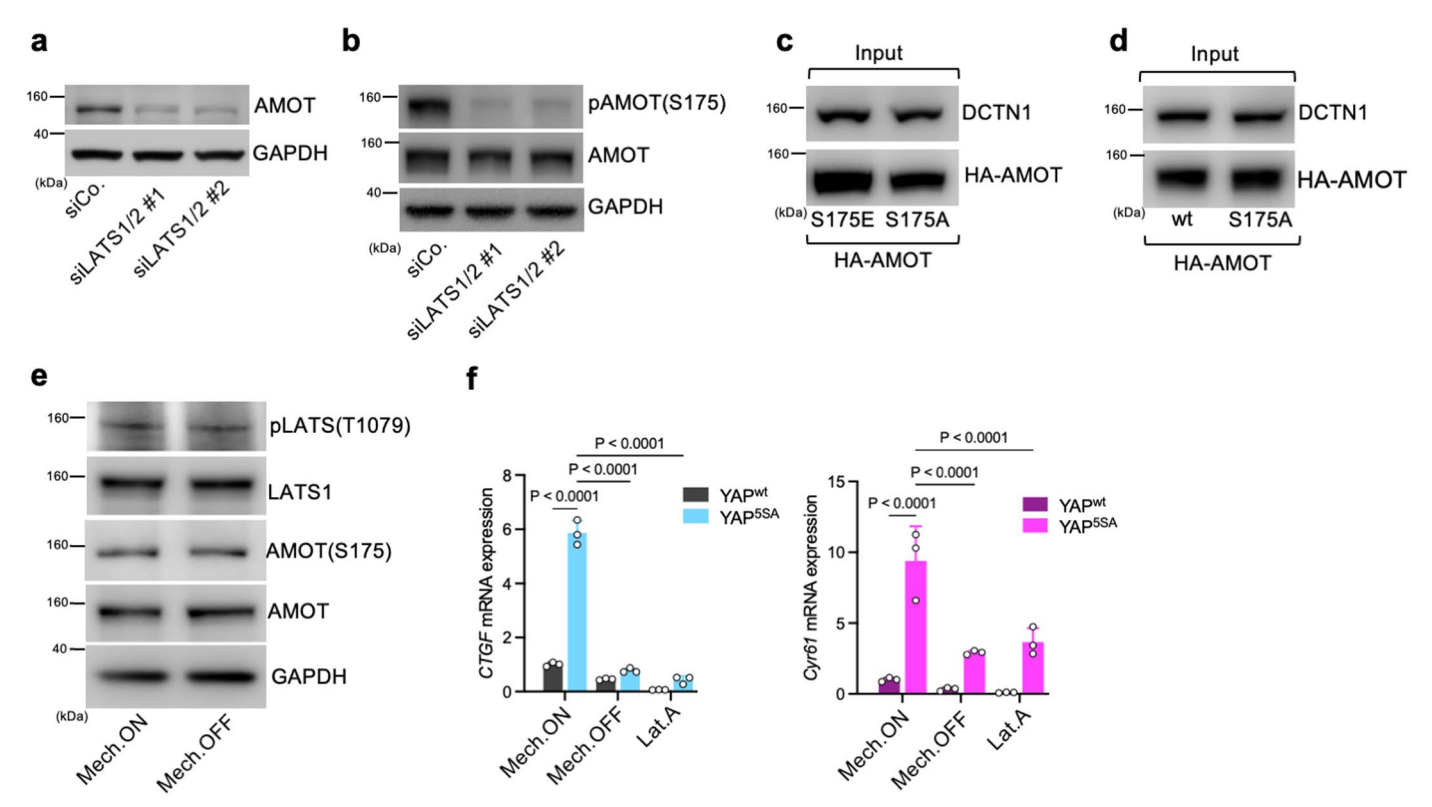
was repeated twice with comparable results.  $\bf e$ ) Representative PARylation assay (see Methods) in HEK293 cells seeded in Mech.ON (sparse) versus Mech.OFF (dense) conditions and treated with proteasome inhibitors showing that AMOT PARylation levels are unaffected by the mechanical state of the cell. GAPDH serves as loading control for inputs. The same experiment was repeated twice with comparable results.  $\bf f$ ) Representative Ubiquitination assays (see Methods) in HEK293 cells seeded in Mech.ON (sparse) versus Mech.OFF (dense) conditions and treated the indicated siRNAs, showing that Tankyrase1/2-dependent AMOT poly-ubiquitination occurs irrespective of the the mechanical state of the cell. The same experiment was repeated twice with comparable results.  $\bf g$ ) Inputs for the co-immunoprecipitation experiment shown in Fig. 4c.  $\bf h$ ) Cycloheximide (CHX) pulse-and-chase experiment (see Methods) in HEK293 cells showing that in mechano-ON conditions, AMOT is rapidly degraded after proteasome inhibitor (Prot.i) washout. Cells were treated with CHX 50  $\mu$ g/mL. GAPDH serves as loading control. The same experiment was repeated twice with comparable results.



Extended Data Fig. 7 | See next page for caption.

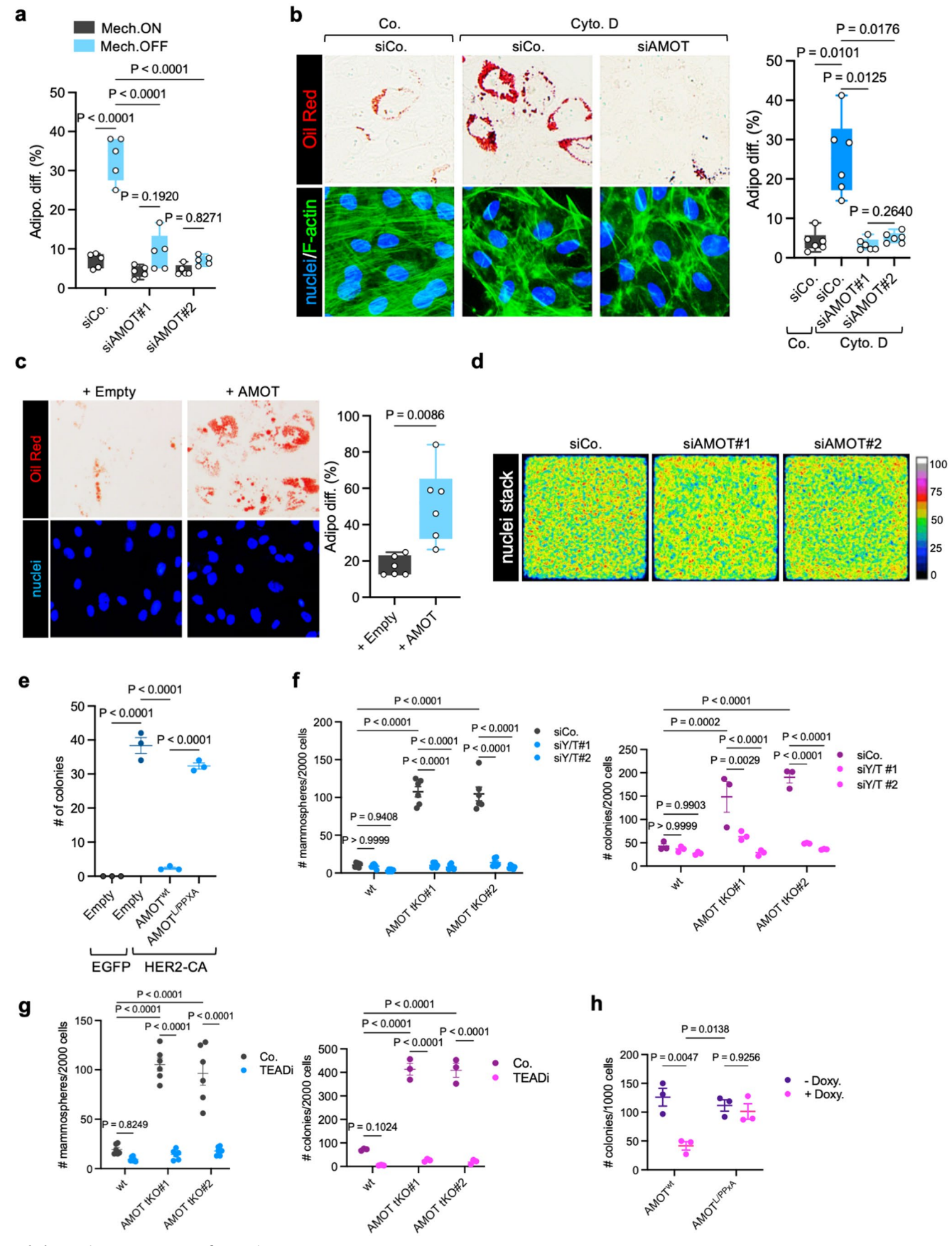
Extended Data Fig. 7 | AMOT delivery to proteasomal condensates by dyneinmediated retrograde transport. a) Graph depicting the most significant GO terms emerging from the Gene Ontology analyses of AMOT proximal proteins, as reported in a publicly available dataset<sup>38</sup>. A full list of retrieved AMOT proximal proteins and associated significant GO terms  $(-Log_{10}[p-value]) \ge 2.6)$ , and associated p-values are provided in Supplementary Table 2. b) Representative AMOT immunoblot of HEK293 cells seeded in mechano-ON conditions and treated with the indicated siRNAs. GAPDH serves as loading control. c) Representative AMOT immunoblot of HEK293 cells seeded in mechano-ON conditions and treated with DMSO (Co.) or Dynarrestin (10 µM, 6 h). GAPDH serves as sample processing control. d) Representative AMOT immunoblot of HEK293 cells seeded in mechano-ON conditions and treated with DMSO (Co.) or Ciliobrevin D (Cilio.D 10 μM, 5 h). Cilio.D treatment was followed by 2 or 4 h of washout. GAPDH serves as loading control. e) Quantitative real-time PCR (qRT-PCR) assessing the expression levels of the YAP/TAZ endogenous target CTGF in HEK293 cells treated with the indicated siRNAs and seeded in mechano-ON conditions. Data are mean + s.d. of n = 3 biologically independent samples. P < 0.0001. **f.g**) Luciferase assay of HEK293 cells treated with the indicated siRNAs, seeded in mechano-ON conditions and transfected with a synthetic reporter for YAP/TAZ/TEAD-dependent transcription (8xGTIIC-Lux).

Data are mean + s.d. of n = 3 biologically independent samples. P = 0.0031 for siCo. vs siDYNLL2#2), P < 0.0001 for all other comparisons shown. **h**) Pulldown of endogenous AMOT (left) or endogenous YAP (right) from proteasome-inhibited HEK293T cell seeded in Mech.ON versus Mech.OFF conditions, showing that AMOT bound to DCTN1 in Mech.ON cells is unable to bind to YAP. IgG pulldown serves as negative control. i) Cartoon representations of the X-ray structure (PDB code 7nma)<sup>43</sup> of the 14-3-3 domain (grey) in complex with a short AMOT peptide phosphorylated at S175 (pS175). The AMOT peptide is shown as stick representation in green with pS175 and L178 highlighted. j) AlphaFold2 predicted alignment error (PAE) plot<sup>81</sup> for the complex shown in Fig. 4g, indicating that the ICD structure is predicted with very high confidence. k) DCTN1-ICD as surface representation with highlighted in white the four residues (\$659, A662, T835, A839) lining the putative binding cleft. These have been replaced by tryptophans for co-immunoprecipitation (co-IP) assays of Fig. 4h (see main text for details). I) Schematic illustrations of the domain structures and motifs of DCTN1/ p150 (top) and AMOTp130 (bottom). Created in BioRender. m) Representative immunoblots of the inputs of the pulldown experiment shown in Fig. 4h. n) Representative immunoblots of the inputs of the pulldown experiment shown in Fig. 4i. P values were determined by one-way ANOVA with Welch's correction (e-g), or with multiple testing correction using the default g:SCS method (a).



Extended Data Fig. 8 | Hippo/LATS signaling indirectly feeds on YAP/TAZ mechanoregulation through AMOT. a) Representative AMOT immunoblot of HEK293 cells treated with the indicated siRNAs and seeded in mechano-OFF conditions. GAPDH serves as loading control. The same experiment was repeated twice with comparable results. b) Representative phospho-AMOT-S175 immunoblot of HEK293 cells transfected with the indicated siRNAs, seeded in mechano-ON conditions and treated with proteasome inhibitor (Lactacystin,  $10\,\mu\text{M}$ ,  $8\,\text{h}$ ). GAPDH serves as loading control. The same experiment was repeated twice with comparable results. c) Representative immunoblots of the inputs of the pulldown experiment shown in Fig. 5b. d) Representative immunoblots of the inputs of the pulldown experiment

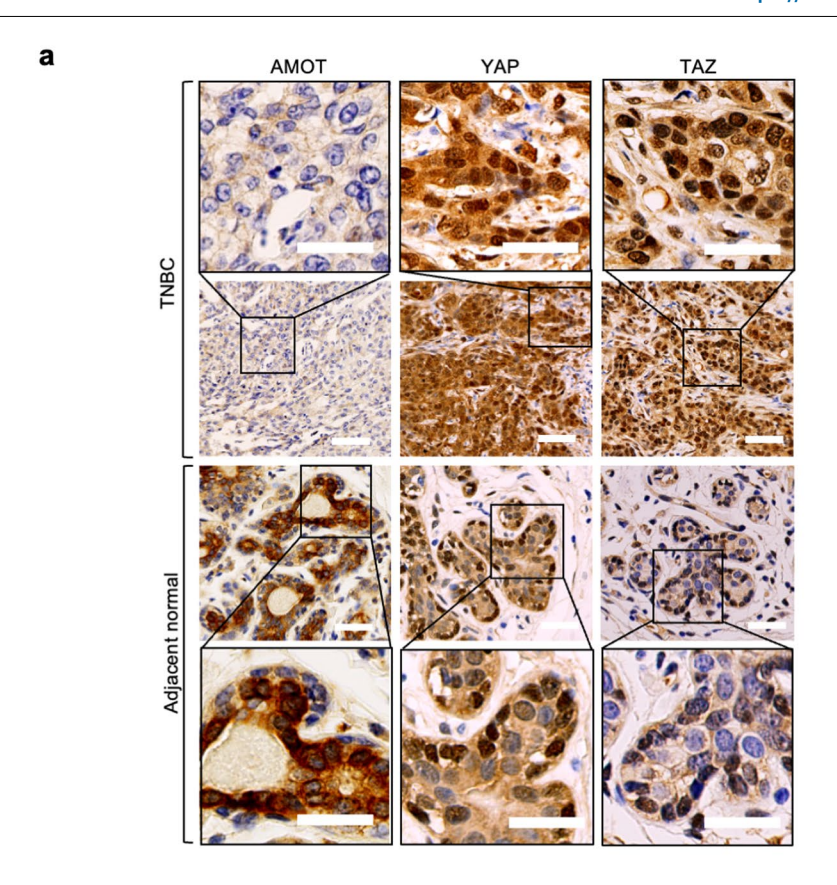
shown in Fig. 5c. e) Representative immunoblots of HEK293 cells seeded in Mech.ON (stiff) versus Mech.OFF (0.7 kPa hydrogels) conditions treated with proteasome inhibitor (Lactacystin,  $10~\mu M$ , 8~h), showing that AMOT-S175 and LATS1-T1079 phosphorylation is unaffected by cell mechanics. GAPDH serves as loading control. The same experiment was repeated twice with comparable results. f) Quantitative real-time PCR (qRT-PCR) assessing the expression levels of the YAP/TAZ endogenous targets CTGF (left) and Cyr61 (right) in YAPwt or YAP5SA reconstituted MCF10A cells (see Methods) seeded in Mech.ON (sparse), Mech.OFF (dense) conditions or treated with Lat. A (343 nM, 15 h). Data are mean + s.d. of n = 3 biologically independent samples. P < 0.0001. P values were determined by two-way ANOVA (f).

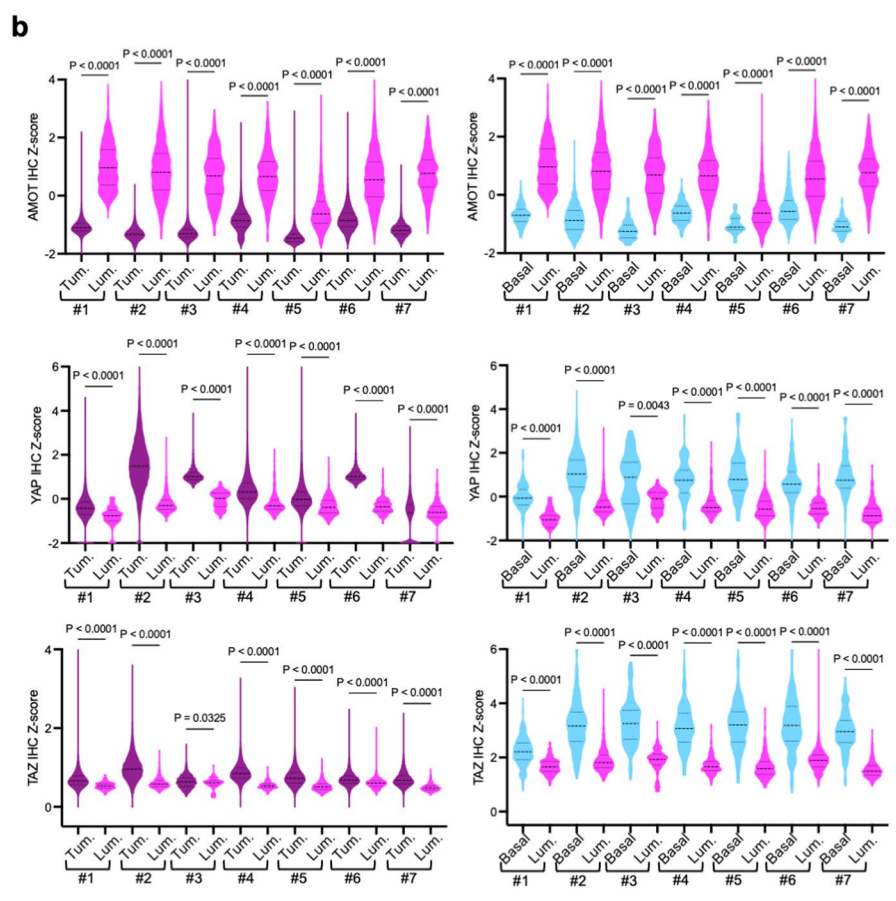


 $\textbf{Extended Data Fig. 9} \, | \, \textbf{See next page for caption.} \\$ 

Extended Data Fig. 9 | AMOT acts as mechanical rheostat to control biological responses driven by YAP/TAZ. a) Quantifications of the percentage of adipogenic differentiation (based on Oil Red staining) of hMSCs seeded on spread (unconfined, Mech.ON) or small (1000 µm<sup>2</sup>, Mech.OFF) micropatterns and treated with the indicated siRNAs, as in Fig. 6a. Data are representative of n = 5 biologically independent experiments, with 100 cells quantified each. Boxplot shows interquartile range and whiskers represent min to max. P = 0.1920(siAMOT#1 Mech.ON vs Mech.OFF), P = 0.8271 (siAMOT#2 Mech.ON vs Mech. OFF), P < 0.0001 for all other comparisons shown. b) Left: Representative Oil Red staining of hMSCs transfected with the indicated siRNAs, seeded in mechano-ON conditions and treated with DMSO (Co.) or with Cytochalasin D (Cyto.D, see Methods). To verify Cyto.D effectiveness, F-actin was labelled with phalloidin (F-actin, green). Nuclei were counterstained with Hoechst (blue). Right: quantifications of the percentage of adipogenic differentiation (based on Oil Red staining) of hMSCs treated as in left panels. Data are representative of n = 6biologically independent experiments, with 100 cells quantified each. Boxplot shows interquartile range and whiskers represent min to max. P = 0.0101 (Co. vs CvtoD), P = 0.0125 (siCo, vs siAMOT#1 CvtoD), P = 0.0176 (siCo, vs siAMOT#2 CytoD). c) Left: Representative Oil Red staining of hMSCs seeded in mechano-ON conditions, transduced with Empty or AMOT-encoding lentiviral vectors and subjected to adipogenic differentiation protocol (see Methods). Nuclei were counterstained with Hoechst (blue). Right: quantifications of the percentage of adipogenic differentiation (based on Oil Red staining) of hMSCs treated as in left panels. Data are representative of n = 6 biologically independent experiments, with 100 cells quantified each. Boxplot shows interquartile range and whiskers represent min to max. P = 0.0086. d) Representative colorimetric stacked images of Hoechst counterstained nuclei of MCF10A cells treated with the indicated siRNAs and seeded as cell monolayers of defined dimensions as in Fig. 6b. The colour scale indicates the density of Hoechst labelled nuclei, showing a uniform distribution of cells within the monolayers in all the experimental conditions. e) Quantifications of the number of colonies formed by human mammary

luminal differentiated cells undergoing oncogenic reprograming when transduced with lentiviral vectors encoding for the indicated factors, as in Fig. 6d (n = 3 biologically independent experiments): HER-CA, constitutive active HER2 mutant (see Methods); AMOT L/PPXA, AMOT point mutant in the three L/PPXY YAP-binding motifs (see Methods). Lines represent mean  $\pm$  s.e.m. P < 0.0001. **f**) Left: Quantifications of the number of mammospheres (n = 6 biological independent samples) formed by control (wt) or AMOT tKO MII cells treated with the indicated siRNAs. Right: Quantifications of the number of soft agar colonies (n = 3 biological independent samples) formed by control (wt) or AMOT tKO MII cells treated with the indicated siRNAs. Lines represent mean  $\pm$  s.e.m. Left graph: P > 0.9999 (wt siCo. siY/T#1), P = 0.9408 (wt siCo. siY/T#2), P < 0.0001for all other comparisons shown. Right graph: P > 0.9999 (wt siCo. vs siY/T#1), P = 0.9903 (wt siCo, vs siY/T#2), P = 0.0002 (wt siCo, vs AMOTtKO#1 siCo.). P = 0.0029 (AMOTtKO#1 siCo. vs AMOTtKO#1 siY/T#1), P < 0.0001 for all other comparisons shown. g) Left: Quantifications of the number of mammospheres (n = 6 biological independent samples) formed by control (wt) or AMOT tKO MII cells treated with the TEAD inhibitor VT107 (see Methods), or with DMSO (Co.). Right: Quantifications of the number of soft agar colonies (n = 3 biological independent samples) formed by control (wt) or AMOT tKO MII cells treated with the with the TEAD inhibitor VT107 (see Methods), or with DMSO (Co.). Lines represent mean  $\pm$  s.e.m. Left graph: P = 0.8249 (wt Co. vs TEADi), P < 0.0001 for all other comparisons shown. Right graph: P = 0.1024 (wt Co. vs TEADi), P < 0.0001for all other comparisons shown. h) Quantifications of the number of soft agar colonies (n = 3 biological independent samples) formed by MDA-MB-231 cells transduced with lentiviral vectors encoding for the indicated doxycycline (Doxy)-inducible AMOT mutant constructs. Lines represent mean ± s.e.m. P = 0.0047 (AMOTwt -Doxy vs AMOTwt +Doxy), P = 0.0138 (AMOTwt +Doxy vs AMOTL/PPXA -Doxy), P = 0.9256 (AMOTL/PPXA -Doxy vs AMOTL/PPXA +Doxy). P values were determined by two-way ANOVA (a, f-h), or by one-way ANOVA with Welch's correction  $(\mathbf{b}, \mathbf{e})$ , or by unpaired two-tailed Student's t-test with Welch's correction (c).





 $\textbf{Extended Data Fig. 10} \, | \, \textbf{See next page for caption.}$ 

#### Extended Data Fig. 10 | Role of AMOT as candidate tumour suppressor.

a) Representative large field immunohistochemical pictures of AMOT, YAP and TAZ proteins in chemo-naïve human triple negative breast cancer (TNBC) samples or adjacent normal mammary tissue. The enlargements (top and bottom panels) are the same pictures shown in Fig. 6g. Data are representative of n=7 independent patient samples. Scale bars, 50  $\mu$ m. b) Digital-pathology based quantifications (Z-scores, see Methods) of AMOT abundance and YAP/TAZ nuclear-to-cytoplasmic subcellular localization based on immunohistochemical signals in the indicated cell populations (Tumour, Tum.; adjacent normal luminal,

Lum.; and adjacent normal basal mammary cells, Basal) in independent TNBC samples (#1-#7), as shown in representative pictures of Fig. 6g and Extended Data Fig. 10a. n = 702261 tumour and n = 138509 normal cells were quantified for AMOT, n = 197876 tumour and n = 3264 normal cells were quantified for YAP, n = 144099 tumour and n = 5205 normal cells were quantified for TAZ. P = 0.0325 (TAZ IHC Tum. vs Lum. #3), P = 0.0043 (YAP IHC Basal vs Lum. #3), P < 0.0001 for all other comparisons shown. P values were determined by unpaired Student's t-test with Welch's correction (t).

# nature portfolio

| Corresponding author(s):   | Stefano Piccolo |
|----------------------------|-----------------|
| Last updated by author(s): | Aug 14, 2025    |

# **Reporting Summary**

Nature Portfolio wishes to improve the reproducibility of the work that we publish. This form provides structure for consistency and transparency in reporting. For further information on Nature Portfolio policies, see our <u>Editorial Policies</u> and the <u>Editorial Policy Checklist</u>.

| <. | トつ | 1  | ıc:  | ŀι | CS |
|----|----|----|------|----|----|
| J  | ιa | ı. | I.O. | LΙ | LJ |

| For         | all statistical analyses, confirm that the following items are present in the figure legend, table legend, main text, or Methods section.  |
|-------------|--|
| n/a         | Confirmed  |
|             | The exact sample size ( $n$ ) for each experimental group/condition, given as a discrete number and unit of measurement  |
|             | A statement on whether measurements were taken from distinct samples or whether the same sample was measured repeatedly  |
|             | The statistical test(s) used AND whether they are one- or two-sided Only common tests should be described solely by name; describe more complex techniques in the Methods section.   |
| X           | A description of all covariates tested   |
|             | A description of any assumptions or corrections, such as tests of normality and adjustment for multiple comparisons  |
|             | A full description of the statistical parameters including central tendency (e.g. means) or other basic estimates (e.g. regression coefficient) AND variation (e.g. standard deviation) or associated estimates of uncertainty (e.g. confidence intervals) |
|             | For null hypothesis testing, the test statistic (e.g. <i>F</i> , <i>t</i> , <i>r</i> ) with confidence intervals, effect sizes, degrees of freedom and <i>P</i> value noted <i>Give P values as exact values whenever suitable.</i>                        |
| $\boxtimes$ | For Bayesian analysis, information on the choice of priors and Markov chain Monte Carlo settings   |
| X           | For hierarchical and complex designs, identification of the appropriate level for tests and full reporting of outcomes   |
| $\boxtimes$ | Estimates of effect sizes (e.g. Cohen's $d$ , Pearson's $r$ ), indicating how they were calculated   |
|             | Our web collection on <u>statistics for biologists</u> contains articles on many of the points above.  |

#### Software and code

Policy information about availability of computer code

Data collection

LASX software (v.4.1.0.23081) was used to acquire immunofluorescence images with Leica Stellaris Confocal microscope. NDPscan3.1 software was used to acquire immunohistochemical images with a Nanozoomer Scanner 2.0RS (Hamamatsu). QuantStudio Design and Analysis software (version 1.4.3) was used to collect qRT-PCR data. INfinite P200PRO plate reader i-control software version 1.12 (Tecan) was used to collect Luciferase reporter assay data.

Data analysis

Fiji-ImageJ2 (v2.14.0/1.54j) was used to analyse and quantify immunofluorescence data. Leica AIVIA (version 14.0.0) software was used for 3D reconstruction of fluorescence images. QuPath 5.0 was used for quantification of immunohistochemical stainings. Graphpad Prism (version 10.4.1) was used for statistical analysis. AlphaFold2 was used for protein structure predictions.

For manuscripts utilizing custom algorithms or software that are central to the research but not yet described in published literature, software must be made available to editors and reviewers. We strongly encourage code deposition in a community repository (e.g. GitHub). See the Nature Portfolio guidelines for submitting code & software for further information.

#### Data

Policy information about availability of data

All manuscripts must include a data availability statement. This statement should provide the following information, where applicable:

- Accession codes, unique identifiers, or web links for publicly available datasets
- A description of any restrictions on data availability
- For clinical datasets or third party data, please ensure that the statement adheres to our policy

Source data are provided with this study. All other data supporting the findings of this study are available from the corresponding author on reasonable request. Previously published crystal structure of 14-3-3 in complex with Amot-p130 peptide (Centorrino et al. Curr Res Struct Biol 2022) is available from RCSB Protein Data Bank PDB code 7nma. The BioGRID31 human database is available at https://downloads.thebiogrid.org/BioGRID/Release-Archive/BIOGRID-3.5.169/. Previously published (Go et al., Nature 2021) mass spectrometry datasets of human proximal proteins, are available at ProteomeXchange through partner Mass spectrometry Interactive Virtual Environment MassIVE (http://proteomics.ucsd.edu/ProteoSAFe/datasets.jsp) PXD015530, PXD015531. Correspondence and requests for materials should be addressed to Stefano Piccolo (stefano.piccolo@unipd.it).

#### Research involving human participants, their data, or biological material

Policy information about studies with <u>human participants or human data</u>. See also policy information about <u>sex, gender (identity/presentation)</u>, <u>and sexual orientation</u> and <u>race, ethnicity and racism</u>.

Reporting on sex and gender

For fresh discard tissue for reductive mastoplasty collection only female patients of age >18. All included subjects were negative for HIV, HBV, HCV or any other disease related to the study.

Reporting on race, ethnicity, or other socially relevant groupings

No socially constructed or socially relevant variables were considered.

Population characteristics

All included subjects for fresh sample collection were negative for HIV, HBV, HCV or any other disease related to the study.

Recruitment

Patients undergoing reductive mastoplasty were rectruited after signature of informed consent to the donation of bioptic material for the research. Recruited participants were informed on the research's scopes and procedures clarifying how participation to the study does not imply nor contemplate any alteration in clinical or surgical protocols. No bias was included in participant rectruitment.

Archival TNBC samples were collected in the context of the METAMECH consortium.

Ethics oversight

Discard tissue was collected from anonymized healthy women undergoing reductive mastoplasty surgery with informed consent according to our institutional guidelines and by the Azienda Ospedaliera di Padova Ethics Commitee (CESC; CanerOrg protocol 3989/AO/16). Archival TNBC samples were collected in the context of the METAMECH consortium (IFOM-CPO007/2019/PO006).

Note that full information on the approval of the study protocol must also be provided in the manuscript.

# Field-specific reporting

| Ple | ease select the one below | that is the best fit for your research. | If yo | ou are not sure, read the appropriate sections before making your selection. |
|-----|---------------------------|---|-------|--|
| X   | Life sciences             | Behavioural & social sciences           |       | Ecological, evolutionary & environmental sciences                            |

For a reference copy of the document with all sections, see <u>nature.com/documents/nr-reporting-summary-flat.pdf</u>

## Life sciences study design

All studies must disclose on these points even when the disclosure is negative.

Sample size

The number of biological and technical replicates and the number of animals is indicated in the Fig. Legends, Main text and Methods section. The sample size was not predetermined

Data exclusions No data was excluded from the analysis. All tested animals were included. The animal ages and sexes are specified in the text and Methods

Replication All biological replicates are as detailed in Figures and legends.

Randomization Allocation of animals to injection with different cell lines was random. Randomization was not relevant to our experiments with cell lines.

Blinding Was not relevant for the study. Results were collected in an equipment or software-based manner, as detailed in the Methods

Blinding was not relevant for the study. Results were collected in an equipment or software-based manner, as detailed in the Methoc section, and did not involve subjective rating.

# Reporting for specific materials, systems and methods

We require information from authors about some types of materials, experimental systems and methods used in many studies. Here, indicate whether each material, system or method listed is relevant to your study. If you are not sure if a list item applies to your research, read the appropriate section before selecting a response.

| Materials & experimental systems   |             | ethods                 |  |  |
|--|-------------|------------------------|--|--|
| n/a Involved in the study  | n/a         | Involved in the study  |  |  |
| Antibodies   | $\boxtimes$ | ChIP-seq               |  |  |
| Eukaryotic cell lines  |             |                        |  |  |
| Palaeontology and archaeology  | ogy         | MRI-based neuroimaging |  |  |
| Animals and other organism   | S           |                        |  |  |
| Clinical data  |             |                        |  |  |
| Dual use research of concern   |             |                        |  |  |
| □ Plants   |             |                        |  |  |
| '  |             |                        |  |  |
| Antibodies   |             |                        |  |  |
| Antibodies used  Primary antibodies used for immunofluorescence were: YAP (Santa Cruz Biotechnology, sc-101199, 1:200), LaminA/C (Santa Cruz Biotechnology, sc-376248, 1:200), Paxillin (Abcam no. ab32084, 1:50), GFP (Abcam ab13970, 1:200), Proteasome subunit alpha 5 (PSMA5) (Origene, TA332887, 1:200), AMOT (Santa Cruz Biotechnology, sc-166924, 1:200), AMOTL1 (Sigma HPA001196, 1:200), alpha Tubulin (Abcam, ab18251, 1:500), gamma-Tubulin (Santa Cruz Biotechnology, sc-17787, 1:500), acetylated-Tubulin (ab24610 1:200), Pericentrin 1 (Santa Cruz Biotechnology, sc-376111, 1:200), LaminC/C (Abcam, ab89814, 1:200), RNF146 (Thermofisher, H00081847-B01P, 1:200). Secondary antibodies used for immunofluorescence were Alexa-Fluor conjugated secondary antibodies from Invitrogen (1:200). Antibodies used for immunohistochemistry were anti-YAP (CST #4912, 1:7000), anti-TAZ (Sigma-Aldrich HPA007415, 1:50) and anti-AMOTL1 (Sigma-Aldrich HPA001196, 1:1000). |             |                        |  |  |

Antibodies used for PLA assays were YAP1 (Proteintech, 13584-AP, 1:200) and AMOT (Santa Cruz Biotechnology, sc-166924, 1:200). Antibodies used for co-immunoprecipitation (all 2  $\mu$ g/sample) and immunoblot experiments were: anti YAP/TAZ (Santa Cruz Biotechnology, sc-101199, 1:1000), anti AMOTL1 (Sigma-Aldrich, HPA001196, 1:1000), anti LATS1 (CST, 3477, 1:1000), anti LATS2 (CST, 5888, 1:1000), anti phospho-Angiomotin Ser 175 (Millipore, ABS1045, 1:1000), anti phospho-LATS1 Thr1079 (CST, 8654, 1:1000), anti DCTN1/p150Glued (Abcam, ab96004, 1:2000), anti 20S/PSMA5 (Abcam, 189855, 1:1000), anti GAPDH (Millipore, MAB374, 1:100000), anti HA-tag (Santa Cruz Biotechnology, sc-7392, 1:1000), anti FLAG-HRP (Sigma-Aldrich, A8592, 1:5000), anti Poly-ADP-Ribose (Biotechne, 4335, 1:1000), anti RNF146 (Thermofisher, H00081847-B01P, 1:1000), anti AMOT (Proteintech, 24-550-1-AP, 1:1000), anti  $\beta$ -TrCP/HOS (Santa Cruz Biotechnology, sc-166492, 1:1000), anti PP1 (Santa Cruz Biotechnology, sc-7482, 1:1000), anti S3BP2 (Santa Cruz Biotechnology, sc-385381, 1:1000), anti NHERF-2 (Santa Cruz Biotechnology, sc-365888), 1:1000, anti USP10 (Santa Cruz Biotechnology, sc-365828, 1:1000), anti OTUB2 (Proteintech, 12066-1-AP, 1:1000), anti PRRG4 (Invitrogen, PA5-115801, 1:1000), anti Pan 14-3-3 (Santa Cruz Biotechnology, sc-1657, 1:1000), anti-FLAG M2 (Sigma-Aldrich F1804, 1:1000), anti-HA (Abcam ab9110, 1:1000), anti-Tubulin (Abcam, ab18251, 1:1000), anti-acetylated-tubulin K40 (Abcam, ab24610, 1:1000). Antibodies used for FACS were: CD31 (BioLegend no. 303119), CD45 (BD Biosciences no. 557833), CD49f (BD Biosciences no. 555736) and EpCAM (BD Biosciences no. 347197).

Validation

Anti YAP (Santa Cruz Biotechnology, sc-101199) was previously validated as YAP/TAZ antibody (Dupont et al., Nature 2011; Aragona et al. Cell 2013; Panciera et al., Nat Mater 2020; Zanconato et al., nat Med 2018). We validated Anti AMOTL1 (Sigma-Aldrich HPA001196) as AMOT130/AMOTL1/AMOTL2 antibody through the use triple KD and triple KO cell lines. All other antibodies were previously validated by the manufacturer.

#### Eukaryotic cell lines

Policy information about <u>cell lines and Sex and Gender in Research</u>

Cell line source(s)

MCF10A cells were a kind gift from F. Miller (Karmanos), MCF10A-YAP-eGFP-KI cells were a kind gift from J.T.Liphardt, MII cells were a kind gift from S. Santner, U2OS (ATCC HTB-96), HEK293 (ATCC CRL-1573) and HEK293T (ATCC CRL-3216) cells were from ATCC, MDA-MB-231 cells (ICLC HTL99004) were from the ICLC, Bone marrow-derived hMSCs were purchased from Lonza (C-12974), HEK293 LATS dKO cells were a kind gift from KL Guan.

Authentication

All parental cell lines were authenticated by BMR Genomics Cell Profiler service based on exon PCR sequencing.

Mycoplasma contamination All cell lines were routinely tested to exclude mycoplasma contamination.

Commonly misidentified lines (See ICLAC register)

No commonly misidentified cell lines were used.

#### Animals and other research organisms

Policy information about <u>studies involving animals</u>; <u>ARRIVE guidelines</u> recommended for reporting animal research, and <u>Sex and Gender in Research</u>

| Laboratory animals      | 3 weeks of age female NOD-SCID Mus musculus mice (IMSR no. CRL:394, Charles River) were employed. Mice were kept in standard cages with a maximum occupancy of 5 mice per cage, ad libitum feeding and drinking water, 21°C controlled temperature and 12h light cycle. |
|-------------------------|---|
| Wild animals            | The study did not involve wild animals  |
| Reporting on sex        | Only female mice were used for orthotopic mammary fat pad transplantations.   |
| Field-collected samples | The study did not involve field collected samples.  |
| Ethics oversight        | Animal experiments were performed adhering to our institutional guidelines as approved by the University animal welfare body (Organismo Preposto al Benessere Animale: OPBA). Reporting was compliant to the ARRIVE guidelines.   |

Note that full information on the approval of the study protocol must also be provided in the manuscript.

| 1) | - | ٠+ | _ |
|----|---|----|---|
| _  | _ |    | ` |

| Seed stocks           | No plants involved in the study |
|-----------------------|---------------------------------|
| Novel plant genotypes | No plants involved in the study |
|                       |                                 |
| Authentication        | No plants involved in the study |
|                       |                                 |

#### Flow Cytometry

#### Plots

Confirm that:

The axis labels state the marker and fluorochrome used (e.g. CD4-FITC).

The axis scales are clearly visible. Include numbers along axes only for bottom left plot of group (a 'group' is an analysis of identical markers).

All plots are contour plots with outliers or pseudocolor plots.

A numerical value for number of cells or percentage (with statistics) is provided.

#### Methodology

Sample preparation

Single-cell suspensions of primary human mammary cells were generated as previously described (Panciera et al., Nat Mater 2020), with minor modifications. Briefly, the ductal tree was mechanically minced and enzymatically digested in tissue dissociation medium (Advanced DMEM-F12 supplemented with HEPES, 1.5% GlutaMAX, 600 U ml-1 collagenase and 200 U ml-1 hyaluronidase at 37 °C overnight). Cells were spun down 3 min at 700 r.p.m., and the pellet was further dissociated in 0.25% trypsin-EDTA for 5 min followed by the addition of 5 ug ml-1 dispase and 1 µg ml-1 DNasel for a further 10 min. Digestion was stopped in Advanced DMEM 10% FBS, and cells were filtered through a 40 µm strainer to remove residual tissue fragments and cell aggregates. Single-cell suspensions of primary mammary cells were stained with CD31 (BioLegend no. 303119), CD45 (BD Biosciences no. 557833), CD49f (BD Biosciences no. 555736) and EpCAM (BD Biosciences no. 347197) in DMEM for 30 min at 4 °C.

Instrument

A FACS Aria III (BD Biosciences) was employed

Software

FACS Diva software

Cell population abundance

No relative abundance of the post-sort fractions was determined. The purity of the populations was verified by gene-espression analyses, according to the previously published standard (Panciera et al., Nat Mater 2020).

Gating strategy

The gating strategies are detailed in Methods. After excluding CD31+CD45+(Lin+) cells, mammary cells were sorted into four populations, as previously shown (Panciera et al., Nat Mater 2020): Luminal differentiated cells, CD49f–EpCAM+; Luminal progenitor cells, CD49f+EpCAM+; basal cells, CD49f+EpCAM-; and stromal cells, CD49f–EpCAM-. Exemplification of the

gating strategy can be found in previous work by the same authors employing this same method on the same type of biological material (see Panciera et al., Nat Mater 2020).